January 2012

Tornadogenesis And Tornadogenesis Failure In Numerically Simulated Supercells

Jason Naylor

Recommended Citation

Naylor, Jason, "Tornadogenesis And Tornadogenesis Failure In Numerically Simulated Supercells" (2012). *Theses and Dissertations*. 1364.
https://commons.und.edu/theses/1364

TORNADOGENESIS AND TORNADOGENESIS FAILURE IN NUMERICALLY SIMULATED SUPERCELLS

by

Jason Naylor
Bachelor of Science, California University of Pennsylvania, 2005
Master of Science, University of North Dakota, 2008

A Dissertation

Submitted to the Graduate Faculty

of the

University of North Dakota

In partial fulfillment of the requirements

for the degree of

Doctor of Philosophy

Grand Forks, North Dakota
December
2012

This dissertation, submitted by Jason Naylor in partial fulfillment of the requirements for the Degree of Doctor of Philosophy from the University of North Dakota, has been read by the Faculty Advisory Committee under whom the work has been done, and is hereby approved.

Matthew Gilmore
Chairperson

Mark Askelson

Gretchen Mullendore

Michael Poellot

Robert Newman

This dissertation is being submitted by the appointed advisory committee as having met all of the requirements of the Graduate School at the University of North Dakota and is hereby approved.

Wayne Swisher
Dean of the Graduate School

December 4, 2012
Date

Title	Tornadogenesis and Tornadogenesis Failure in Numerically Simulated Supercells
Department	Atmospheric Sciences
Degree	Doctor of Philosophy

In presenting this dissertation in partial fulfillment of the requirements for a graduate degree from the University of North Dakota, I agree that the library of this University shall make it freely available for inspection. I further agree that permission for extensive copying for scholarly purposes may be granted by the professor who supervised my dissertation work or, in his absence, by the Chairperson of the department or the dean of the Graduate School. It is understood that any copying or publication or other use of this dissertation or part thereof for financial gain shall not be allowed without my written permission. It is also understood that due recognition shall be given to me and to the University of North Dakota in any scholarly use which may be made of any material in my dissertation.

Jason Naylor
4 December 2012

TABLE OF CONTENTS

CHAPTER

2. METHODOLOGY

3. AUTOMATED SUPERCELL DETECTION

4. CONVECTIVE INITIATION TESTS

Results and Discussion

LIST OF FIGURES

LIST OF TABLES

ACKNOWLEDGEMENTS

This work was supported by NSF grant AGS-0843269. Computational resources were provided by the National Center for Supercomputing Applications through Teragrid allocation TG-MCA94P023; and the Texas Advanced Computing Center and National Institute of Computational Sciences through XSEDE allocation TG-ATM100048. Along with my advisor, Dr. Matthew Gilmore, I would like to thank my committee members Dr. Mark Askelson, Dr. Gretchen Mullendore, Prof. Mike Poellot and Dr. Robert Newman. I would also like to thank Richard Thompson and Roger Edwards for providing the RUC-2 soundings, Jerry Straka for suggesting a nudging technique for capped soundings, and Justin Weber for assisting with the simulations.

ABSTRACT

Simulations were performed in an idealized cloud model to study the processes responsible for tornadogenesis and tornadogenesis failure. The simulations were initialized with supercell proximity soundings taken from the Rapid Update Cycle (RUC) model. Because of the large number of simulations performed, several objective techniques were developed and tested to assist in the simulations—including automated supercell and tornado detection. In addition, the vast majority of the RUC soundings contained capping inversions, and thus the traditional 'warm bubble' convective initiation technique was unsuccessful. A new sustained convective initiation technique was tested to determine which configuration produced the strongest, longest-lived supercells.

Twenty-one tornadic simulations were examined. It was found that 0-3 km storm relative environmental helicity was the best predictor of the intensity (i.e. maximum pressure drop) and duration of the simulated tornadoes. A trajectory analysis found that vertical vorticity was generated in rising parcels as they ascended towards the tornado, and also by parcels that descended from aloft. However, large positive vertical vorticity was only produced after the parcels reached the surface. The most striking difference between the tornadic and nontornadic simulations was that the tornadic simulations produced more negative vertical vorticity in descending parcels, and that the parcels that entered the low-level circulation rose to higher altitudes than the parcels in the nontornadic simulations.

CHAPTER 1

INTRODUCTION AND OVERVIEW

Although tornadoes have been studied extensively over the last fifty years, many unanswered questions remain regarding their development. The highly destructive nature and relatively small temporal and spatial scale of tornadoes make them difficult to measure directly. In addition, it is difficult and expensive to deploy a network of instruments to analyze the airflow in and around a tornado (e.g Rasmussen et al. 1994). Because of these observational limitations, numerical models have been used to study the structure and evolution of tornadic storms.

A particular type of numerical model—the idealized cloud model—has been used to study deep convective storms for over thirty years. This type of model typically consists of a horizontally homogeneous base state and horizontal grid spacing of 2 km or less. The dynamic core of the model consists of a set of equations that is used to predict the three-dimensional wind field, temperature, and pressure, and conserves mass. Processes that occur at a smaller scale than the grid spacing, such as the production and depletion of hydrometeors, sub-grid turbulence, and friction are represented through parameterizations—representations of complex physical processes necessary to produce realistic atmospheric phenomenon (Strensrud 2007). Despite simplifications in the model framework and deficiencies in the parameterization of certain physical processes, studies using idealized models have repeatedly produced simulated storms that are qualitatively similar to those observed in nature [e.g. Weisman and Klemp (1982, 1984); Brooks and

Wilhelmson (1993); Droegemeier et al. (1993); Brooks et al. (1994); McCaul and Weisman (2001); McCaul and Cohen (2002); Adlerman and Droegemeier (2005); Kirkpatrick et al. (2007,2009)].

If the model grid spacing is sufficiently small (i.e. ~ 100 m or less), it is possible to simulate tornado-like vortices that occur within the parent storm [e.g. Wicker and Wilhelmson (1995), Grasso and Cotton (1995), Finley et al. (2001), Gaudet and Cotton (2006a,b), Snook and Xue (2006), Lerach et al. (2008)]. The evolution of both the tornadic region of the simulated storm and the tornadic vortices themselves are very similar to that observed with Doppler radar [e.g. Dowell and Bluestein (2002), Wakimoto et al. (2004), Wurman et al. (2007, 2010)]. Thus, it seems that idealized models are capable of reproducing the storm-scale processes important to tornadogenesis. However, these simulations are computationally expensive and produce large output files—likely the reason only a handful of researchers have performed such simulations to date.

The main goal of this study is to advance the current understanding of tornadogenesis by simulating numerous tornadic and non-tornadic storms to determine the source(s) of vorticity-rich air at low levels and to also identify the processes that result in tornadogenesis and tornadogenesis failure. The idealized simulations are initialized with proximity soundings representative of the environments of tornadic and non-tornadic supercells. This study contains the largest number of tornado-resolving simulations to date and is also the first to compare numerous tornadic and non-tornadic simulations.

Before these simulations could be completed, new methodologies were needed. Due to the large number of simulations performed in this study, data mining techniques were developed to speed up analysis—specifically the automated, in-model detection of both supercells and tornadoes. Additionally, many of the proximity soundings used in this study fail to produce sustained storms when a 'traditional' convective initiation technique is used. In order to produce strong, sustained supercells, a new convective initiation technique was employed. Testing was performed to determine the optimal configuration for this new technique.

In Chapter 2, a general methodology used for all forthcoming simulations is discussed. Specific details of the methodology for each experiment are presented in that chapter. Results from the testing of automated supercell identification algorithms are presented in Chapter 3, and in Chapter 4 the convective initiation experiments are discussed. In Chapters 5, 6, and 7, results from the tornado-allowing simulations are presented. Chapter 8 provides a summary and conclusions for all experiments.

CHAPTER 2

METHODOLOGY

As previously mentioned, this chapter discusses the general methodology used in all simulations discussed herein. The simulations in each subsequent chapter required a specific methodology, the details of which are discussed in the individual chapters themselves.

Dataset

This study uses soundings taken within close spatial and temporal range to observed supercells (a.k.a., "proximity soundings") to initialize and provide boundary conditions for the simulations. Proximity soundings are assumed to represent the large-scale environment in which the supercells were embedded and have been used for decades to investigate environmental factors that produce tornadoes and other forms of severe weather. However, a standard definition of proximity sounding does not exist, and many past studies have used varying time and space criteria (see Table 2.1). Brooks et al. (1994) state these definitions of a proximity sounding are arbitrary, and that more analysis of the spatial and temporal variability of the environment is needed. Furthermore, Potvin et al. (2008) found that the definition of proximity can have a substantial effect on the statistical distribution of sounding derived parameters.

Recently, Thompson et al. (2003, 2007) used proximity soundings gathered from version 2 of the Rapid Update Cycle model and data assimilation system (RUC;

Benjamin et al. 2004) to study features of tornadic storms. The RUC-2 model used in their study has a horizontal gridspacing of 40 km and a temporal spacing of 1 h. By using modeled soundings as opposed to actual rawinsonde data, they were able to apply closer space/time proximity criteria than had previously been used (within 30 min and 40 km), resulting in a very large dataset of 897 supercell soundings. Thompson et al (2003) showed that the modeled RUC-2 soundings agreed well with nearby rawinsonde data and are believed to accurately represent the supercell environment.

The dataset used in this study is an expanded version of that used by Thompson et al. (2003, 2007). It is composed of 454 non-tornadic, 309 weakly tornadic and 134 significantly tornadic RUC-2 soundings. The significantly tornadic soundings are associated with supercells that produced tornadoes with F2 or greater intensity or lasted longer than 5 min. Thompson et al. (2003; 2007) showed differences in sounding parameters between the three classes, although with significant overlap. Due to time constraints, and because the sounding parameters overlap less between the non-tornadic and significantly tornadic datasets, the weakly-tornadic soundings will not be considered. Instead, this study focuses on the significantly tornadic soundings and an equal number of non-tornadic soundings.

Table 2.1. Summary of time and space criteria used for the definition of proximity soundings in select previous studies.

Study	Space Criteria	Time Criteria
Beebe (1958)	80 km	60 min
Darkow (1969)	80 km	105 min
Maddox (1976)	92.5 km	180 min
Davies and Johns (1993)	120 km	180 min
Rasmussen and Blanchard (1998)	400 km	NA

Description of the Numerical Model

Idealized simulations are carried out using the CM1 cloud model (Bryan and Fritsch 2002). The governing equations of CM1 are nearly identical to those developed by Klemp and Wilhelmson (1978),

$$\frac{\partial u}{\partial t} = -\vec{v}\cdot\nabla u - c_p\theta_\rho\frac{\partial \pi'}{\partial x} + K_m D_u, \tag{2.1}$$

$$\frac{\partial v}{\partial t} = -\vec{v}\cdot\nabla v - c_p\theta_\rho\frac{\partial \pi'}{\partial y} + K_m D_v, \tag{2.2}$$

$$\frac{\partial w}{\partial t} = -\vec{v}\cdot\nabla w - c_p\theta_\rho\frac{\partial \pi'}{\partial z} + g\frac{\theta_\rho - \theta_{\rho 0}}{\theta_{\rho 0}} + K_m D_w \tag{2.3}$$

$$\frac{\partial \pi}{\partial t} = -\vec{v}\cdot\nabla \pi - \frac{R_d}{c_p}\pi\left(\frac{\partial u}{\partial x} + \frac{\partial v}{\partial y} + \frac{\partial w}{\partial z}\right), \tag{2.4}$$

$$\frac{\partial \theta}{\partial t} = -\vec{v}\cdot\nabla \theta + \frac{1}{c_p\pi}\left(L_x M_\phi\right) - K_H D_\theta, \tag{2.5}$$

where $\overleftarrow{v}$ is the three-dimensional velocity vector (u,v,w), c_p is the specific heat of air at constant pressure, θ_ρ is the potential density temperature, π is the non-dimensional Exner function, g is gravity, K_M is eddy viscosity, R_d is the gas constant for dry air, θ is potential temperature, D_x represents sub-grid diffusion of variable x, L_x is the latent heat of either evaporation or sublimation, K_H is eddy diffusivity, and M_ϕ represents changes in θ due to microphysical processes (to be discussed later). Primed quantities represent perturbations from the initial base state and zero subscripts represent the base state value of that particular variable. The last term on the RHS of (2.1)-(2.3) and (2.5) is the turbulent stress tensor, and is presented using summation notation for brevity. In the original Klemp and Wilhelmson model, virtual potential temperature (θ_v) is used in the pressure gradient term in (2.1)-(2.3) instead of θ_ρ and M_ϕ only included phase changes between liquid and vapor, whereas the microphysics parameterization in this study also includes frozen hydrometeors.

Equations (2.1)-(2.5) are solved on a staggered Arakawa C grid (Arakawa and Lamb 1977) in the horizontal and a Lorenz vertical grid (Lorenz 1960). In this configuration, the components of the three-dimensional wind are solved at points that are offset from the remaining variables by ½ of the model grid spacing (Fig. 2.1). The model is integrated forward in time using a third order Runge-Kutta technique and fifth order spatial derivatives are used for the advection terms. The Klemp-Wilhelmson time splitting scheme is used, which integrates terms on the LHS of (2.1)-(2.4) (except those involving π) at a frequency specified by the large time step. A smaller time step is used to integrate (2.5) as well as the terms in (2.1)-(2.4) that involve π. This technique allows for minimal computation time while limiting the development of high-frequency longitudinal waves.

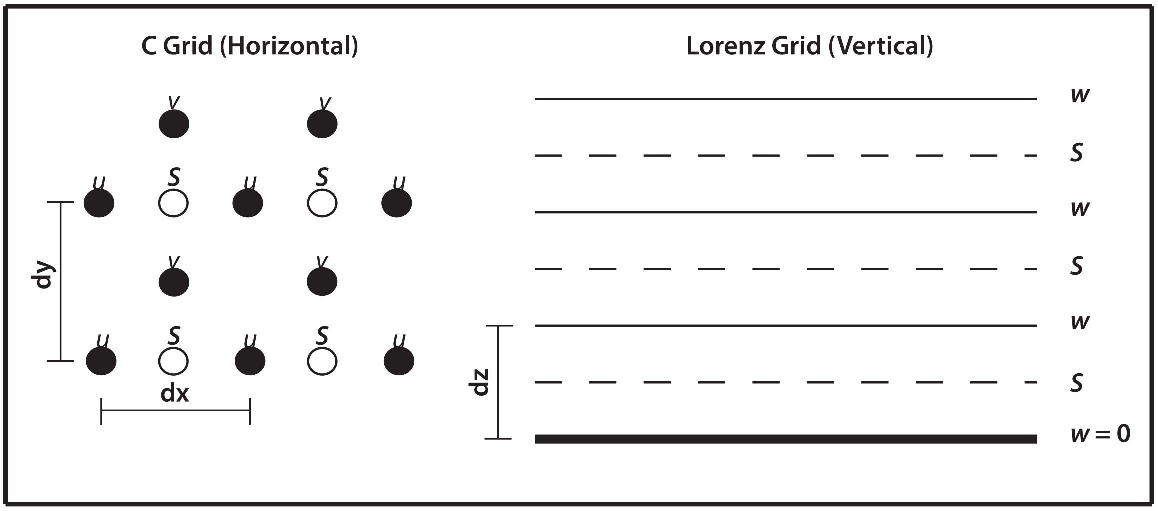

FIG. 2.1. Visual representation of the horizontal and vertical grid configurations in CM1. The components of the three-dimensional wind field are represented as *u*, *v*, and *w*, and *S* represents any thermodynamic or moisture variable (e.g. pressure, temperature, mixing ratio, etc.). Adapted from Purser and Leslie (1988) and Kalnay 2004.

Each simulation uses a 120x120x20 km computational domain. Longer simulations can be completed by using a moving grid determined by the 0–6 km mean wind of the input sounding. The lateral boundaries are gravity wave radiating and an additional Rayleigh damper is used within 10 km of the domain edge to eliminate partial reflection. The rigid upper and lower boundaries are free slip and a standard Rayleigh damping layer is applied above z=16 km to damp vertically-propagating gravity waves and minimize their reflection off the upper boundary. The Coriolis force is neglected and there are no terrain or surface fluxes.

Many of the RUC-2 soundings used in this study have layers characterized by small Richardson number (R_i) values. In these layers, turbulence production owing to shear is larger than buoyant turbulent production. If R_i is less than a certain critical value (typically assumed to be 0.25), the environment becomes unstable and convective overturning occurs. This could produce convective 'rolls' near the top of the boundary layer or even spurious convection throughout the model domain that could interact with the main supercell. To prevent this from happening, the turbulence scheme is modified to prevent overturning in the initial environment. Details are discussed in the 'Turbulence' section below. This is done by calculating the eddy diffusivity terms (K_m and K_h) in the initial environment and subtracting these values from the diffusivity terms at all later times.

Microphysics

The evolution of simulated supercells has been shown to be sensitive to microphysics parameterizations [e.g. Johnson et al. 1993, Straka and Rasmussen (1998) Gilmore et al. (2004), Li et al. (2008)]. The precipitation distribution within the storm and subsequent evaporative cooling influence the low-level cold pool and that has been shown to influence subsequent evolution. Observations suggest that outflow thermodynamics are also important to tornadogenesis [e.g. Markowski et al. (2003), Shabbott and Markowski (2006), Gryzch et al (2008)]. Thus, it would seem important that precipitation processes be parameterized as accurately as possible by perhaps using a multi-moment scheme with numerous hydrometeor categories. However, it has been recently shown that more complex microphysics do not necessarily produce more 'realistic' simulations. Milbrandt et al. (2010) found that a single-moment microphysics scheme produced simulations that more closely resembled observations than did simulations using double and triple-moment microphysics. Morrison and Milbrandt (2011) also note that it is incorrect to assume that the use of multi-moment parameterizations will produce more realistic simulations simply due to added complexity. Additionally, multi-moment microphysics parameterizations substantially increase computational duration and output file size. Because of the large number of high-resolution simulations being performed, it is it is important to minimize the computational load wherever possible. For these reasons, a simple, single-moment, bulk microphysics parameterization is used. This scheme is from Gilmore et al. (2004) and is based on the commonly used Lin et al. (1983) parameterization.

Six categories are represented in the microphysics—water vapor (q_v), cloud water (q_c), cloud ice (q_i), rain water (q_r), snow (q_s), and graupel/hail (q_g). Source and sink terms represented in this scheme are melting, evaporation, condensation, freezing, accretion, autoconversion, sublimation, deposition, aggregation, and hail/graupel shedding. Exponential distributions are used for q_g, q_r, and q_s (Marshall and Palmer

1948) with intercept parameters of 4x10^4, 3x10^6, and 8x10^6, respectively. Due to the single moment nature of this scheme, intercept parameters are constant throughout the simulation, with changes in mixing ratios resulting in changes only in the slopes of the distributions. Cloud ice and cloud water have a monodisperse distribution, with mass and diameter being a function of mixing ratio. Densities of water, snow, and graupel/hail are set at 1000, 100, and 900 kg m^{-3}, respectively.

Turbulence

Bryan et al. (2003) presented arguments based on the Kolmogorov microscale to show that a grid spacing of approximately 0.1 mm is needed to fully resolve all motions in deep convective storms. Since this is not feasible, subgrid-scale motions need to be parameterized to represent small-scale energy dissipation. Given that the scale of a supercell is tens of kilometers, and that the grid spacing used in the model is 100 m, a large-eddy simulation (LES) turbulence closure scheme is applicable. The LES closure scheme used in this study is based on Smagorinsky (1963), which assumes isotropic, steady-state turbulence, and is only active in areas of shear.

In this scheme, the turbulence coefficients, K_M and K_H, are determined using

$$K_M = (C_s\Delta)^2 S\left(1-\frac{R_i}{\mathrm{P_r}}\right)^{1/2} - K_{M\,BASE}\ , \tag{2.6}$$

$$K_H = \frac{K_M}{P_R} - K_{H\,BASE}\,, \tag{2.7}$$

where C_s is the Smagorinksy constant, P_r is the Prandlt number (~1/3), S is the square root of the deformation, $\Delta = (\Delta x \Delta y \Delta z)^{1/3}$,and $K_{H\,BASE}$ and $K_{M\,BASE}$ are the initial values of K_M and K_H. These terms are not in the original formulation, but were added to the K_M

and K_H calculations to ensure that the initial sounding is preserved, even when dynamic instability is present.

With traditional LES schemes it is assumed that the grid spacing is much smaller than the scale of the energy-containing eddies but much larger than the energy dissipation scale. With 100 m grid spacing, these assumptions are valid when considering the supercell scale but they are not true for tornado scale circulations. Because of this, the simulations in this study will be referred to as convective-resolving (referring to the main updraft) and tornado-allowing. This distinction is important because it demonstrates some limitations of this study. The storm scale processes responsible for tornado formation and maintenance should be well resolved. However, only the basic structure of the larger tornadic vortices will be captured and they are likely to be dampened due to the turbulence parameterization applied at the chosen resolution. Tornado vortices have a scale of O[100 m], the same as the proposed model grid resolution for this study, so many smaller tornadoes that might otherwise be simulated will not appear. Wyngaard (2004) states that turbulence closure schemes were not designed for use when the scale of the energy-containing eddy is the same size as the grid resolution. For this reason, it would be inappropriate to make conclusions about the detailed structure of the tornadoes themselves (i.e. presence of multiple vortices, corner flow structure, etc.). Rather, the focus will be on the storm scale processes that promote the *presence* of tornadic vortices.

Convective Initiation

Since Klemp and Wilhelmson (1978), in most idealized three-dimensional modeling studies of supercells convection has been initiated by placing a thermal perturbation in the center of the domain at the initial time step. Due to buoyancy, this thermal ‘bubble’ rises and, in the appropriate environment, it will grow into a strong, well-developed convective updraft. However, many of the RUC-2 soundings have strong capping inversions, and the thermal bubble technique fails produce strong, sustained convection in those cases because the capping region disrupts the ascent of the thermal bubble when the bubble becomes negatively buoyant relative to the environment. In these environments, a low-level upward perturbation pressure gradient force driven by horizontal convergence is needed to maintain the updraft beneath the level of free convection (LFC). By using a convective initiation technique that is applied for multiple time steps, the low-level wind fields will have time to adjust and produce the convergence needed to maintain the required perturbation pressure gradient force.

The convective initiation approach used in this study will be referred to as updraft nudging (UN) and was used recently by Zeigler et al. (2010). In this technique, a spheroid is defined with specified x, y, and z origins and lengths. At all points inside the spheroid, the w field is gradually increased towards a maximum w threshold (w_{max}) following

$$w_{mag} = \begin{cases} w_{max} cos^2\left(\frac{\pi}{2}\beta\right), & \text{if } 0 \leq \beta \leq 1 \\ 0, & \text{if } \beta > 1 \end{cases} \tag{2.8}$$

$$w_t = w_{t-1} + dts \times \alpha \times \max\,(w_{mag} - w_{t-1}, 0), \tag{2.9}$$

where β is the distance from the center of the spheroid normalized by its radius, α is the acceleration constant, dts is the small model time step, and the max function insures that nudging is not applied once the vertical velocity exceeds w_{max}. The degree to which the w field is increased depends upon α and the distance from the center of the spheroid. Nudging is strongest in the center of the spheroid and decays to zero at its edges. The UN is applied at each small model time step for a defined period of time (t_{LUN}).

However, because this technique is new, the parameter settings needed to maximize storm potential are unknown and require testing. These tests are discussed in Chapter IV. UN experiments are aided by the use of an objective and automated method for defining the presence, strength, and duration of a supercell (Chapter III).

Logistics of the Simulations

Simulations in Chapters 3 and 4 were performed on resources located at the Texas Advanced Computing Center (TACC). The simulations were executed on a Dell Linux cluster with distributed memory (nicknamed ‘Lonestar’). Lonestar has over 62,000 processing cores and is capable of a peak performance of 302 TeraFLOPS. These simulations used 36 processors each. Each of these simulations generates less than 100 MB of data. The tornado-allowing simulations in Chapters 5 and 6 were performed at the National Institute for Computational Sciences (NICS) on a Cray XT5 (nicknamed ‘Kraken’). Kraken has over 112,000 processors and a peak performance of 1.17 PetaFLOPs. Testing on Kraken has shown that CM1 has nearly perfect scaling up to 2304 processors (meaning that as the number of processors increases, there is a proportional decrease in the amount of time needed to perform the simulation). These tests have also shown that the optimal balance between simulation run time and supercomputing unit (SU) usage is achieved when 576 cores are used for each simulation (Fig. 2.2). When run with 576 compute cores, each simulation (of 2 hours cloud time) finished in approximately 11 hrs.

Each of the tornado-allowing simulations produces hundreds of gigabytes of model output. However, the storm (and tornado) only occupies a very small portion of the overall model domain. Because CM1 writes 576 separate model history files (one from each processor) at each output time in a tiled manner across the domain, this results in the creation of thousands of output files for each simulation. By using the automated analyses developed in Chapters 3 and 4, information regarding supercell strength/presence and tornado presence is written to a standard output ASCII text file. This information was used to determine which simulations contain supercells and if/when tornadogenesis occurred. Cases that did not produce a supercell were discarded, along with output files from the supercell producing simulations not associated with the time of tornadogenesis or tornadogenesis failure. Thus, the actual amount of retained data was a fraction of the above-listed total.

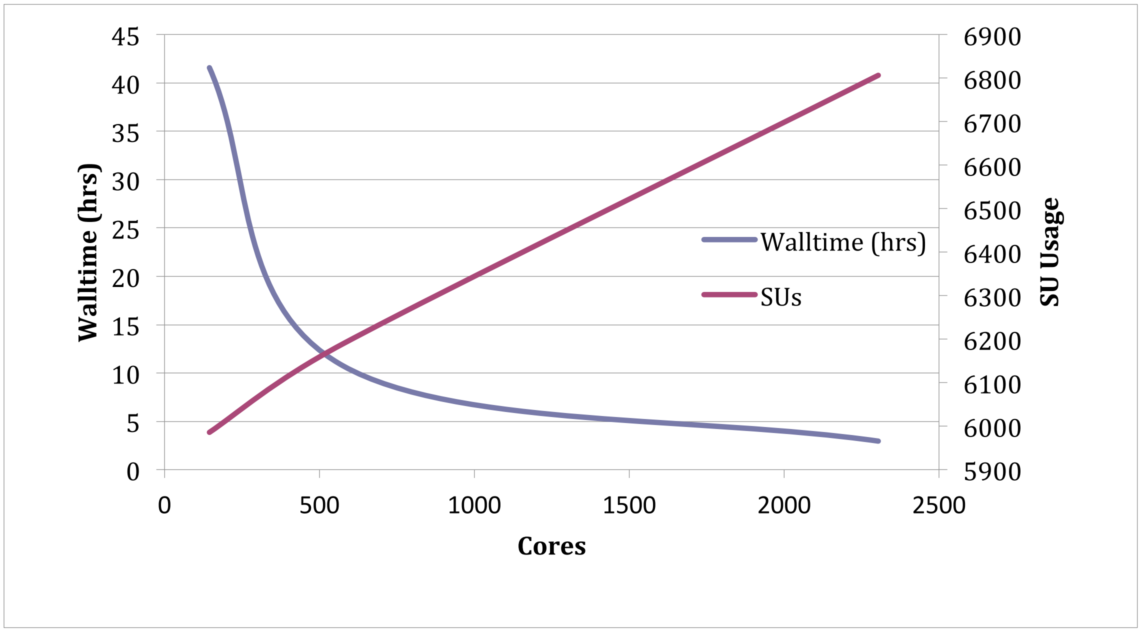

FIG. 2.2. CM1 performance as a function of total number of computing cores used.

CHAPTER 3

AUTOMATED SUPERCELL DETECTION

Introduction

In order to determine which convective initiation technique produces the longest-lived supercells, an objective definition of a supercell is first needed. The formal American Meteorological Society (AMS) definition of a supercell is: "an often dangerous convective storm that consists primarily of a single, quasi-steady rotating updraft, which persists for a period of time much longer than it takes an air parcel to rise from the base of the updraft to the summit" (Glickman 2000). However, this does not provide a quantitative means of defining a supercell.

Efforts to distinguish supercells from other modes of convection in short-term forecasts using storm-scale simulations have been performed as a part of STORMTIPE and other spring programs at the National Severe Storms Laboratory since the early 1990s (e.g., Brooks et al 1993; Wicker et al. 1997). These studies focused on using grid point soundings taken from operational models to initialize an idealized cloud model with a limited domain. Recently, it has been shown that information obtained from convective-allowing (i.e. 4 km or less horizontal grid spacing) operational models can help improve severe weather forecasts by giving insight into the general characteristics and mode of forthcoming convection (Kain et al. 2006, Weisman et al. 2008). Even though all of these studies used numerical model forecasts in some manner to predict convective mode, none offer a quantitative definition of a supercell. With the possibility of an operational warn-on-forecast system based on output from numerical models (Stensrud et al. 2009) being implemented in the near future, a rigorously tested, quantitative supercell definition could be useful for issuing warning products based on such a system.

There is also interest in the research modeling community for identifying and processing supercell characteristics for a large number of simulations (B. Jewett 2011, personal communication). High performance computers are now capable of performing a large number of simulations in a short period of time. However, it can be time consuming and tedious to manually examine the output from many simulations for the presence of supercells. Analysis time requirements of large suites of simulations could be greatly reduced through use of an automated supercell detection technique.

To date, there has been no known systematic comparison of the performance among the available supercell identification algorithms. This paper describes a systematic effort in testing the performance of three automated supercell identification methods for simulated storms at 1-km horizontal grid spacing, which, while considered coarse for research, will soon be used in storm-scale forecast models. This resolution has been shown to be sufficient for capturing the basic structure of deep convection (Bryan et al. 2003).

Distinctive radar characteristics of supercells were noted long before their recognition as a separate mode of convection by Browning (1964). Newton and Katz (1958) first observed that these storms move to the right relative to the mean environmental winds. Stout and Huff (1953), Fujita (1958), and Browning and Donaldson (1963) observed hook shaped appendages in images of radar reflectivity factor. The 4 May 1961 Geary, OK storm (Browning and Donaldson 1963) and the 9 July 1959 Wokingham, England hailstorm (Browning and Ludlam 1962) were both found to possess an echo-free region—now known to be coincident with a strong updraft.

The presence of these distinctive features has been used as the basis for the conceptual model of a classic supercell (e.g., Browning 1964; Marwitz 1972; Lemon and Doswell 1979). Numerous studies since have used these models in some manner as criteria for supercell identification (e.g., Lemon 1977; Brooks et al 1994; Moller et al. 1994; Thompson 1998; Klimowski et al 2003; Thompson et al. 2003; Bunkers et al. 2006). Some of these studies also included threshold values of Doppler radar-detected horizontal wind shear to aid in subjectively determining mesocyclone presence.

Doswell and Burgess (1993) argue that radar features are inadequate for categorizing convective storms. Reflectivity hooks and bounded weak echo regions (BWERs) may not be evident in heavy- or low-precipitation supercells (Moller et al. 1994), rightward storm propagation may be small (Davies and Johns 1993; Moller et al. 1994), and range limitations might cause a supercell to be missed due to smoothing of the velocity signature. Since the distinctive radar-observable characteristics of a supercell (i.e., hook echoes, rightward propagation, BWER) are related to the presence of a mesocyclone, it seems that a more direct definition of a supercell would involve a quantitative means of detecting the presence of a mesocyclone. However, as mentioned by Moller et al. (1994), a universally accepted definition of a mesocyclone does not exist.

A quantitative approach to defining a mesocyclone commonly used in numerical modeling is to examine the linear correlation between vertical velocity (w) and vertical vorticity (ζ). However, as is the case with radar-based mesocyclone detection, a standard methodology for this technique has not been defined. Using three-dimensional models and multi-Doppler radar data, Clark (1979) found linear correlation coefficients as high as 0.4. The correlation was performed on all points over a depth of 2–10 km. Weisman and Klemp (1984) similarly calculated the linear correlation for an idealized, right-moving supercell, but only for grid points with $w > 0$ m s^{-1}, within a 15-km × 15-km box centered on the storm and averaged over the lowest 8 km. Their results show correlation values ranging from 0.5–0.8. Droegemeier et al. (1993) followed Weisman and Klemp (1984) except using $w > 1$ m s^{-1}. The analysis window was centered on the storm with a size specified to minimize influence from nearby convection (S. Lazarus 2011, personal communication). Their results yielded correlations as high as 0.7 for supercells and 0.78 for multicells, with the distinguishing characteristic between the two storm types being the longer duration of the correlation for supercells. Knupp et al (1998) defined a supercell as a storm with a w–ζ correlation of 0.4 or greater over 1/3 of the storm depth that lasts for at least two updraft-parcel cycles. Their version of correlation was calculated using only points where $w \geq 3$ m s^{-1}. None of these studies tested their respective objective threshold values using a sample size larger than a few cases.

Recently, Kain et al. (2008) and Sobash et al. (2011) presented the concept of updraft helicity (UH) as a method for mesocyclone detection in convection-allowing operational models. UH is the local product of w and ζ integrated over a specified depth (equation 3.2, discussed below). Kain et al. (2008) used a UH threshold of 50 $m^2 s^{-2}$ to define mesocyclones in their 2-km WRF runs, with a smaller threshold found to be appropriate for 4-km simulations. Sobash et al. (2011) tested UH thresholds in their 4-km WRF runs with values of 34–103 $m^2 s^{-2}$. However, these thresholds were determined by comparing model *forecasted* storm structure to the number of radar-observed mesocyclone detections; and thus it was as much a test of whether the model captured the proper environmental conditions and convective mode as it was of the proper UH thresholds. This comparison was only available once per hour, and some loss of forecast skill may have resulted from the coarse temporal resolution.

The purpose of this chapter is to evaluate the skill of various objective supercell identification techniques by using an idealized numerical cloud model initialized with a large number of RUC-2 proximity soundings that were associated with supercells in nature. The modeled storms are classified based on their simulated radar reflectivity structure and presence of vertical vorticity, then compared to objective techniques to determine which approach (and threshold) has the most skill in detecting and identifying supercells.

Methodology

Dataset

Each idealized simulation was initialized using a subset of the RUC-2 proximity soundings discussed in Chapter 2. The subset used here is the 113 significantly tornadic soundings representative of a *mature* supercell. Twenty-one of the 134 total significantly tornadic soundings were not considered because they were taken before the storm reached peak maturity and are more representative of the initiation environment. It has been previously shown that the storm initiation environment can differ from that of the mature storm (e.g. Zeigler et al. 1997,2001).

Since simulated storm structure is primarily a function of environmental CAPE and vertical wind shear (e.g. Weisman and Klemp 1982,1984), most of the storms produced in the simulations using these soundings possess at least some supercell characteristics (i.e. midlevel rotation) at some point in their lifetime. The simulated storms produced by using the selected soundings include strong, isolated, long-lived supercells, rapidly decaying supercells with weak updrafts and lingering midlevel rotation that pose no severe threat, multicell clusters, and some quasi-linear convective systems. The analysis focused on only right-moving supercells, if present (i.e. left moving supercells are not considered). Even though not all types of convection are represented in this study, we believe that the simulations offer a good testbed for the mesocyclone identification algorithms presented herein, because some rotation is present in nearly every case.

Numerical Model Setup

The model setup consisted of 1-km horizontal grid spacing and 250 m vertical grid spacing within a 120-km × 120-km × 20-km domain. The large time step was 3 s for advection and the small time step was 0.5 s. All other settings are identical to those discussed in Chapter 2.

Convection was initiated using the updraft nudging technique discussed in the previous chapter. The nudging was performed for the first 1800 s of cloud time over a 10-km × 10-km × 3-km spheroid centered at z = 1.5 km. The w field at all points inside this spheroid was accelerated towards a maximum value of 10 m s^{-1}, with the strongest nudging at the center of the spheroid and falling off to zero at the edges. The nudging settings were chosen such that every simulation produced a storm that lasted at least 30 min.

Subjective Analysis

The criteria used for categorizing a storm as a supercell was designed to mimic that of Thompson et al. (2003) as closely as possible. That is, a storm was considered a supercell at a particular instant if all of the following criteria were met:

- The storm possessed one or more of the radar reflectivity characteristics typically associated with supercells (hook echo, inflow notch, BWER)
- Vertical vorticity > 0.004 s^{-1} was present in an area likely to be coincident with updraft. By definition, the vorticity value used is twice the ΔV shear value used by Thompson et al (2003).

In order to perform this analysis, model history files were analyzed at 5 min intervals for each simulation. The analysis consisted of a visual inspection of horizontal plots of simulated radar reflectivity factor (computed following Smith et al. 1975) and specified contours of vertical vorticity at z=875 m and z=4875 m. These levels were chosen because they roughly estimate the upper and lower bounds of possible radar beam heights of the data in Thompson et al. (2003)[1]. In addition, the use of multiple heights allows inferences to be made about the depth of the rotation and also the presence of a bounded weak echo region.

At every analysis time, the storm was subjectively categorized as a supercell or non-supercell by several contributors ("1" for supercell, "0" for non-supercell). A storm at a particular instant was classified as a supercell if the composite score was greater than 0.5, and a non-supercell is otherwise. The results from the composite analysis are considered 'truth' for the sake of comparisons with the objective classification techniques.

Although general subjective identification guidelines were established, there was some freedom in interpretation. For instance, no criteria were specified regarding time scales, whether threshold rotation was required at both levels, spatial continuity between rotation at both levels, threshold values of simulated radar reflectivity factor, or the alignment of vertical vorticity relative to reflectivity structures.

---

[1] Thompson et al. (2003) analyzed 0.5° and 1.5° WSR-88D elevation scans. Assuming storms were within 200 km of the radar location, the maximum height of the radar beam would have been approximately 5.2 km AGL.

Objective Classification Techniques

Pearson Correlation Coefficient

The Pearson correlation coefficient (PC) (e.g. Wilks 2006) between vertical velocity and vertical vorticity is defined as

$$R = \frac{w'\zeta'}{\sigma_w \sigma_\zeta}, \tag{3.1}$$

where w is vertical velocity, ζ is the vertical component of vorticity, σ is the standard deviation, and primed quantities indicate the deviation from the mean. This correlation generally has been calculated using only grid points with positive vertical velocity, within an analysis window selected to capture the updraft region of a particular storm. The single correlation value computed in (3.1) for each altitude is then averaged over some vertical depth. Previous studies have used different sub-region sizes, storm-selection criteria, averaging depths, and minimum w criteria for selecting grid points; and all of these choices influence the calculation.

In this study, PC was standardized to a single 9-km × 9-km analysis window centered on the maximum domain updraft at 6 km—similar to the method used in the studies cited above. This sub-region size was selected because it is the approximate size of supercell updrafts from historical idealized simulations with 1-km resolution (e.g. Klemp and Wilhelmson 1978; Weisman and Klemp 1984; Rotunno and Klemp 1985). Thus, this sub-region should encompass the main convective updraft of a storm and limit the likelihood of nearby weaker updrafts from influencing the correlation value. Testing was performed to determine which settings for minimum w value and vertical averaging depth result in the best supercell detection as defined by the threat score[2]. Minimum w thresholds used were 3 m s^{-1}, 5 m s^{-1}, 7 m s^{-1} and 9 m s^{-1}; and the vertical averaging depths tested were 1–6 km, 1–8 km, and 2–5 km. Previous studies have included levels below 1 km, however these levels were not considered for testing herein because the presence of near-surface rotation is not essential for a storm to be classified as a supercell.

Modified Pearson Correlation

There are several drawbacks to the traditional application of the Pearson correlation. The first drawback is the lack of information regarding the spatial structure of a mesocyclone, since only one correlation coefficient is calculated for a single storm. The second drawback is the need to define an analysis window only around the storm of interest without including other strong left-moving supercells or multicells. As mentioned above, the presence of multiple updrafts in the correlation sub-region may dilute the magnitude of the correlation and scenarios such as storm splitting and storm occlusion may not produce a strong w–ζ correlation when considering the multi-updraft storm complex as a whole. While manual placement of the analysis window has been successful in past studies, simple algorithms to automate its placement can fail to provide a representative PC value when multiple storms are present in the domain.

As an alternative approach to the traditional Pearson Correlation, a modified Pearson correlation (MPC) was developed herein. It was calculated by applying

---

[2] Only fixed depths are used in tests of vertical averaging depth. More sophisticated techniques like that used by Knupp et al. (1998) are being tested to determine if they offer improved skill over fixed depths.

(3.1) at each horizontal grid point using a smaller 3-km × 3-km subset of surrounding grid points (i.e., 9 total points for the dx=1 km simulations) and then averaging over a defined vertical depth. The size of this subset was chosen so that only a portion of the updraft was considered for reasons discussed above. MPC at a particular point was set to zero if <4 (44% of the area at 1-km grid spacing) of the points in the subset exceeded a defined *w* threshold (discussed below). This was done in order to filter out points with little or no updraft, and to make sure that the correlation was not being computed on the very edge of the updraft. This method should ensure that the maximum possible correlation is obtained everywhere in the domain, so that the user can be more certain to extract the maximum PC value for each storm of interest without concern for placement of the analysis window. Thus, it is less sensitive to user error and potentially better for automation. The presence of a supercell was determined herein by the domain-maximum value of MPC. As with the traditional PC, testing was conducted to determine the influence of *w* threshold and averaging depth on the reliability of this technique. Minimum *w* thresholds and vertical averaging depths were the same as for the PC method.

Updraft Helicity

As discussed by Kain et al. (2008), updraft helicity is the vertical component of helicity integrated over a specified depth,

$$UH = \int_{z_b}^{z_t} w\zeta dz, \tag{3.2}$$

where z_t and z_b represent the upper and lower integration limits, respectively. Equation (3.2) was calculated at every point in the horizontal domain. The presence of a mesocyclone was determined based on the domain maximum value of UH. Kain et al. (2008) used z_b and z_t values of 2 km and 5 km, which is a shallower layer than typically has been used in other objective identification techniques. Using a deeper layer for the integration may produce better results. Thus, for a fair comparison to the PC and MPC techniques, the vertical layers of 1–6 km and 1–8 km were tested in addition to 2–5 km.

Verification of Automated Techniques

Comparisons between the subjective and algorithm results were made using a 2×2 contingency table (e.g., see Wilks 2006). For the purposes of this analysis, the subjective results were considered to be observational truth and the results from the automated algorithms are being verified. The accuracy of the automated techniques was evaluated based on threat score—defined as the ratio of hits to the sum of hits, misses, and false alarms. Threat score was chosen for verification because it does not consider correct non-events; thus high threat scores only can be achieved by minimizing both false alarms and misses. The detection threshold was systematically varied for each automated technique (0.1 to 1 for PC and MPC and 0-400 for UH) and the threat score was calculated at each detection threshold. The Heidke skill score does include correct non-events and also was tested, but is not shown because the results produced the same optimal configuration for each automated technique as the threat score analysis.

Results

By 1200 s, all simulations produced a storm with a strong updraft, areas of large simulated reflectivity, and at least some vertical vorticity. In order to reduce the number of correct non-events resulting from times with no storm, analysis of the cases begins at *t*=1200 s. Note that by beginning the analysis at *t*=1200 s, the first few analysis times occur while updraft nudging is still enabled (See Chapter 4 for details of how updraft nudging affects supercell structure). A total of 2373 snapshots were obtained by analyzing each of the 113 simulations at 5 min intervals between 1200 and 7200 s. However, some of these instances were removed from consideration because the automated analysis window needed for the PC technique had moved temporarily to a different storm in the domain (i.e. a different storm than was subjectively analyzed). After removing these occurrences, 2099 instances were left. From the subjective analysis, the dataset contains 1188 instances in which a supercell is present and 911 instances of non-supercells. At no point in any of the simulations were multiple supercells present simultaneously. Of the instances classified as non-supercells, 563 (62%) are because of a lack of strong updraft in the domain (i.e., no storm).

In the upcoming sections, the following nomenclature is used to discuss a particular configuration: [*technique name*][*minimum w threshold*]w[*depth*]. For example, pc3w25 refers to a Pearson Correlation configuration using a minimum *w* threshold of 3 m s^{-1} and averaging over 2-5 km.

Pearson Correlation

Figure 3.1 shows that, for all configurations, the threat score is maximized using a detection threshold of 0.1, and decreases with increasing detection threshold. The small spread in threat scores at detection threshold 0.1 indicates that PC performance at this threshold is not strongly influenced by configuration (i.e., averaging depth and minimum *w* threshold). The spread in threat scores increases at larger detection thresholds, suggesting that configuration settings become more influential. Although the spread in threat scores increases, the general tendency of the results remains the same. For a given *w* threshold, threat scores are largest when using an averaging depth of 2–5 km and smallest when using an averaging depth of 1–8 km.

The PC configuration that produces the largest threat score was that having a minimum updraft value of 7 m s^{-1} and averaging from 2–5 km (pc7w25) with a detection threshold of 0.1. A contingency table for this configuration, using a detection threshold of 0.1, is shown in Fig. 3.2. While there are 1732 instances when the subjective and automated methods agreed (1036 hits and 696 correct non-events), there are also 367 instances (215 false alarms and 152 misses) in which the two methods disagreed. These disagreements result in a false alarm ratio of 0.1713 and a relatively low hit rate of 0.8721.

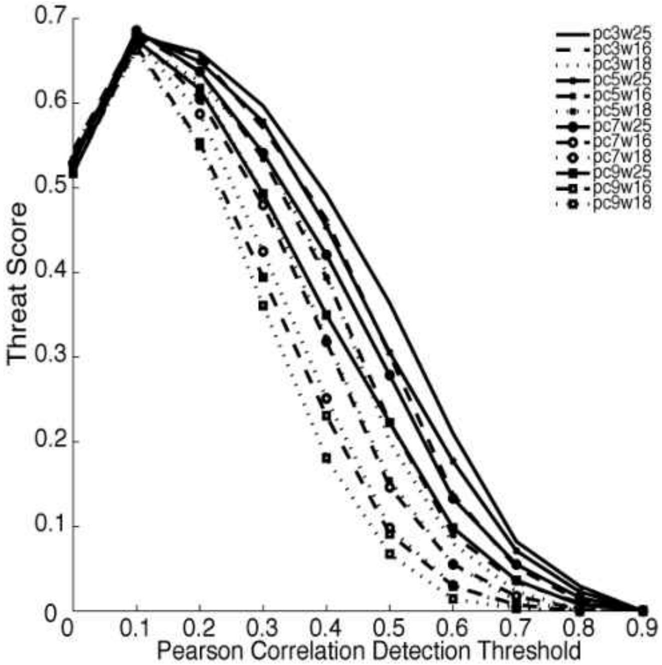

FIG. 3.1. Threat score vs. detection threshold for various configurations of the Pearson Correlation.

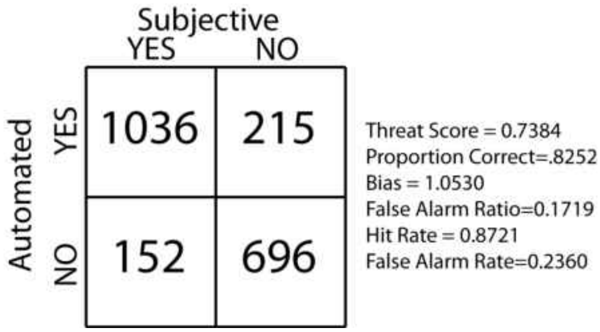

		Subjective	
		YES	NO
Automated	YES	1036	215
	NO	152	696

Threat Score = 0.7384
Proportion Correct=.8252
Bias = 1.0530
False Alarm Ratio=0.1719
Hit Rate = 0.8721
False Alarm Rate=0.2360

FIG. 3.2. Contingency table and statistics for the Pearson Correlation configuration using only points with $w > 7$ m s^{-1} and averaging from z=2-5 km.

Modified Pearson Correlation

Maximum threat scores using the MPC method are nearly 0.05 larger than the PC method, with every configuration producing a larger threat score than the optimal PC configuration (Fig. 3.3). The variation in the threat scores among particular configurations is much greater relative to that for the PC method; however, several configurations did produce very similar threat scores at particular detection thresholds. As with the PC method, for a specific updraft threshold, the configuration using an averaging depth of 2–5 km produces the largest threat score. Overall, the largest threat score is achieved for mpc7w25 with a detection threshold of 0.3. A contingency table for the mpc7w25 configuration is shown in Fig. 3.4. Even though this is the same depth and *w* combination that was found to produce the largest threat scores for the PC technique, the MPC technique yields more hits and substantially fewer misses than the optimal PC configuration, resulting in a much larger hit rate (0.9369). The number of false alarms and correct non-events remains fairly similar.

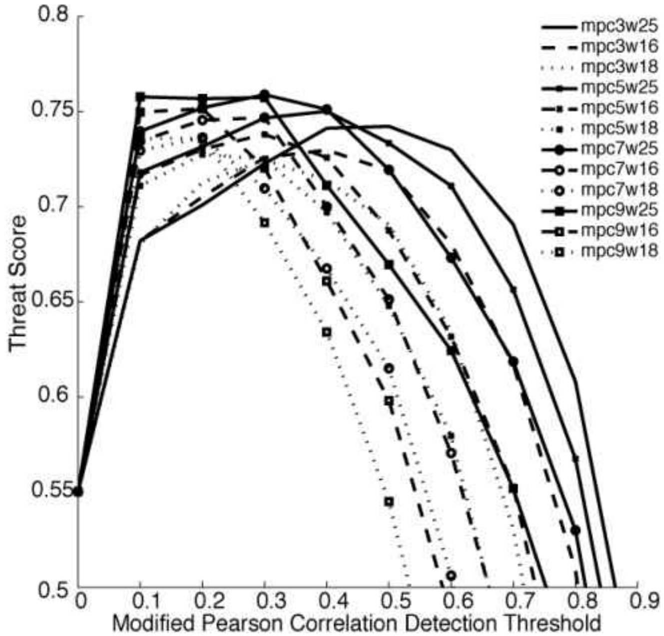

FIG. 3.3. Threat score vs. detection threshold for various configurations of the Modified Pearson correlation.

		Subjective YES	Subjective NO
Automated	YES	1113	230
	NO	75	681

Threat Score = 0.7849
Proportion Correct=.8547
Bias = 1.1305
False Alarm Ratio=0.1713
Hit Rate = 0.9369
False Alarm Rate=0.2525

FIG. 3.4. Contingency table and statistics for the modified Pearson Correlation configuration using only points with $w > 7$ m s^{-1} and averaged from z=2-5 km.

Updraft Helicity

The UH technique produces slightly larger threat scores (about 0.78) than the optimal MPC configurations (c.f., Figs. 3.3 and 3.5). As with the previous two techniques, the configuration using the 2–5 km layer produces the largest threat scores. However, recall that for the UH technique the values are integrated over this depth, while in the PC and MPC techniques the values are averaged over the depth.

As integration depth increases, larger threshold values are needed to produce a maximum in threat score (Fig. 3.5).

The largest threat score for depths considered here is achieved using an integration depth of 2–5 km and a detection threshold of 180 m^2 s^{-2}. Fig. 3.6 shows that this UH configuration produces more hits and fewer misses than the optimal PC and MPC techniques, yielding the largest hit rate of the three techniques. The total number of false alarms is slightly less than with the MPC and PC techniques.

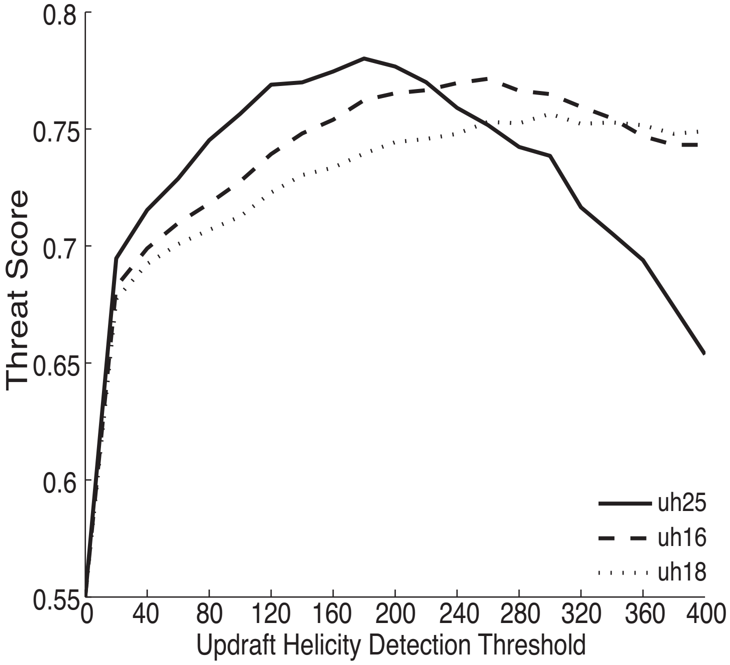

FIG. 3.5. Threat score vs. detection threshold for various configurations of updraft helicity.

		Subjective	
		YES	NO
Automated	YES	1126	204
	NO	62	707

Threat Score = 0.8089
Proportion Correct=.8733
Bias = 1.1195
False Alarm Ratio=0.1534
Hit Rate = 0.9478
False Alarm Rate=0.2239

FIG. 3.6. Contingency table and statistics for the updraft helicity method integrated from z=2-5 km.

Comparison of Automated Technique Performance

To demonstrate differences in how the various automated techniques perform under their optimal settings, a case was chosen for additional analysis in which the automated techniques disagreed on storm type. The case involves a storm that was subjectively classified as a supercell at all times between t=1200 s and t=7200 s. Both the optimal MPC and UH techniques agree with the subjective classification at all times. However, the PC technique fails to detect this storm as a supercell at numerous times throughout the simulation. This case was initialized with a RUC-2 sounding from Waterloo, IA on 12 May 2000[3]. The sounding and hodograph are shown in Fig. 3.7.

By t=1200 s, the storm begins to develop common supercell characteristics such as a hook-shaped appendage and a BWER. Values of ζ exceed 0.01 s^{-1} at both z=875 m and z=4875 m. Over the next 600 s, the storm continues to grow in size but maintains its overall structure. By t=1800 s, there is evidence of storm splitting at midlevels and by t=3000 s a left moving multicell cluster is clearly distinguishable

---

[3] For this study, it is not necessary for the modeled storm to match the structure/evolution of the observed storm

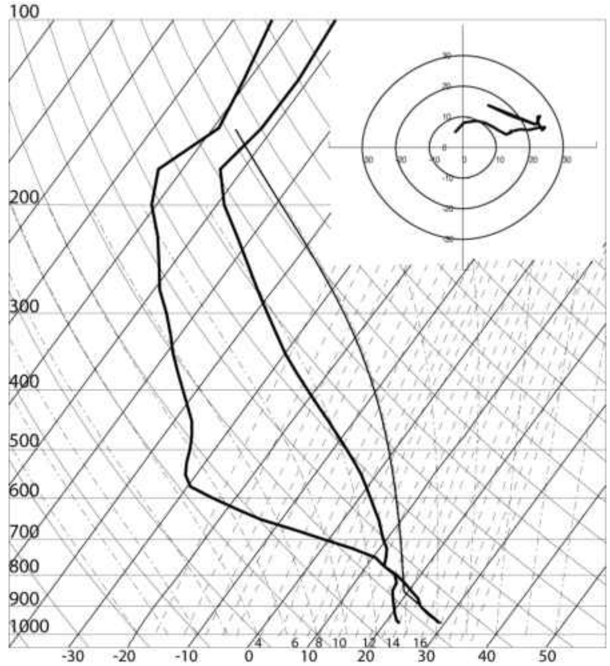

FIG 3.7. Skew-T and hodograph of RUC-2 data used to initiate the simulation discussed in this section.

from the right moving supercell. Up to this point, all three automated techniques classified this storm as a supercell. At t=3300 s, the PC technique produces a correlation of 0.05, which is below the established optimal threshold of 0.1. The UH technique produces a maximum value of 714 $m^2 s^{-2}$, while the MPC technique produces a maximum value of 0.5. Both of these values are well above the optimal supercell detection thresholds established in previous sections. This trend continues until t=4200 s, when the PC value again exceeds the detection threshold. To determine why the PC method stops classifying this storm as a supercell after t=2700 s, this time period is analyzed in more detail.

At t=2700 s, the storm possesses a strong, circular, midlevel updraft centered slightly to the northeast of the low-level hook echo (Fig. 3.8a). A large portion of the updraft inside the PC analysis window is coincident with positive values of ζ. At this time, MPC and UH values are large over most of the updraft, and PC is 0.44. There is good spatial agreement between the UH and MPC methods as to the placement of the mesocyclone, since the contours of these values have significant overlap. Thus, it is clear why all three methods classified the storm as a supercell.

By t=3900 s, the region of $w > 7$ m s^{-1} at z=4875 m increases along the rear flanking line giving the overall updraft a more elongated appearance (Fig. 3.8b). UH values exceeding the detection threshold are located primarily ahead of the hook echo in the weak echo region, coincident with the strongest region of updraft. Maximum UH at this time is 378 m^2 s^{-2}. MPC values exceeding the detection threshold are located further to the southwest, in a region coincident with the hook echo and flanking line. Inside the PC analysis window, however, there is less overlap between contours of updraft and positive ζ than at t=2700 s. This is likely why the PC value has decreases to –0.06 at this time. A test was performed to determine if PC values would be increased by only including points with positive ζ, in addition to exceeding the minimum w threshold (not shown). This test did not improve forecast skill and actually yielded lower PC values at many times. The large 9-km × 9-km box in the PC method may have caused the storm to not be detected as a supercell. To test this theory, a 3-km x 3-km box was used (as in the MPC method), but still centered on the max updraft. This resulted in a PC value of –0.37 at t=3900 s, meaning that, for this particular case, the placement of the correlation window is at least as important as the size of the window.

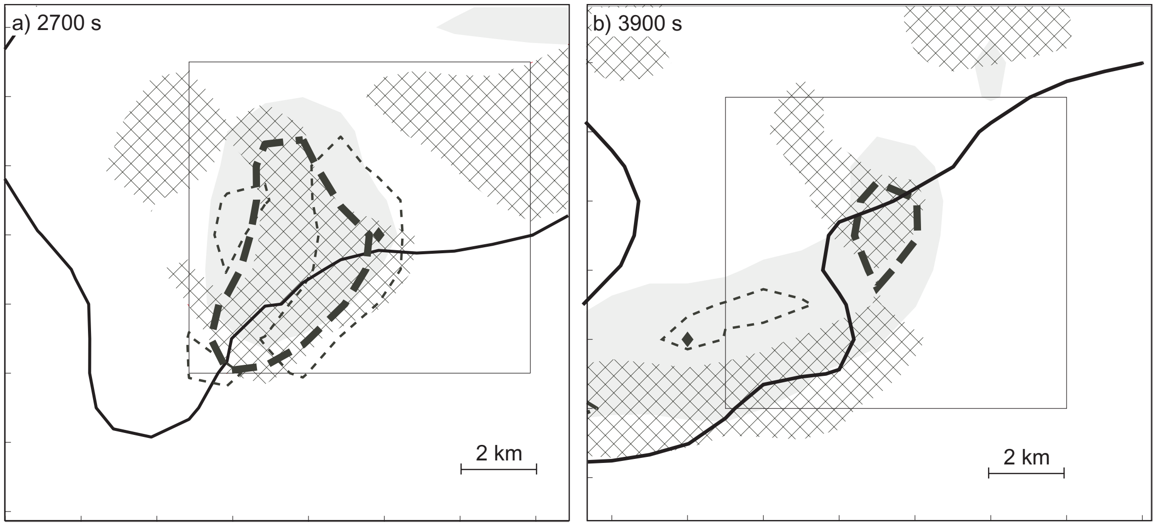

FIG. 3.8. Storm plan view at a) t=2700 s and b) t=3900 s. The thick solid line is the 40 dBZ simulated reflectivity contour at z=675 m; hatched areas are ζ >=0.004 s^{-1} and shaded areas are w >= 7 m s^{-1} (both at z=4875 m). Thin dashed lines are MPC >= 0.3 and thick dashed lines are UH >= 180 m^2 s^{-2}. The black rectangle represents the analysis window for the PC calculation. The diamond marks the location of the MPC maximum. Tick marks are 2 km apart.

Temporal Criteria

The results presented above demonstrate the ability of the automated techniques to detect supercell characteristics at a specific point in time. However, the AMS definition of a supercell includes a stipulation that the rotating updraft be present for some period of time. The goal of the analysis presented in this section is to determine if the false alarms present in the automated techniques have shorter durations than the positive detections (hits). Because the PC technique had lower skill than the MPC and UH techniques, and because of the numerous instances in which samples were disregarded due to improper automated placement of the PC analysis window, it is not considered in this analysis. With PC technique thus disregarded, it is no longer necessary to remove times when the PC analysis box was placed incorrectly. All times from t=1200–7200 s for all cases are used for this subsequent analysis.

Instantaneous false alarms were grouped together based on the number of consecutive instances, with the same procedure applied to positive detections. For example, a case with six consecutive positive detections would be categorized as one 'hit' that lasted for 1800 s (30 min). Detection of four consecutive false alarms would be categorized as a singular false alarm with duration of 20 min.

For both the MPC and UH cases, a large proportion of the false alarms have a duration of ≤20 min (Figs. 3.9b & d), while only a small proportion of the hits persist for <20 min (Figs. 3.9a & c). There are two scenarios that could produce short-lived false alarms: 1) A short-lived rotating updraft from a non-supercell exists for a brief period of time, or 2) The automated technique detects a supercell shortly before it was detected subjectively. Either way, it seems from Fig. 3.9 that requiring that the automated algorithm to exceed the specified threshold for at least 20 min could eliminate a large proportion of false alarms. The overall improvement in skill would be greater for the UH technique, since more false alarms would be reduced and fewer hits eliminated than with the MPC technique.

Sensitivity to Horizontal Grid Spacing

To determine the relative performance of the three techniques at different horizontal resolutions, additional simulations were performed. A subset of 30 cases was randomly selected for simulation using Δx of 2 km, 500 m and 250 m. Upon performing the subjective analysis, 10 cases were discarded from the subsequent analysis—reasons for which include incorrect PC analysis window placement and non-existent convection. Only the 'optimal' configurations of the automated techniques (determined from Figs. 3.1, 3.3, and 3.5) were tested. Results from the

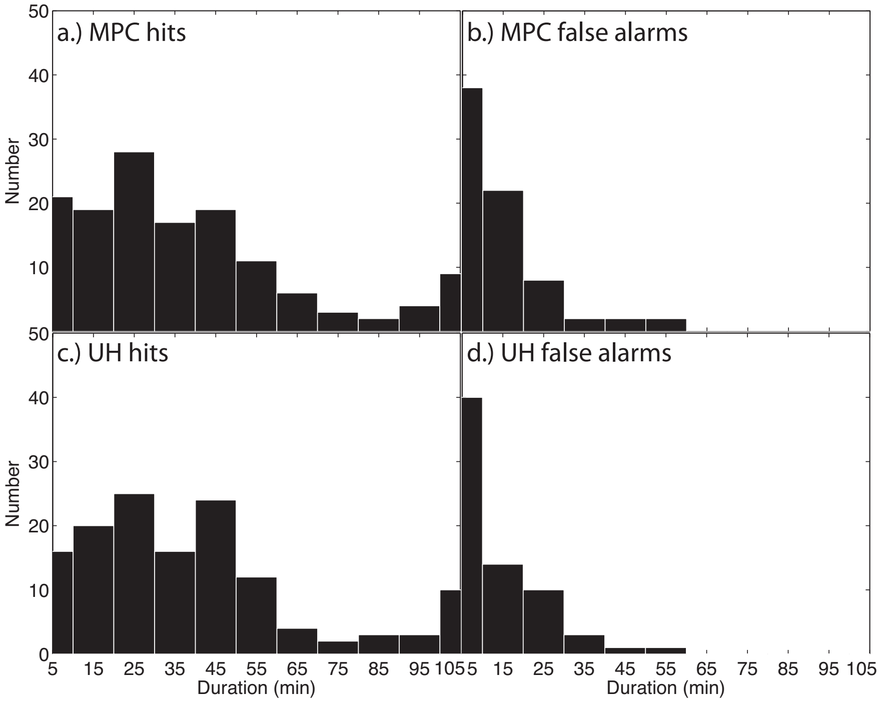

FIG. 3.9. Histograms of the duration of consecutive a.) hits from the optimal modified Pearson correlation technique, b.) false alarms from the optimal modified Pearson correlation technique c.) hits from the optimal updraft helicity technique, and d.) false alarms from the optimal updraft helicity technique.

remaining 20 cases are shown in Figure 3.10. The PC technique achieved the lowest threat score at all of the horizontal grid spacing values, but showed limited variability in both threat score and optimal detection threshold as a function of horizontal grid spacing. Both the UH and MPC techniques produced notably larger threat scores, however the performance of these two techniques as a function of grid spacing differed markedly. The largest threat score for the UH technique occurred in the Δx = 2000 m simulations, with threat scores decreasing as Δx decreased. Conversely, threat scores for the MPC technique *increased* as Δx decreased. In fact, the MPC technique produced the largest threat scores of all three techniques for Δx of 500 m and 250 m.

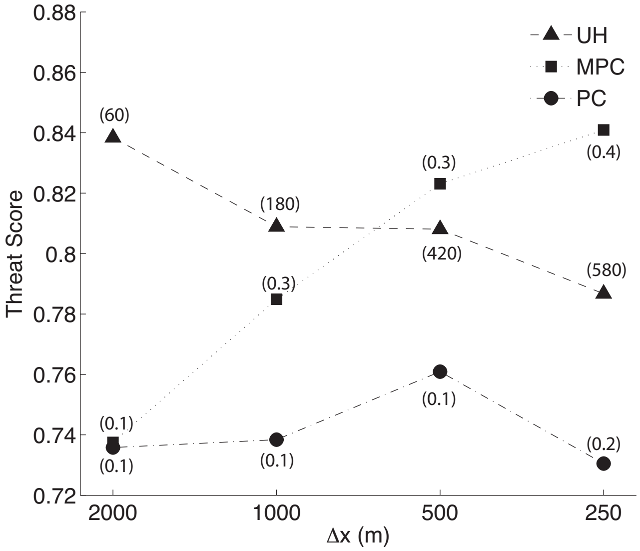

FIG. 3.10. Threat score as a function of horizontal grid spacing for the UH (dashed line with triangles), MPC (dotted line with squares), and PC (dash-dot line with circles) techniques. Numbers in parentheses represent the detection threshold that resulted in the largest threat score for a particular technique. Values of UH are in m^2 s^{-2} while PC and MPC values are dimensionless.

Tests of Statistical Significance

A one-sided matched pair t-test can be used to determine whether the threat scores are significantly different among the resolutions and techniques. However, this test requires computing a separate threat score for the analysis times of each storm simulation rather than using the "bulk" threat scores that were shown in Fig. 3.10. This results in a distribution of 113 threat scores for each technique for the 1 km simulations and 20 threat scores for each technique for each of the resolution tests. For each matched pair test, two automated techniques are selected and the difference in threat score for each of the *n* simulations is calculated. The null hypothesis for these tests is that the mean difference in threat score between two techniques is zero and statistical significance was determined based on the a=0.05 level. The results from these tests show that, for the Δx=1 km simulations, the MPC and UH techniques are both significantly better than the PC technique, however the performance of the UH technique is *not* significantly better than the MPC technique (Table 3.1). The remaining results in Table 3.1 should be interpreted with some caution, due to the much smaller sample size for these simulations compared to the Δx=1 km simulations (i.e *n*=20 vs. *n*=113, respectively). With that in mind, it is noted that the UH technique performs significantly better than the MPC and PC techniques in the Δx=2 km simulations. However, when grid spacing is reduced to 250 m, the MPC technique performs significantly better than both the PC and UH techniques.

Discussion

Although other combinations of depth and *w*-threshold settings could have been tested for the PC and MPC techniques, such tests may not be necessary. Both the PC and MPC tests revealed that the largest threat scores were achieved when using the smallest vertical averaging depth. Based on this finding, it is unlikely that larger depths (e.g. 2–10 km) will result in larger threat scores. Smaller depths would be undesirable because the presence of shallow updraft rotation could increase the number of false alarms. Tests with *w* thresholds <3 m s^{-1} and >9 m s^{-1} probably are unnecessary also, since the PC results show small spread in the threat scores at the peak correlation threshold value (i.e., 0.1) and the MPC technique appears to be more dependent on averaging depth than minimum *w* threshold.

Table 3.1. Result from one-sided matched pair *t*-tests between two specified techniques for all simulations. The two techniques being compared is shown in the top row. The top number in each cell is the *t*-statistic, with the *p* value beneath in parentheses. Values that are emboldened and italicized represent differences that are statistically significant at the 0.05 level.

	PC–MPC = 0	**MPC–UH = 0**	**PC–UH = 0**
2000 m	-1.29 (0.0956)	***-2.86*** ***(0.0014)***	***-2.51*** ***(0.0046)***
1000 m	***-6.47*** ***(6.6x10^{-13})***	-0.39 (0.3472)	***-6.54*** ***(3.9x10^{-13})***
500 m	***-1.83*** ***(0.0306)***	0.96 (0.1656)	-0.2894 (0.3861)
250 m	***-3.51*** ***(9.78x10^{-5})***	***1.66*** ***(0.0455)***	-1.31 (0.0917)

For all three automated techniques, the largest threat score was achieved using a depth of 2–5 km. Threat scores decreased as depth increased. The physical reasoning for this finding may differ between the UH and correlation techniques. The UH technique could be particularly sensitive to updraft tilt in strongly sheared environments because it is vertically integrated at a specific x, y location. When larger depths are used for UH calculations with storms having strongly tilted updrafts, the updraft may tilt out of the column at the specific x, y grid point, yielding zero values at certain levels, effectively weakening the overall value of UH. For both MPC and PC calculations, since the technique typically used is to average all correlation values over the depth, the lack of updraft rotation at a particular level (due to either absence of updraft or tilting outside of the analysis window) also would weaken the overall correlation coefficient. As a result, shallow supercells may go undetected when large depths are used. In a practical setting, this would include tropical-cyclone supercells, which tend to be relatively shallow (e.g., McCaul 1991; McCaul and Weisman 1996); such storms were excluded from the Thompson et al. (2003) dataset.

All three automated techniques produced many more false alarms than misses. It is possible that some of these false alarms are the result of subjective misclassification due to limitations in methodology of the subjective identification technique. By only considering two vertical levels in the subjective classification, it is possible that some of the subjective criteria were absent at these levels, yet present at some vertical level(s) between them. In this scenario, a storm would be subjectively classified as a non-supercell, yet detected by the automated technique as a supercell—yielding a false alarm. However, since all three automated techniques produced the largest threat score with the same vertical depth (2–5 km), and all produced approximately the same number of false alarms, it is unlikely that this effect influenced one particular automated technique more than another.

The results demonstrate that the commonly used Pearson correlation produced the lowest threat scores of the three automated techniques. However, this is not because linear correlation is a poor method for detecting supercells. If this were true, the MPC technique should have produced similarly small threat scores. Rather, the PC technique is hindered by the need to define an analysis window around the storm of interest. Additionally, it was found that the MPC technique produced the largest threat scores of the three techniques for the higher resolution simulations (i.e. Δx of 500 m and 250 m) while the UH technique produced the largest threat scores for lower resolution simulations (e.g. $\Delta x = 2$ km). These performance differences among the techniques were statistically significant and reasons for these differences are a topic for future research.

The reader may wonder about the robustness of the subjective analysis results. It is possible that the results would likely vary somewhat if a different group of researchers were to perform the subjective analysis. The contributors to this subjective supercell analysis independently agreed on 77% of the 2099 analysis snapshots obtained from the simulations having 1 km horizontal grid spacing. Most of the disagreement occurred near the end of the simulations, when many of the supercells were decaying. To examine any potential variability in the results, the threat scores shown in Fig. 3.10 were re-computed using only the subjective analysis results from one analyst. The results from this test showed that the threat scores varied by 1% or less from the values shown in Fig. 3.10—a value that is not significant.

Finally, the model results in this study are dominated by the presence of supercells. Less than 25% of the 2099 analysis snapshots contain strong convection of a mode other than supercell. Further testing is needed to better determine the false alarm rates from other forms of convection, such as squall lines, multi-cell systems and ordinary cells.

Summary

This chapter evaluated the accuracy, reliability, and skill of several automated mesocyclone detection algorithms using a dataset of 113 idealized simulations at 1-km horizontal grid spacing by comparing the automated results to the results obtained from a subjective classification of the storms produced in the simulations. The goals were to test the sensitivity of each technique to various configuration settings and determine which technique and configuration detected simulated supercells with the greatest skill. The following conclusions were reached:

- The PC, MPC and UH techniques all produced the highest threat score when the analysis was performed over a depth of 2–5 km. Threat scores decreased as vertical depth increased.
- The largest threat scores for both the PC and MPC techniques were achieved when using all points with w > 7 m s^{-1} and averaged from z=2–5 km. Compared to previous studies that have used the PC technique, the updraft threshold is larger than typically used in the past, while the averaging depth is smaller. Additionally, the PC performed worse than the other two techniques, having the fewest number of hits and largest number of misses.
- The UH technique with integration from 2–5 km and using a detection threshold of 180 m^2 s^{-2} produced the largest threat score of the three techniques for the Δx=1 km simulations. However, differences between the UH and MPC techniques were not statistically significant. For the subset of analyzed cases with Δx=250 m (averaged from 2-5 km and using a *w* threshold of 7 m s^{-1}), the MPC technique produced the largest threat scores, which were found to be significantly larger than the UH technique.
- False alarms tended to have a much shorter duration than positive detections for the MPC and UH techniques (the only two tested). The majority of the

false alarms lasted less than 20 min, while the majority of the positive detections lasted more than 20 min. Based on this finding, adding a requirement that the automated detection threshold must be exceeded for >20 min should substantially reduce false alarms without drastically decreasing positive detections.

Therefore, it is concluded that for simulations with Δx=1 km, either the UH or MPC techniques could be used with nearly equal skill in automated detection of non-tropical supercells in both large idealized parameter studies and in convective resolving forecast models. Additionally, the UH technique has the most skill in automatically detecting supercells in simulations with Δx =2 km, while the MPC technique has the most skill for simulations with Δx = 500 m or 250 m.

CHAPTER 4

CONVECTIVE INITIATION TESTS

Introduction

Because the initial environment in most idealized supercell simulations is devoid of horizontal gradients, convective development must be initiated artificially. By far the most common method is the thermal perturbation (or warm bubble) technique (Klemp and Wilhelmson 1978). With this method, a spheroid of positive potential temperature perturbation is inserted in the center of the domain at the initial time. In the appropriate environment, the positively buoyant air in this spheroid will rise—creating convergence and additional vertical motion in its wake. Over time, a strong convective updraft develops. Although the warm bubble technique is widely used, it is not without drawbacks.

The vast majority of environments observed near mature supercells have some amount of convective inhibition (CIN; e.g. Thompson et al. 2003, Davies 2004). However, in several idealized simulation studies, investigators have reported difficulty in using the warm bubble method to initiate convection in environments containing capping inversions [e.g. Chen and Orville (1980), Wicker et al. (1997), Elmore et al. (2002), Letkewicz and Parker (2011)] or lacking deep moisture (e.g. McCaul and Cohen 2004). Perhaps it is not surprising that the two most commonly used soundings for idealized supercells initiated using the bubble technique have capping inversions that have either been removed, were not resolved by the vertical model grid spacing, or were absent by design. These are the 20 May 1977 Del City sounding [e.g. Klemp et al. (1981), Grasso and Cotton (1995), Gilmore and Wicker (1998), Adlerman et al. (1999), Adlerman and Droegemeier (2005)] and the Weisman and Klemp analytical sounding [e.g Weisman and Klemp (1982,84), Brooks and Wilhelmson (1993), Brooks et al. (1994), Wicker and Wilhelmson (1995), Richardson et al. (2007)].

Ziegler et al. (1997) state that these two soundings are similar to the narrow convective initiation regions observed along dry lines but are not representative of the mature storm environment. For instance, in the well-studied 22 May 1981 Binger, OK supercell, the storm survived and was not tornadic until it moved into an area with larger values of convective inhibition (Ziegler et al 2010). Muñoz (1994) emulated such environmental changes within an idealized cloud model by initializing the warm bubble in the uncapped sounding and progressively nudging a capping inversion into the model for a maturing supercell storm. Sustained convection would not initiate using only the capped environment.

An alternative to using an initial warm bubble to initiate convection is to apply a convergent wind field. Tripoli and Cotton (1980) and Loftus et al. (2008) used a sustained initiation technique to study convective development by nudging the model winds with a near-surface convergence field, but this was tested using environments *without* capping inversions. The horizontal convergence produces a positive pressure anomaly, which drives an upward-directed perturbation pressure force and resulting updraft to help parcels reach their level of free convection (LFC). Alternatively, one may nudge an updraft within the boundary layer (e.g., Ziegler et al 2010). This is similar to the convergent wind technique, except the horizontal wind field responds to the updraft instead of vice versa. However, there is some question as to the time period and altitudes over which low-level updraft nudging should be applied to overcome a typical capping inversion. If too low, the air may slow or even stop moving vertically, causing the air to diverge horizontally beneath the capping inversion. If too high, and the updraft may not be able to draw in air from below the capping inversion.

This chapter has three main purposes: (1) to demonstrate that a sustained updraft nudging initiation technique is substantially more effective than the instantaneous warm bubble technique at producing supercells in horizontally-homogeneous environments with capping inversions, (2) determine which updraft nudging settings produce the strongest, longest-lived supercells, and (3) demonstrate that a sustained forcing technique is most effective when elevated off of the surface.

Methodology

Model Setup

The model setup follows that of the simulations in Chapter 3, which includes a single moment, bulk ice microphysics parameterization (Gilmore et al. 2004) with default parameters; a model grid that moves with the 0-6 km mean wind; and a simulation run time of 2 h. Each idealized simulation used a horizontally homogeneous environment and was initialized with one of the 113 Rapid Update Cycle-2 (RUC-2) supercell proximity soundings used in Chapter 3.

Convective Initiation

Supercell simulations were initiated using two methods. The first was the traditional warm bubble method (hereafter, BUB), which is defined by a spheroid having a 10 km horizontal radius and a 1.5 km vertical radius centered at z=1.5 km with a 4 K max potential perturbation. Brooks (1992) and McCaul and Cohen (2004) have shown that a 4 K perturbation can produce sustained convection in a wider ranger of environments (i.e. smaller CAPE and moisture content) than a 2 K perturbation.

The second initiation method utilized updraft nudging (UN). A spheroid having the same dimensions and location as the warm bubble is used, with the difference being that the updraft at a particular time and grid point (w_t) is determined by

$$w_{mag} = \begin{cases} w_{max} cos^2\left(\frac{\pi}{2}\beta\right), & \text{if } 0 \le \beta \le 1 \\ 0, & \text{if } \beta > 1 \end{cases} \tag{4.1}$$

$$w_t = w_{t-1} + dts \times \alpha \times \max\left(w_{mag} - w_{t-1}, 0\right), \tag{4.2}$$

where β is the distance from the center of the spheroid normalized by its radius, α is the acceleration constant, *dts* is the small model time step (0.375 s in these simulations), and the max function insures that nudging is not applied once the vertical velocity exceeds w_{max}. Here, $\alpha = 0.5\ \mathrm{s}^{-1}$ and w_{max}=10 m s^{-1}. Nudging starts at t=0 and lasts a specified duration. The durations tested herein varied from 5 min to 45 min at 5 min increments, resulting in a total of 9 UN tests for each sounding environment.

Supercell Detection

Supercell presence is determined based on threshold values of 2-5 km updraft helicity (UH > 180 $\mathrm{m}^2\ \mathrm{s}^2$ for 20 min; following Chapter 3). This method is used to determine both supercell duration and supercell intensity (time-average of domain maximum updraft helicity) based on model output available every 60 seconds during the simulation. The results in Chapter 3 show that the UH technique has a small (roughly 5%) false alarm rate from successive non-supercell mesocyclones that jointly exceed the 20 min temporal criteria.

Results and Discussion

Simulations With the Warm Bubble Technique

Of the 113 simulations completed with BUB, only 35 (31%) had supercells detected at least once during the simulation (SUP). The average supercell duration in these cases was 4265 s. Of the 35 SUP cases, 18 (51%) produced supercells that lasted at least 1 h. Of the 78 simulations without any supercell detection, 29 (37%) produced a non-supercell updraft exceeding 10 m s^{-1} (NON) while 49 (63%) failed to produce any vertical motion greater than 10 m s^{-1} (NULL).

The relationship between CAPE, CIN, and whether BUB was able to produce a supercell is striking but perhaps not surprising. For the SUP cases, mixed layer CAPE[4] is larger (on average; Fig 4.1a), mixed layer |CIN| is significantly smaller (median of 18 J kg^{-1}; Fig 4.1b), and the ratio between CAPE/|CIN| (Fig 4.1c) is larger (75 or greater) than in the NON + NULL cases. In fact, Fig. 4.1c shows almost no overlap in the upper quartile of CAPE to |CIN| ratio between the SUP and NON+NULL categories. In other words, although all proximity soundings were associated with supercells in nature, the capping inversion was usually too strong for BUB to initiate sustained convection in the model. Furthermore, midlevel relative humidity, averaged from 2 – 5 km ($\overline{RH}_{25}$; Fig 4.1d) is larger in the SUP cases and smaller in the NON-NULL cases —consistent with the results of McCaul and Cohen (2004) who found that storm lifetime was short in environments with small environmental relative humidity. These results demonstrate the limited supercell environments in which BUB is effective.

---

[4] Thermodynamic indices were calculated using a 500 m mixed layer parcel and the virtual temperature method discussed by Doswell and Markowski (2004).

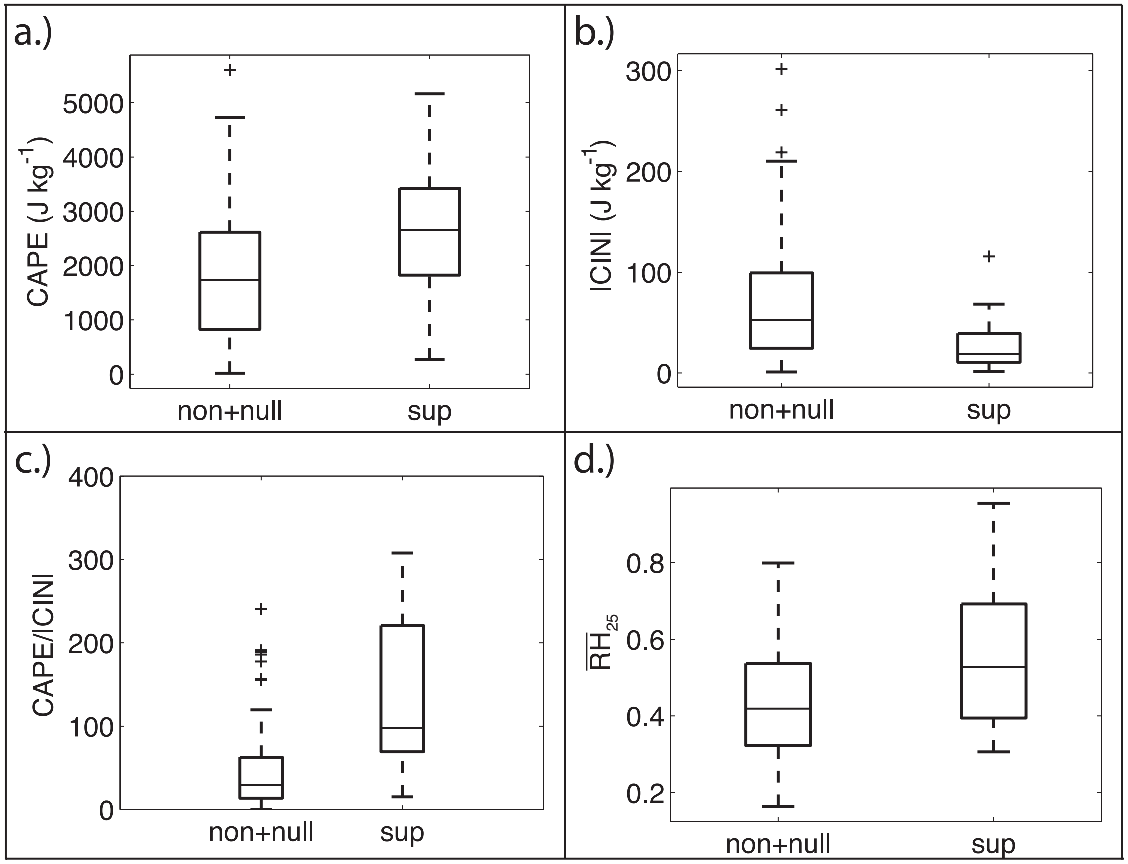

FIG 4.1. Box and whisker plots of a.) mixed layer CAPE, b.) magnitude of mixed layer CIN, c.) CAPE/CIN ratio, and d.) 2-5 km average relative humidity for the supercell producing (SUP) and non-supercell plus NULL producing simulations (NON+NULL) using warm bubble convective initiation. CAPE and CIN are calculated using a 500 m thick parcel to represent the surface and virtual temperature. The whiskers represent 2.5 times the standard deviation from the mean.

Updraft Nudging (UN) Simulations

All UN configurations result in about three times as many SUP simulations than BUB (Table 4.1) and, unlike BUB, none are NULL. Although average supercell duration[5] is largest for the 10 min UN configuration (Fig. 4.2), the 15 min UN configuration (hereafter, UN15) is able to produce supercells in more environments (Table 4.1) and those supercells are strongest, on average, with a substantial drop-off in supercell strength when UN is applied for longer or shorter periods (Fig. 4.2). In

---

[5] Supercell duration is likely underestimated since approximately 35% of supercell producing simulations still contained a supercell when the simulations ended at t=2 h.

addition, Table 4.1 shows that the UN15 configuration also produced the most supercells both lasting longer than 60 min and lasting longer than 75 min[6].

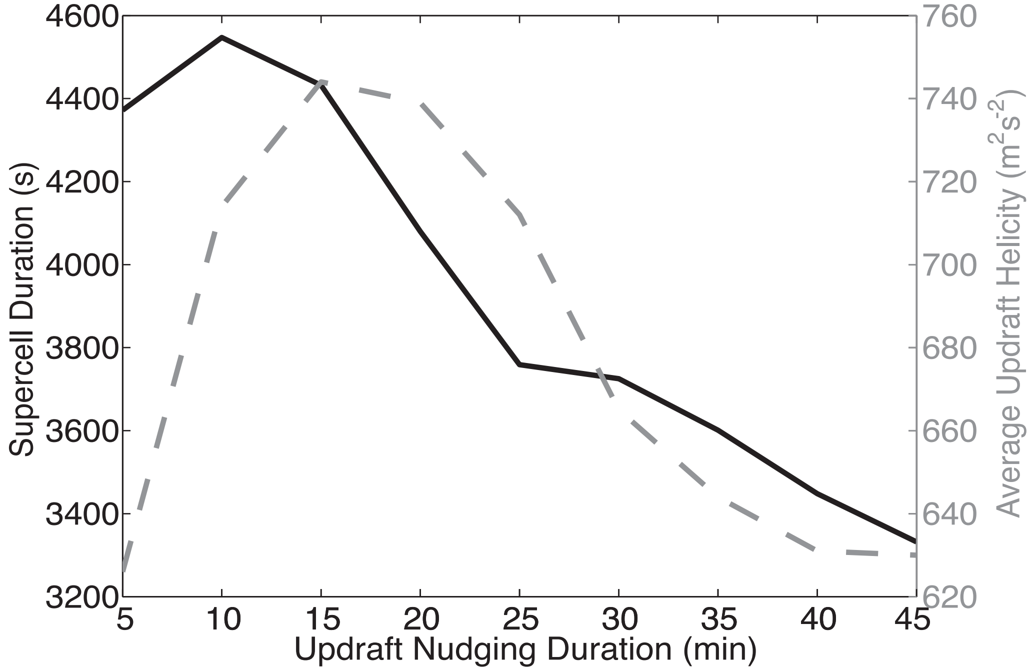

FIG 4.2. Average supercell duration (black line) and average updraft helicity (gray dashed line) for all 113 cases as a function of updraft nudging duration. The average supercell duration for the bubble technique is 4625 s and average updraft helicity is 472 m^2 s^{-2} (not plotted).

To illustrate one reason why supercells are stronger and longer-lived for UN15, a few sounding cases with substantially longer-lived supercells for UN15 compared to UN45 were examined in more detail (not shown). The longer UN duration produces supercells with greater precipitation mixing ratio aloft and faster propagating gust fronts that surge ahead of the midlevel updraft once the heavier precipitation reaches the surface: a well known mechanism for supercell demise (McPherson and Droegemeier 1991). Because the microphysics is “switched on” the entire UN time, it is logical that longer UN times would produce more precipitation, and future work should explore this sensitivity, including tests where precipitation is delayed during the UN period.

---

[6] Supercell duration is calculated only after UN is turned off. Thus, 75 min is the longest possible duration for the UN45 simulations.

Conversely, if the UN duration is too short, the nudging ends before a cold pool is established. Thus, when nudging is turned off, the low-level updraft could weaken because it is not aided by convergence along the gust front.

Table 4.1 Number of supercell producing simulations and number of simulations that produce a supercell that exceeds specified durations for the various UN configurations. Numbers in parentheses represent the amount of time from the point UN is disabled until the end of the simulation (t=2 h). The bold entries indicate the maximum for each column. The number in parentheses in the last column represents the total possible duration remaining after UN is shut off for each 120 min simulation. None of the UN configurations produced NULL cases.

	Total # of supercells	**Supercell > 60 min**	**Supercell > 75 min**	**Supercell duration of simulation**
UN5min	91	52	43	0 (115 min)
UN10min	99	***61***	52	33 (110 min)
UN15min	***102***	***61***	***53***	33 (105 min)
UN20min	***102***	56	49	35 (100 min)
UN25min	98	48	42	31 (95 min)
UN30min	98	51	44	36 (90 min)
UN35min	97	50	43	37 (85 min)
UN40min	97	48	42	***40*** (80 min)
UN45min	94	47	39	39 (75 min)

These mechanisms of supercell demise are illustrated for one case in a capped environment (Fig 4.3a). Fig. 4.3b shows that a long nudging duration (UN45) produces a supercell that weakens earlier than those in simulations using a shorter UN duration while nudging that is too brief produces only a short-lived supercell (UN5 in Fig 4.3b). In contrast, the UN15-UN35 configurations all produce a long-lived, quasi-steady supercell (Fig. 4.3b). Note that the bubble technique failed to produce a supercell in this case (BUB in Fig 4.3b).

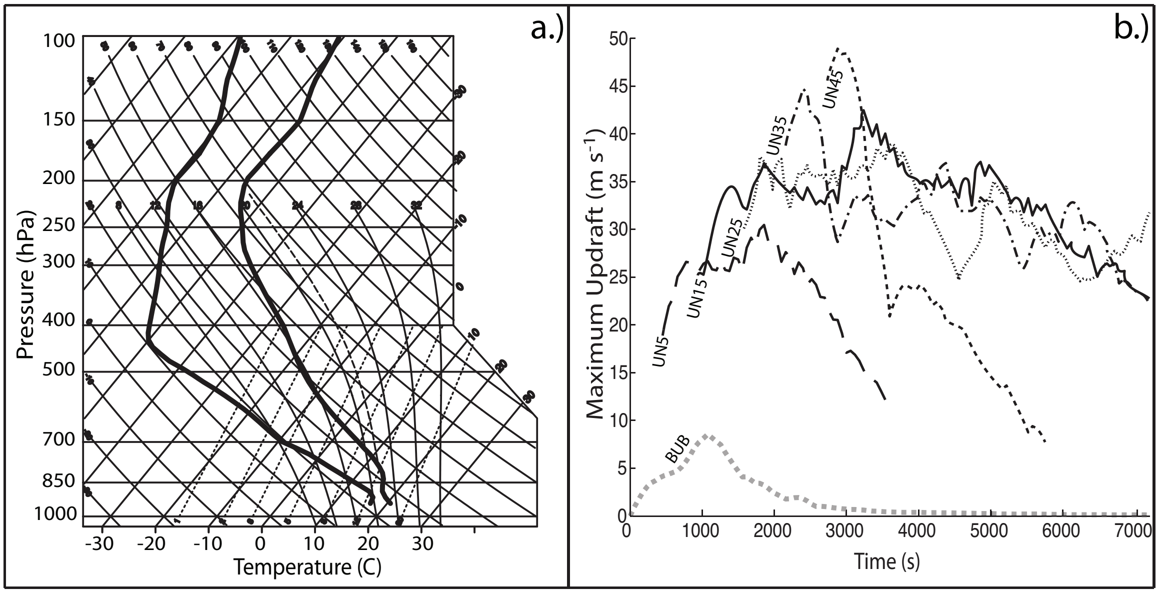

FIG. 4.3. Time series of domain maximum updraft for a specific RUC-2 sounding (panel a) using the bubble (BUB) convective initiation method and various durations of updraft nudging (panel b). Maximum updraft speed is plotted at all times for BUB and only at times when a supercell was present for UN cases. The bubble method did not produce a supercell at any time in the simulation.

For the UN15 technique, |CIN| is a poor discriminator (Fig. 4.4b) between the SUP and NON cases. CAPE to |CIN| ratio values in the UN15 SUP cases are about half those of the BUB SUP cases (Fig 4.4c). In addition, the UN15 results show a small difference in $\overline{RH}_{25}$ between the NON+NULL and SUP cases (Fig. 4.4d). Thus, in contrast to the BUB results, the effectiveness of the UN method is not strongly affected by the amount of CIN and $\overline{RH}_{25}$ in the initial environment.

Sensitivity to UN Spheroid Placement

To demonstrate the importance of spheroid placement, the UN15 simulations were repeated with the same settings as before, except with a spheroid having a vertical radius of 500 m centered at *z*=500 m (hereby referred to as the UNsfc simulations). These simulations are meant to emulate a ‘surface-based’ forcing technique similar to that of Loftus et al. (2008). Tests have shown that the near surface convergence response

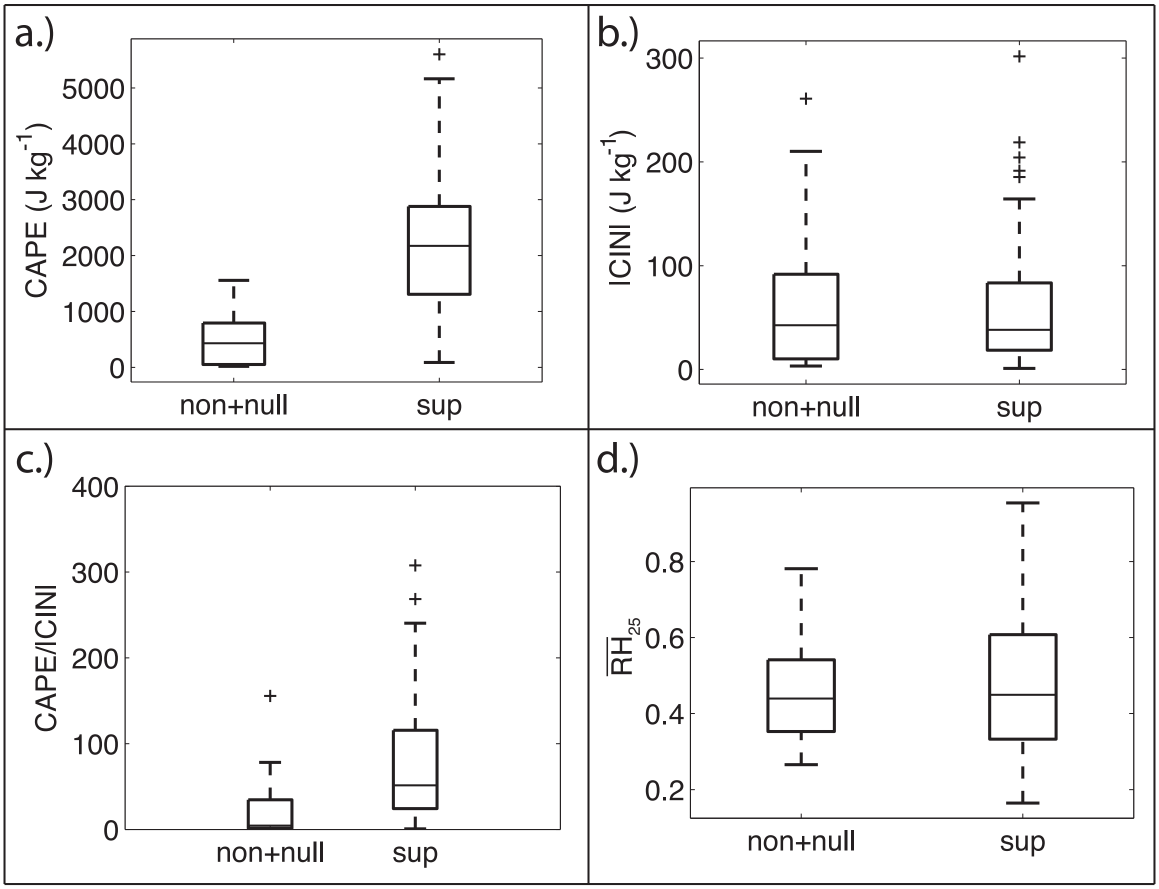

FIG 4.4. Box and whisker plots of a.) mixed layer CAPE, b.) magnitude of mixed layer CIN, c.) CAPE/CIN ratio, and d.) 2-5 km average relative humidity for the supercell producing (SUP) and non-supercell plus NULL producing simulations (NON+NULL) using UN15 convective initiation. CAPE and CIN are calculated using a 500 m thick parcel to represent the surface and virtual temperature. The whiskers represent 2.5 times the standard deviation from the mean. Note that NULL=0 for all UN configurations so NON+NULL is really equal to the number of NON.

to the UNsfc settings is approximately 6-8 times stronger than the maximum surface convergence specified by Loftus et al. (2008). Compared to the original UN15 simulations with the spheroid centered at 1.5 km AGL, the UNsfc simulations produced fewer SUP cases (28 vs. 102), fewer supercells lasting longer than 1 h (14 vs. 61), and smaller average updraft helicity (524 $m^2 s^{-2}$ vs. 744 $m^2 s^{-2}$). Further analysis of the UNsfc simulations revealed that the SUP cases were only possible for smaller environmental |CIN| (Fig. 4.5) as compared to the original UN15 runs. Thus, UNsfc is less able to overcome larger |CIN| compared to when UN is placed at 1.5 km AGL—suggesting that the UN method is more effective when the spheroid extends higher than the area of convective inhibition and above (or close to) the LFC—similar to the warm bubble results of Brooks (1992).

Additional UN Simulations

Additional simulations were performed to test sensitivity to the updraft nudging parameters α and w_{max}. When UN simulations were repeated with α=0.1 s^{-1}, 15 min is again the optimal UN duration. However, there were fewer SUP cases (88 vs. 102), fewer SUP exceeding 1h (47 vs 61), and the average UH was less (628 m^2 s^{-2} vs. 744 m^2 s^{-2}) than the UN15 simulations (not shown). Several simulations were performed by decreasing w_{max} from 10 m s^{-1} to 5 m s^{-1}, but doing so consistently decreased supercell duration and intensity no matter what environmental sounding was used (not shown).

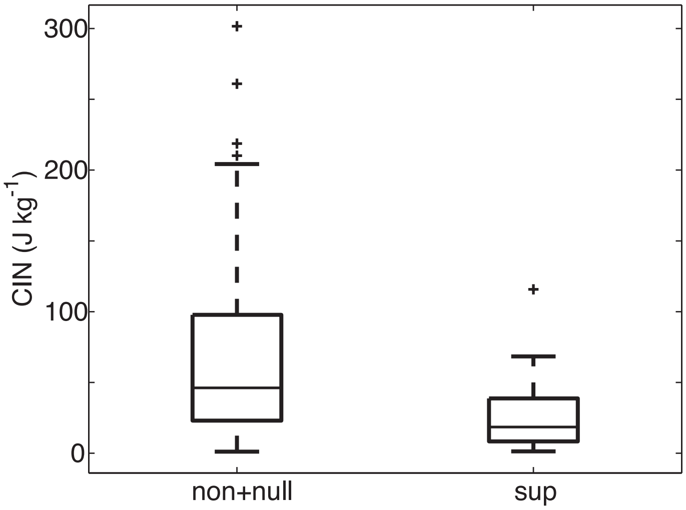

FIG 4.5. Magnitude of mixed layer CIN for simulations using an updraft nudging spheroid with a vertical radius of 500 m and centered at *z*=500 m.

Additional Factors Influencing Updraft Nudging Effectiveness

Simulations using a sustained convective initiation technique have additional sensitivities compared to those initiated by a warm bubble. Two of these sensitivities are discussed below, along with a handful of examples. These sensitivities were not tested with the full suite of simulations discussed in this chapter. The purpose of this section is simply to demonstrate that such sensitivities exist.

Sensitivity to Grid Motion

With the warm bubble convective initiation technique, model grid motion has almost no effect on storm evolution. The small changes that are observed are most likely caused by differences in gravity wave reflection at the lateral boundaries. However, when a sustained initiation technique like UN is used, grid motion can produce large differences in storm structure. This is because the nudging location is fixed to the center of the domain. As an extreme example, consider two simulations performed with the same initial environment—one performed with a non-moving grid and one with a grid motion determined from the 0-6 km mean wind. In the non-moving grid simulation, the UN spheroid is fixed to the center of the domain, however once the updraft exits the spheroid, it is advected downstream. If instead, a grid motion is selected that matches the storm motion, then the nudging region is essentially following the updraft, creating a nearly vertical updraft.

Sensitivity to grid motion was tested by randomly selecting five of the RUC-2 soundings for simulation. The UN was applied for the first 45 min of simulation with α =0.5 s^{-1}, w_{max}=10 m s^{-1}. For the moving grid simulations, box motion was based on storm motion, which was calculated using the 0-6 km mean environmental wind in the initial sounding. Two of the five soundings selected for testing did not produce organized convection regardless of grid motion, and will not be mentioned hereafter. The results from the remaining three soundings show that two cases (Cases B & C) produced sustained updrafts only when a non-moving grid was used (Figs. 4.6c and 4.6e), while the other case (Case A) produced a sustained updraft with both a moving and non-moving grid (Fig 4.6a). The updrafts in the non-moving simulations developed much slower than in the moving grid simulations for all three cases. Figs. 4.6b, 4.6d, and 4.6f show that strong downdrafts rapidly developed immediately after updraft nudging is turned off. In Case A, initial downdraft magnitude between the moving and non-moving simulations is quite similar. However, in Cases B and C, downdrafts in the moving simulations are initially much stronger, while the downdrafts in the non-moving simulations develop more gradually. This suggests, at least for these two cases, that the outflow is too strong to balance the near surface inflow winds and the storm gusts out.

To test this hypothesis, Case B was analyzed in more detail. Figure 4.7 shows that the low-level outflow of the storm in the moving grid simulation has much smaller pseudo-equivalent potential temperature (θ_{ep}) than the outflow in the non-moving simulation. Consequently, the outflow in the moving simulations propagates outward at a much more rapid rate, eventually cutting off the low level updraft from inflow air. In the non-moving simulation, the outflow is weaker and the low level updraft is not disrupted.

To further investigate the reason why grid motion has such a strong effect on storm longevity, cross-sections were taken through the updraft for the Case B simulations (not shown). The results show that, in the moving simulations, by the time the updraft nudging is turned off at t=2700s, a strong, singular updraft extends well past

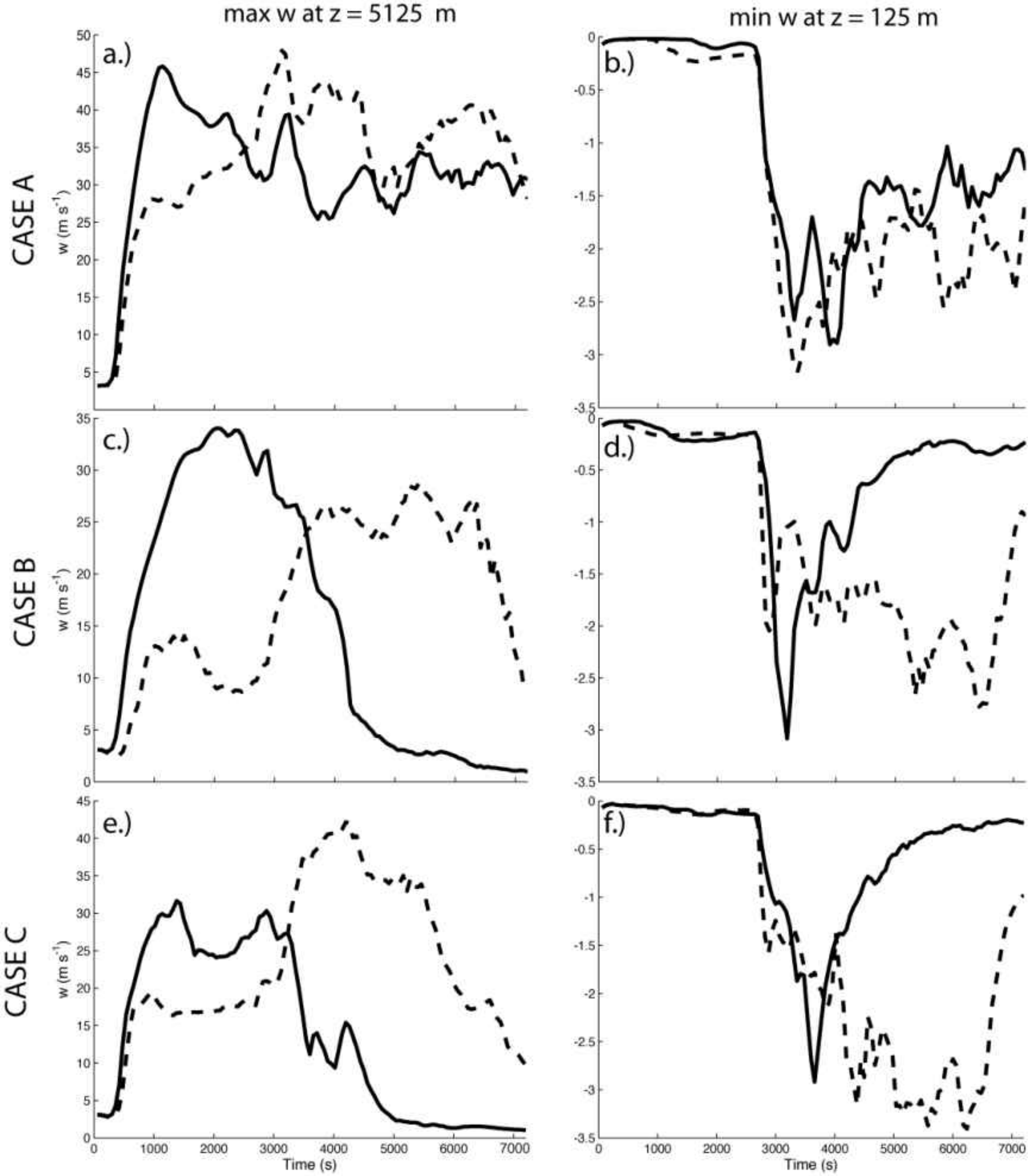

Fig. 4.6: Time series plots of domain maximum *w* (m s^{-1}) at 5125 m (first column) and domain minimum *w* (m s^{-1}) at 125 m (second column) for three different test cases. Each case was simulated using a 0-6 km mean wind moving grid (solid line) and non-moving grid (dashed line).

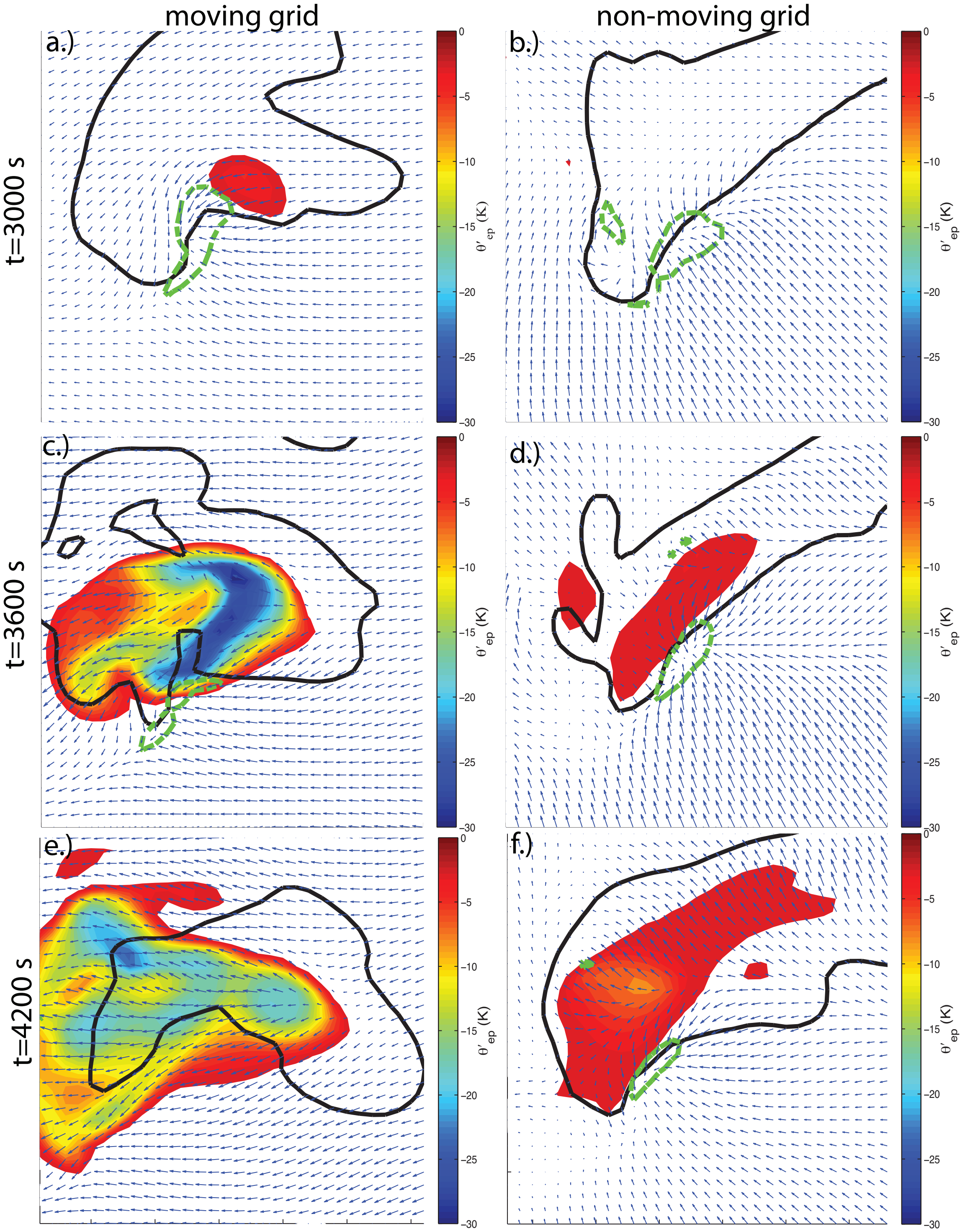

Fig. 4.7: Time evolution of storm structure at *z*=125 m for Case B using a moving grid (left column) and non-moving grid (right column). The solid black contour is the 30 dBZ simulated radar reflectivity contour, green dashed line is the 1 m s^{-1} vertical velocity contour, blue wind barbs show horizontal winds, and the filled colored contours represent deficits (relative to initial values) of pseudo-equivalent potential temperature (θ'_{ep}).

z=10 km. However, in the non-moving simulations, there is a strong disconnect between the 0-3 km updraft and the upper level updraft. Since the UN spheroid is 'locked' to the center of the grid, the low-level updraft remains at thecenter of the domain. Above this altitude, the updraft is advected downstream by the environmental winds. After UN is turned off at t=2700 s, the low-level updraft is allowed to propagate downstream and begins to grow in vertical extent. This explains the increase in midlevel updraft with time shown in Fig. 4.6.

Downdraft Production

Equations (4.1) and (4.2) show that the UN technique does not permit downdrafts anywhere in the domain during the nudging period. This is certainly unrealistic, especially when the nudging is applied for an extended period of time. The nudging subroutine was modified to allow the presence of downdrafts outside of the nudging spheroid. The three simulations discussed in the previous section were repeated with this modified UN subroutine to test sensitivity to the presence of downdrafts during the UN period. The results show that when downdrafts are enabled, maximum updraft intensity diminishes more rapidly in both the moving and non-moving grid simulations (Fig. 4.8).

Summary and Conclusions

RUC-2 supercell proximity soundings were used within an idealized cloud model having 1 km horizontal grid spacing to test the sensitivity of supercell intensity/longevity to two different convective initiation methods: the traditional warm bubble technique (BUB) and a sustained updraft nudging technique (UN). The UN initiation technique, applied for the first 15 min of simulation over the lowest 3 km,

1. was more effective at producing supercells (102 cases; 61 lasting longer than 1 h) than BUB (35 cases; 19 lasting longer than 1 h);
2. was able to produce supercells in environments having larger median |CIN| than BUB (38 J kg^{-1} vs. 18 J kg^{-1});
3. usually produced stronger and longer-lived supercells compared to when longer UN forcing was used; and,
4. was more effective at producing supercells than when the UN spheroid was moved from the lowest 3 km to the lowest 1 km.

Thus, the UN convective initiation technique—with settings that maximize supercell longevity and intensity—will be used for all remaining simulations in subsequent chapters. Although this current study only investigated supercells, these tests could be expanded to study the initiation sensitivity of other modes of convection. Future work could also focus on the sensitivity of the UN method to grid spacing, grid motion, spheroid size, and precipitation development during the UN period.

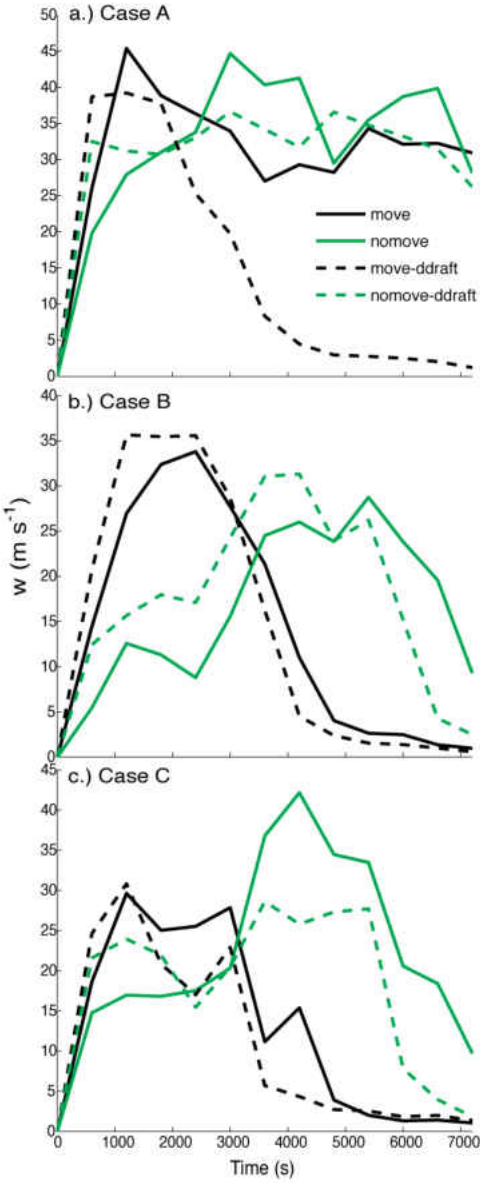

FIG. 4.8. Time series of domain maximum updraft for three cases. Four simulations were performed for each case: simulations with a moving grid and downdrafts disabled (enabled) during the UN period are shown with a solid (dashed) black line, and simulations with a non-moving grid and downdrafts disabled (enabled) are shown with the solid (dashed) green line.

CHAPTER 5

ENVIRONMENTAL FACTORS INFLUENTIAL TO THE DURATION AND INTENSITY OF TORNADOES IN SIMULATED SUPERCELLS

In Chapter 3, various methods were tested to determine the best approach for automating supercell detection in cloud-resolving simulations. In Chapter 4, the convective initiation technique that produces the longest, strongest lived supercells was identified. The remaining chapters will apply these results to perform simulations of the RUC-2 soundings at tornado-allowing resolution. This chapter focuses on examining which sounding parameters are most influential to the duration and intensity of simulated tornadoes.

Introduction

The environments supportive of tornadoes and their parent supercell thunderstorms have been studied extensively over the last sixty years using so-called "proximity soundings"— thermodynamic and wind profiles of the atmosphere that are in close time/space proximity to tornadic storms [e.g. Fawbush and Miller (1952,54); Beebe (1955,58); Darkow (1969); Maddox (1976); Davies and Johns (1993); Brooks et al. (1994); Rasmussen and Blanchard (1998); Thompson et al. (2003*);* Togstad et al. (2011)]. For the latter three studies, statistically significant differences were found between environmental sounding parameters associated with significantly tornadic [i.e. a damage rating of F2 or greater on the F-scale (Fujita 1981) and non-tornadic environments]. While the sounding parameters from these studies are useful tools for forecasting the occurrence of tornadoes, they have not been tested to predict tornado intensity and *duration*. A better understanding of the factors influential to tornado strength and duration is important to improving forecasts of violent, long-lived tornadoes (Simmons and Sutter 2012).

Previous studies that have investigated the relationship between tornado intensity and environmental parameters have used tornado damage ratings (i.e. F-scale) as a proxy for tornado intensity [e.g. Colquhoun and Shepherd (1988); Colquhoun and Riley (1996); Kerr and Darkow (1996), Thompson et al. (2012)]. However, damage ratings may underestimate true tornado intensity (as indicated by maximum wind speed or central pressure drop) if the tornado does not encounter any structures to damage. In addition, Marshall (2002) showed that tornado damage is heavily influenced by the quality of building construction, and that the wind speeds needed to cause the damage observed from the 3 May 1999 Moore, OK tornado were much less than that established by the F-scale. Although the F-scale has recently been replaced by the Enhanced Fujita (EF) scale, there are likely still issues related to damage rating consistency (Doswell et al. 2009). Another potential problem with these studies is that they relied on sounding data obtained with infrequent weather balloon launches which may not be representative of the tornado environment. This issue was remedied by Thompson et al. (2003) and later studies that used sounding output from a data assimilation system [RUC; Benjamin et al. (2004)] that frequently updates the 3-D state of the atmosphere to better pinpoint the tornado environment in both time and space.

The purpose of this chapter is to take a first step toward examining the environmental parameters associated with long-lived and intense simulated tornado-like vortices (herein referred to as simulated tornadoes). This study is the first ever (modeling or observational) to demonstrate a relationship between environmental parameters and tornado duration. The simulation framework provides a way to more easily capture the entire lifecycle of intense tornadoes, even if they are especially long-lived. This chapter also demonstrates a new algorithm for automated tornado detection in cloud models—believed to be the first of its kind. This work is part of a larger effort toward understanding how and why the environmental parameters affect tornado intensity and/or longevity.

Methodology

The model setup was identical to that of previous chapters except for the following: 100 m grid spacing (vertical and horizontal) within a 120-km × 120-km × 20-km domain; a large time step of 1 s for advection and a small time step of 0.167 s. According to the Courant-Friedrichs-Levy model stability criteria for advection, a model time step of 1 s in combination with 100 m grid spacing will maintain numerical stability as long as simulated wind speeds are less than 100 m s^{-1}. Since the strongest tornado in the Enhanced Fujita scale would be approximately 103 m s^{-1}, it is unlikely that winds associated with simulated tornadoes will produce numerical instability.

Convection was initiated using the optimal updraft nudging configuration determined in Chapter 4 (applied for the first 900 s of cloud time over a 10-km × 10-km × 3-km spheroid centered at z = 1.5 km with α =0.5 s^{-1} and w_{max}=10 m s^{-1}). Each idealized simulation was initialized with one of the 113 RUC-2 proximity soundings associated with significantly tornadic (EF2 or greater) supercells from Thompson et al. (2003). That study verified tornado and parent supercell existence, but omitted detailed observations of individual storms (including low-level outflow characteristics) that might otherwise be compared to the simulations. Thus, instead of a detailed storm comparison, the focus here is to statistically determine which environmental variables explain most of the variance in simulated tornado behavior.

Definition of a Simulated Tornado

Several studies have found that a Rankine vortex (Rankine 1882) is a good approximation to tornado wind fields observed with radars [e.g. Lee and Wurman (2005); Kosiba and Wurman (2010)]. This model consists of two regions, separated by a critical radius (r_c). Within the inner core of the vortex ($r < r_c$), tangential velocity (v) is directly proportional to the distance from the center of the vortex (solid body rotation) and vertical vorticity is constant. Outside of the inner core ($r > r_c$), tangential velocity is inversely proportional to r and vertical vorticity is zero. Additionally, it is assumed that there are no vertical or radial motions in the vortex. Following Houze (1993), flow within the vortex can be represented by the cyclostrophic relation

$$\frac{v^2}{r} = \frac{1}{\rho_0}\frac{\partial p}{\partial r}. \tag{5.1}$$

Integrating (5.1) from 0 to r_c yields the relationship

$$p(r_c) - p_0 = \frac{\rho_0 v^2}{2}, \tag{5.2}$$

where p_0 is the pressure at the center of the vortex and $p(r_c)$ is the pressure at r_c. Assuming the density of air (ρ) is 1 kg m^{-3}, a simulated tornado is said to be present in a simulation if the horizontal pressure difference (measured from a particular grid point to its relative r_c) is less than -450 Pa, with the wind speed at r_c being at least 30 m s^{-1}.

The maximum tangential wind speed for a Rankine vortex is related to the circulation (Γ) by

$$V_{\max} = \frac{\Gamma}{2\pi r_c}. \tag{5.3}$$

Since circulation is also defined as vorticity multiplied by area, the vertical vorticity associated with a Rankine vortex can be determined. However, assumptions about the size of the vortex must be made for this calculation. As a low-end estimate to the minimum vorticity that should be associated with a Rankine vortex, consider an EF0 tornado with maximum winds of 30 m s^{-1} (~65 mph) and r_c of 500 m. This vortex would have a vertical vorticity of approximately 0.1 s^{-1}. Thus, a third criterion for tornado detection is that the pressure drop be associated with vertical vorticity of at least 0.1 s^{-1}.

All values are computed at the lowest scalar level (z=50 m). In this study, r_c is defined by the grid point with the maximum horizontal wind speed located within a 600 m radius of r_0. A schematic of the detection procedure is shown in Figure 5.1. The wind speed and pressure drop thresholds correspond to an EF0 tornado and the vorticity threshold is used to ensure that the pressure drop is associated with rotation.

Results

The simulations from Chapter 4—which used 1 km horizontal grid spacing—were used to predict which significantly tornadic RUC-2 soundings would produce long-lived supercells when simulated with 100 m grid spacing. Cases that did not produce long-lived supercells in the 1 km simulations were deemed unlikely to do so with 100 m grid

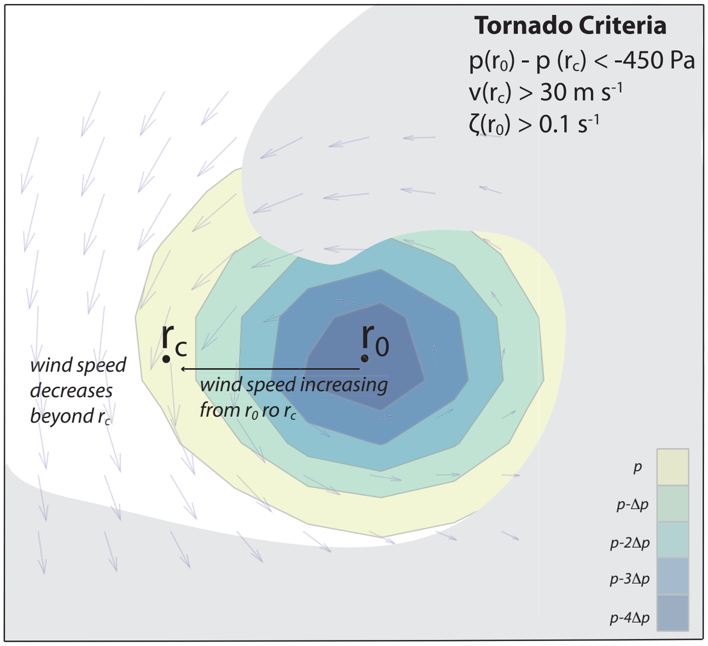

Figure 5.1. Conceptual schematic of simulated tornado detection. The filled gray region represents the radar reflectivity of a supercell hook echo. Wind vectors are shown in light gray, with the size of the vector being proportional to wind speed (v). Colored contours represent pressure (p) at the lowest scalar level in the model (z=50 m).

spacing. In the 1 km resolution simulations, sixty cases produced supercells lasting at least 1 hr in duration. These sixty cases were chosen for simulation at 100 m resolution. Thirty-one of these simulations produced supercells—determined using a combined subjective and objective approach. Subjective criteria included the presence of common supercell characteristics detectable in the simulated radar reflectivity field (e.g. a hook echo, weak-echo region, and rightward propagation). The objective portion was determined using an updraft helicity (integrated from 2-5 km) threshold value of 900 m^2 s^{-2} (based on results from Chapter 3). A supercell was said to be present if both the objective and subjective criteria were met for at least 20 minutes. Of the 31 supercell simulations, 21 produced simulated tornadoes. These 21 simulations are the focus of the forthcoming analysis.

Simulated Tornado Duration

Total simulated tornado duration was determined by summing the number of times that at least one simulated tornado is detected during the two-hour simulation from model output available every 30 s. Longer durations may be associated with a single simulated tornado or a series of simulated tornadoes (Figure 5.2). Note that tornado demise was not coincident with storm demise. (Supercells that produced short-lived simulated tornadoes maintained their updraft strength and structure for at least 30 min after the final tornado detection.) The left column of Figure 5.3 shows scatterplots of simulated tornado duration as a function of selected environmental parameters. Note that three of the cases have CIN magnitude that is at least twice the standard deviation more than the mean (Figure 5.3d). These cases are considered outliers (gray “x” symbols in Figure 5.3) and are not included in the upcoming regression analysis.

Of all the variables shown in Figure 5.3, 0-3 km storm relative environmental helicity (SREH) produces the strongest simple linear regression (R^2=0.75; Fig. 5.3a). For comparison, 0-1 km SREH is also shown (Figure 5.3b), but the relationship is weaker with R^2=0.48. The thermodynamic indices in Figure 5.3 all individually have a weak linear relationship with simulated tornado duration: convective available potential energy (CAPE), CIN, level of free convection (LFC) height, and lifted condensation level (LCL) height (Figures 5.3c-f; R^2 all near 0). Additionally, neither precipitable water (Pwat) (Figure 5.3g) nor 0-6 km shear (Figure 5.3h) was correlated with simulated tornado duration. In cases where the scatterplot was not linear (e.g., Figures 5.3e, 5.3f, and 5.3g), additional regressions were performed but did not improve the results significantly (not shown).

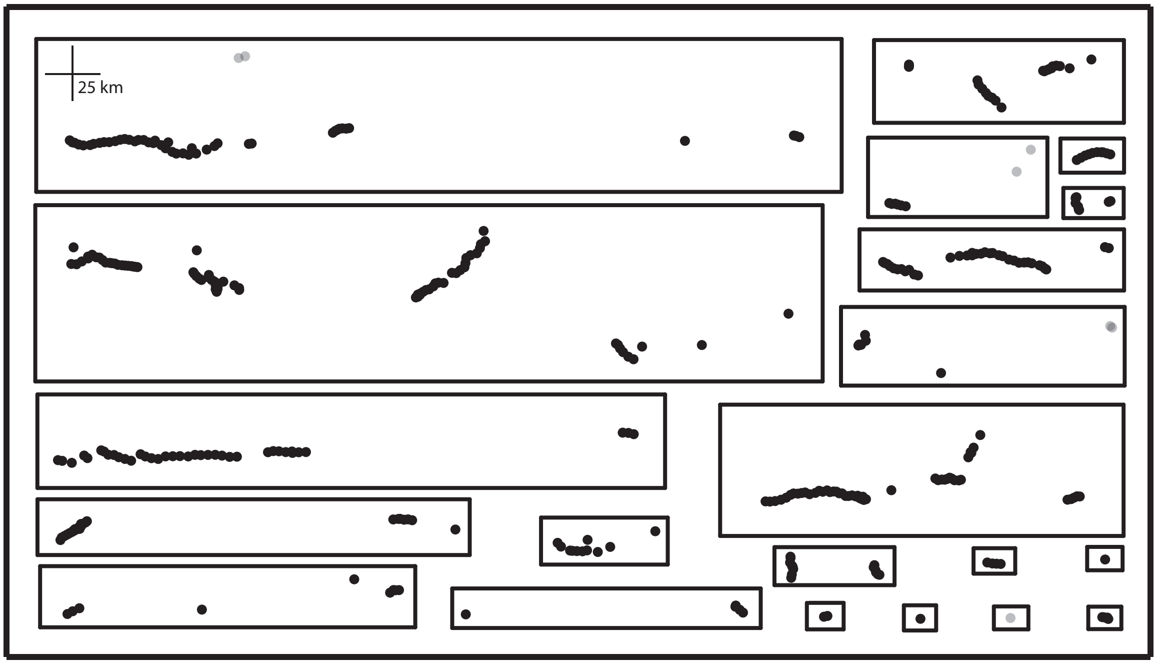

Figure 5.2. Plan view plots of simulated tornado detections at the surface every 30 seconds during each 2 hour simulation. Black dots represent simulated tornado detections that were associated with the main rotating updraft of an objectively and subjectively determined simulated supercell storm. Gray dots represent simulated tornado detections that were significantly displaced from or were missing a parent supercell updraft. All tracks have been rotated such that the time is increasing from left to right.

A multiple linear regression analysis was then performed involving all environmental parameters shown in Figure 5.3. The predictor variables were screened by performing both a forward and backward selection analysis (see Wilks 2006 for an example). Only the results from the backward selection are shown in Table 5.1 due its having a slightly lower mean square error (MSE). To avoid multicollinearity, only one calculation of SREH was used. The 0-3 km SREH was chosen due to its better linear relationship with tornado duration (Figure 5.3), although 0-1 km SREH could also be used. A regression involving 0-3 km SREH, LFC height, CAPE, and Pwat produced the largest F ratio and correlation coefficient and the smallest MSE. The sign of the coefficients in Table 5.1 shows that longer duration simulated tornadoes are associated

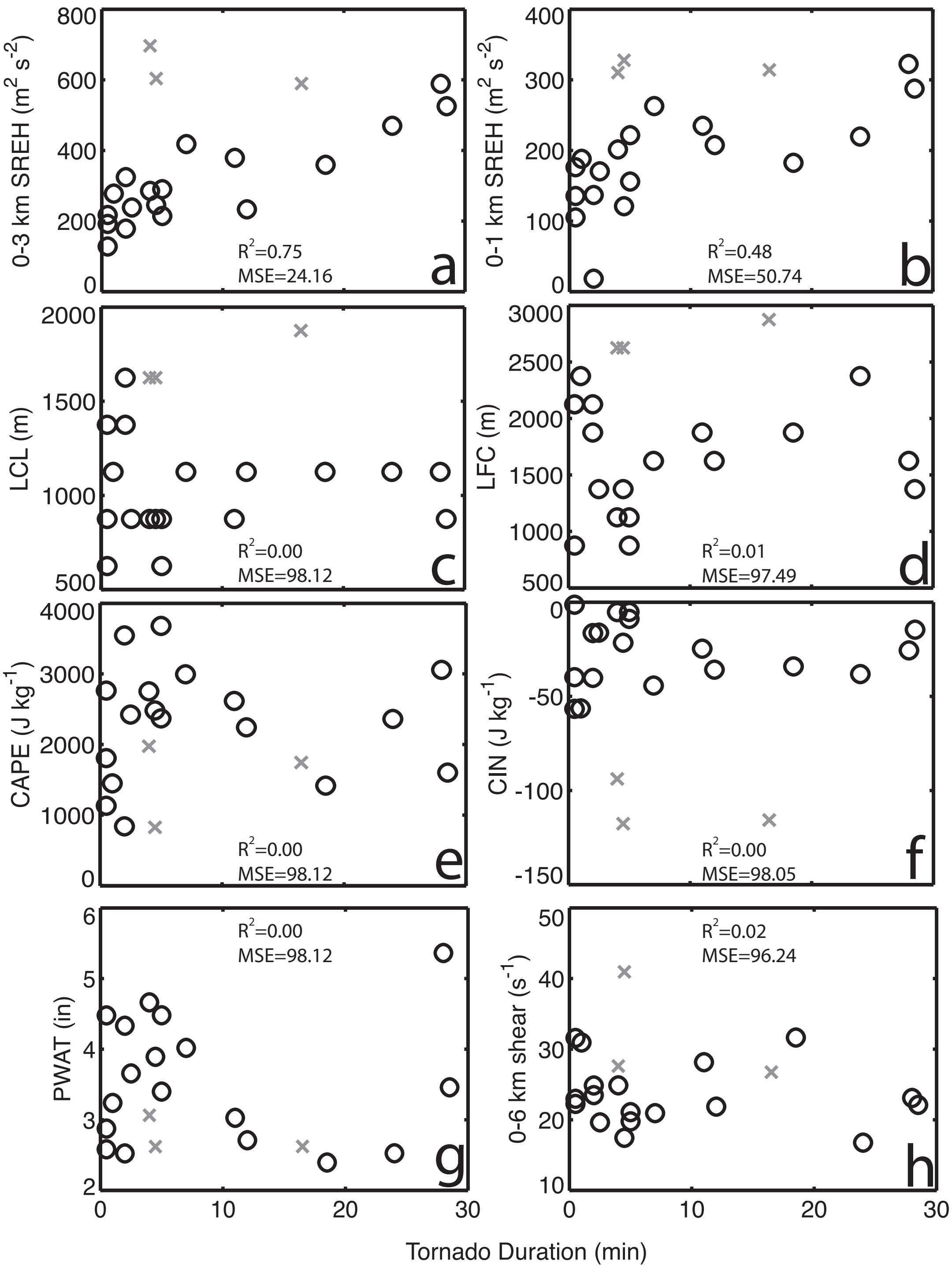

Figure 5.3. Scatter plots of tornado duration vs. select sounding parameters. Gray x's are outlier cases (based on large magnitudes of convective inhibition--CIN). Storm-relative environmental helicity (SREH) is calculated using a storm motion following the method of Bunkers et al. (2000) and thermodynamic variables are calculated assuming a 500 m mixed layer parcel and using the virtual temperature technique introduced by Doswell and Markowski (2004).

with larger values of 0-3 km SREH, lower LFC heights, and smaller values of Pwat and CAPE. The inverse relationship with CAPE is surprising, and somewhat counterintuitive since one might expect larger CAPE/strong updrafts to be associated with stronger vorticity stretching. Perhaps a more complex relationship exists such as larger CAPE leading to stronger updrafts, more precipitation production and increased evaporation as it falls to ground – leading to colder low-level outflow that could disrupt the tornado.

Table 5.1. ANOVA table and regression summary for tornado duration. Columns shown in the ANOVA table are degrees of freedom (df), sum of squares (ss), mean squares (ms) and F ratio (F).

Source	df	SS	MS	F
Total	18	1570.06		
Regression	4	1376.6	1376.6	23.125
Residual	16	193.46		

Variable	Coefficient	s.e.	t-ratio	p value
Constant	12.448	8.1606	1.525	0.1511
0-3 km SREH	0.08	0.0084	9.5534	3x10e-7
LFC	-0.0066	0.0026	-2.4839	0.0274
CAPE	-0.0035	0.0014	-2.4818	0.0275
Pwat	-2.7262	1.462	-1.8647	0.0849

Simulated Tornado Intensity

Figure 5.4 shows scatterplots of maximum pressure drop (an objective measure of tornado intensity) as a function of various environmental parameters. Similar to the regression analysis of tornado duration, the 0-3 km SREH (Figure 5.4a) has the strongest relationship as a possible predictor variable (R^2=0.48), with 0-1 km SREH being the 2nd best predictor (R^2=0.42; Figure 5.4b) and none of the remaining variables showing a strong linear relationship to simulated tornado intensity (Figures 5.4c-4h, R^2 values near 0). Interestingly, both Kerr and Darkow (1996) and Colquhoun and Riley (1996) reported a similar relationship with 0-3 km SREH in their studies relating peak tornado damage intensity (F-scale rating) to sounding parameters.

A multiple linear regression shows that 0-3 km SREH, Pwat, and LFC height are the best predictors for simulated tornado intensity (Table 5.2). This variable combination is obtained from both forward and backward predictor selection. The sign of the coefficients in Table 5.2 shows that the magnitude of the central pressure drop at the surface increases as the environmental 0-3 SREH increases, and as the Pwat and LFC height decrease.

Discussion and Conclusions

RUC-2 proximity soundings associated with significantly tornadic supercells were used to initialize simulations in an idealized cloud model capable of resolving simulated tornadoes. The characteristics of the resulting simulated tornadoes (i.e. longevity and intensity) were compared with environmental sounding parameters. Incidentally, the twenty-one tornadic simulations presented are the most ever in a single study. It was found that the magnitude of 0–3 km SREH is the best single predictor (largest correlation coefficient and smallest MSE) of both simulated tornado duration and intensity. A statistically significant relationship between 0-1 km SREH and simulated tornado duration/intensity was also found, however this relationship was not as strong as the one involving 0-3 km SREH. Interestingly, other sounding parameters (CAPE, Pwat, LFC height) that are *not* good predictors alone do improve prediction of tornado duration and intensity when included within a multiple linear regression. These results provide new avenues of future research into the understanding and study of violent, long-lived tornadoes.

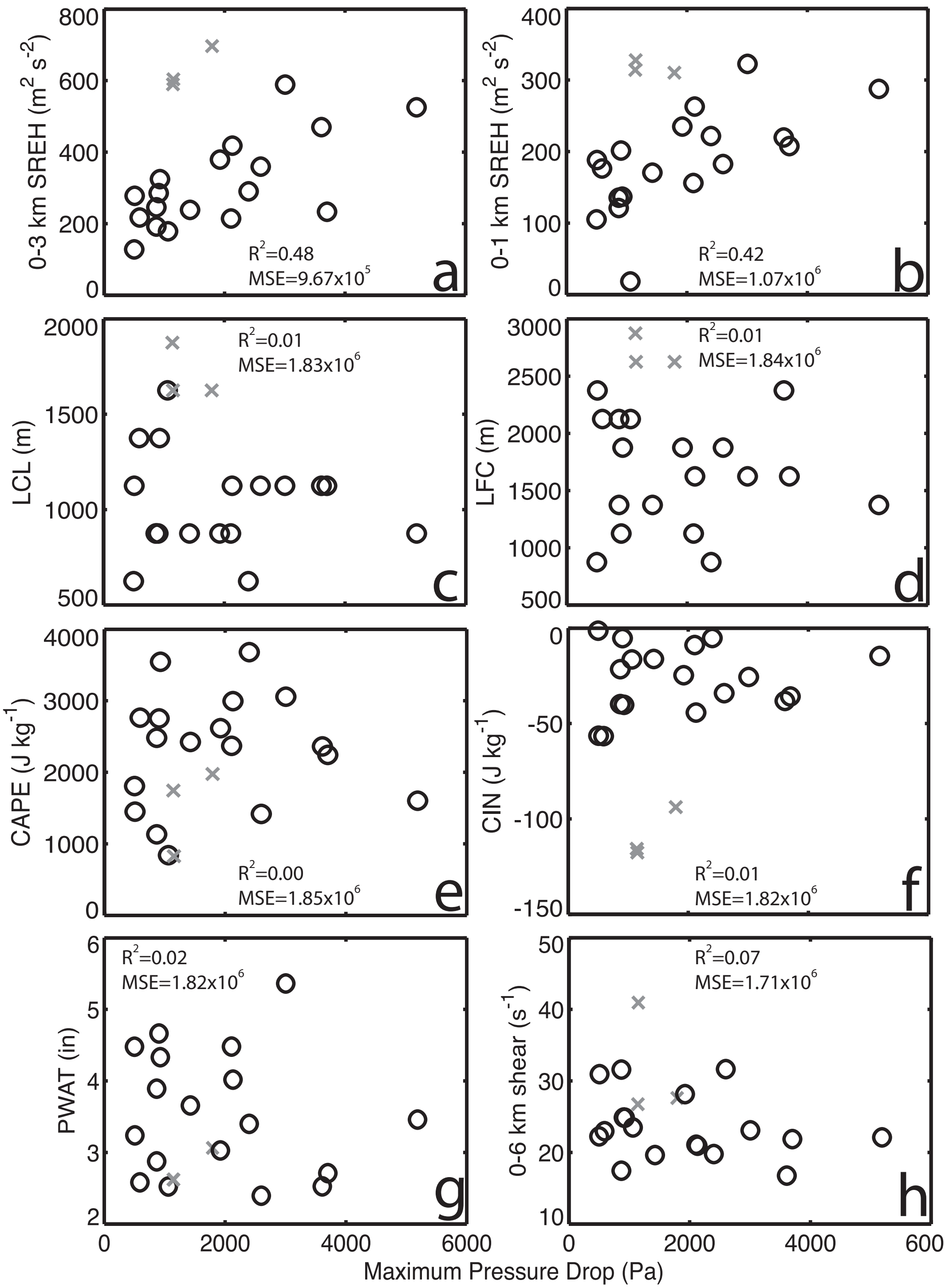

Figure 5.4. Scatter plots of maximum pressure drop vs. select sounding parameters. Gray x's are outlier cases (based on large magnitudes of convective inhibition - CIN). Storm-relative environmental helicity (SREH) is calculated using a storm motion following the method of Bunkers et al. (2000) and thermodynamic variables are calculated assuming a 500 m mixed layer parcel and using the virtual temperature technique introduced by Doswell and Markowski (2004).

Table 5.2. ANOVA table and regression summary for tornado intensity (pressure drop). Columns shown in the ANOVA table are degrees of freedom (df), sum of squares (ss), mean squares (ms) and F ratio (F).

Source	df	SS	MS	F
Total	18	29620870		
Regression	3	22195692	22195692	13.95
Residual	16	7425178		

Variable	Coefficient	s.e.	t-ratio	p value
Constant	5161	1488	3.4665	0.0037
0-3 km SREH	9.5	1.5	6.2504	2.1x10e-5
CIN	-979	267	-3.6639	0.0026
Pwat	-1.7	0.5	-3.374	0.0045

An interesting finding was the three cases labeled as outliers due to the large values of CIN in the soundings. All three cases possess large values of SREH, which indicate a potential for intense, long duration tornadoes. However, two of these cases produced simulated tornadoes for less than five minutes with relatively small central pressure deficits. It is possible that the large CIN in these environments was disruptive to simulated tornado development and/or weakened the parent supercell. Large values of CIN can disrupt downdraft descent and weaken low-level updrafts (Naylor et al. 2012), thus reducing vorticity stretching and negatively impacting vorticity tilting. However, more work is needed in this area before definitive relationships between tornado characteristics and CIN can be established. Lastly, it is noted that the exclusion of these large CIN cases from the statistical analysis did not alter the general conclusions of this study. A statistically significant relationship (albeit weaker) between 0-3 km SREH and tornado intensity/duration is still present when the outliers are included.

A few words of caution for interpreting these results: First, in order for a supercell to produce a long-lived tornado, the environment must also be favorable for a long-lived supercell (see Bunkers et al. 2006) and significant tornadoes (see Thompson et al. 2003; Togstad et al. 2011). Second, the environments in the present simulations were horizontally homogenous, whereas observed supercells can experience time-varying environmental conditions that could affect tornado duration and/or intensity. Lastly, previous studies have shown the intensity and duration of simulated vortices is sensitive to both grid spacing (e.g. Adlerman and Droegemeier 2002) and microphysics representation (e.g. Snook and Xue 2008). The simulations herein need to be repeated—with varying grid spacing and microphysics options—to explain how much of the variance of longevity/intensity is explained by various model parameters within the regression equations.

Future work will also focus on understanding the physical relationship between SREH and simulated tornado characteristics. With the information presented, it is unclear whether larger values of SREH promote simulated tornado longevity due to the associated larger amounts of barotropic vorticity available for tilting and/or whether the larger values of SREH and associated curvature of the low level winds promote a stronger dynamic vertical pressure gradient force [e.g. Brooks and Wilhelmson 1993] that enhances low level vertical vorticity via stretching. Work will also focus on the inter-relationships between simulated tornado characteristics such as intensity, width, duration, path length, and motion. Early results show a strong linear relationship between intensity and duration (not shown), which agrees with the observational results of Colquhoun and Riley (1996).

CHAPTER 6

VORTICITY ANALYSIS OF TORNADIC SIMULATIONS

For tornadogenesis to occur, vertical vorticity (rotation with a spin axis in the vertical) near the surface must be concentrated and stretched to produce strong rotation. Trapp and Davies-Jones (1997) identified two possible ways this process can occur. In the first mode (i.e. Mode I), rotation is first evident at midlevels, generally in the form of a tornado vortex signature (TVS) detected by radar. In the second method (i.e. Mode II), low-level rotation occurs simultaneously, or even precedes midlevel rotation. For Mode II tornadogenesis to occur, some vertical vorticity must already be present near the surface such as along a preexisting boundary or front (e.g. Lee and Wilhelmson 1997) or from outflow from a nearby storm (e.g. Ziegler et al. 2001). Although it was shown by Trapp et al. (1999) that Mode II tornadogenesis occurs often, it will not be considered in this chapter. Since this study utilizes a cloud model with a homogeneous background state, no ambient vertical vorticity will be present in the initial environment. The focus here is on understanding the storm scale mechanisms responsible for Mode I tornadogenesis that occur in isolated supercells after the development of midlevel rotation in an environment initially devoid of vertical vorticity.

In such environments, supercells acquire (and maintain) midlevel rotation through the tilting of horizontal environmental vorticity [e.g. Klemp and Wilhelmson (1978), Rotunno (1981), Davies-Jones (1984) Rotunno and Klemp (1985), Weisman and Rotunno (2000), Davies-Jones 2002]. This process occurs because vortex lines act as if they are frozen in the fluid (See Appendix A for a description of this process). In order for an updraft to acquire *net* rotation, at least some component of the environmental vorticity must be streamwise (i.e. parallel to the storm relative environmental winds). If there is no streamwise component, the environmental vorticity is said to be purely crosswise, and the updraft does not acquire *net* rotation. Davies-Jones (1984) demonstrated that environmental vorticity becomes streamwise when (1) storm motion deviates from that of the environmental winds or (2) the environmental vertical wind shear vector changes direction with height. These two processes are intimately related since changes in environmental vertical wind shear will produce vertical pressure gradients that cause the storm to propagate off of the hodograph (Davies-Jones 1984, Rotunno and Klemp 1982, Weisman and Rotunno 2000, Davies-Jones 2002). Note that in the real atmosphere, (2) will always produce some degree of streamwise vorticity due to the presence of friction in the boundary layer and the Ekman Spiral (Davies-Jones et al. 2001).

As pointed out by Davies-Jones (1982), near-surface rotation cannot be produced in a similar fashion because ascending parcels will not produce substantial vertical vorticity until they are well above the ground. Numerical modeling studies have repeatedly shown that low-level rotation does not develop until downdrafts reach the surface [e.g. Rotunno and Klemp (1983), Davies-Jones and Brooks (1993), Walko (1993), Trapp and Fiedler 1995, Wicker and Wilhelmson (1995; hereafter WW95), Adlerman et al. (1999)]. Although these studies agree that the development of near surface vertical vorticity awaits the presence of a downdraft, they do not agree on the exact mechanism that produces this vorticity. It has been suggested that downdrafts can produce positive (cyclonic) near-surface vertical vorticity through stretching of

- tilted horizontal vorticity that was baroclinically generated (i.e. vorticity generated by the storm's own horizontal density gradients),
- tilted barotropic horizontal vorticity (i.e. vorticity produced by the vertical wind shear of the environment), or,
- vertical vorticity that is transported to the surface.

A combination of these processes contributes to the rotation in the low-level mesocyclone (Klemp and Rotunno 1983, Davies-Jones and Brooks 1993, Adlerman et al. 1999, Markowski et al. 2008), however the relative importance of these processes to the development of near surface rotation and tornadogenesis varies between cases. Modeling studies by Davies-Jones and Brooks (1993) and Grasso and Cotton (1995) found that the largest source of vertical vorticity in the low-level mesocyclone is baroclinically generated in air that descends cyclonically around the updraft. Furthermore, Markowski et al. (2003) and Davies-Jones (2008) demonstrated that tornadogenesis could be induced without tilting of horizontal vorticity, purely through the transport of vertical vorticity to the surface via downdrafts and curtains of rain that wrap cyclonically around the low-level mesocyclone. However, the Brandes (1984) observational study and WW95 numerical study concluded that the primary source of cyclonic vertical vorticity was via tilting and stretching of horizontal vorticity originally generated along the forward flank gust front (see Fig. 6.1), and that descending parcels either did not strongly contribute to low-level vertical vorticity or, as in WW95, contributed adversely to vorticity of the opposite sign.

Regardless of the source of near surface vertical vorticity, sufficient amounts are concentrated to tornadic levels through convergence amplification (stretching) in a region of strong gradients in the vertical velocity field where the low-level inflow meets the storm outflow (e.g. Fujita 1975, Brandes 1984, Adlerman et al. 1999, Markowski et al. 2003).

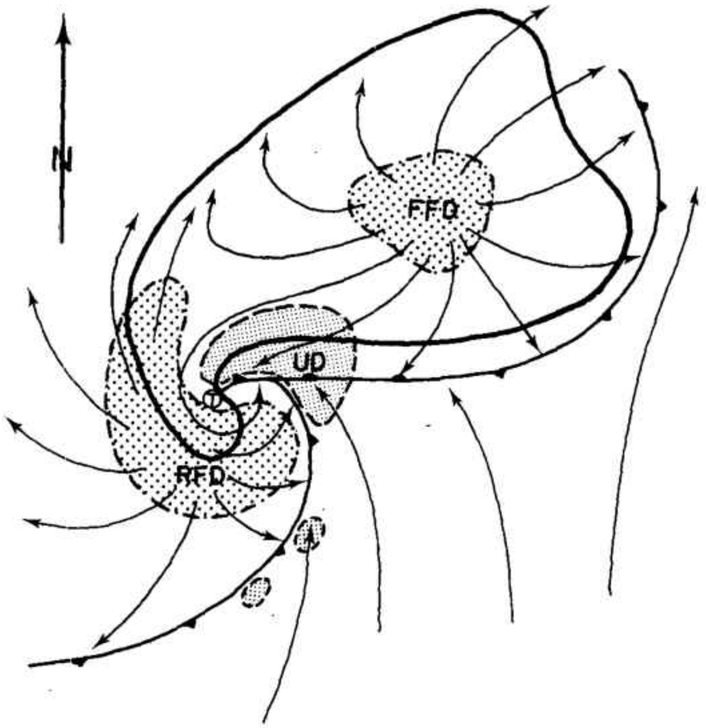

Figure 6.1. Schematic of a supercell thunderstorm. Thick black line represents radar echo, UD represents the region of updraft, FFD is the forward flank downdraft, RFD is the rear flank downdraft, and streamlines are shown in thin black lines. The small "T" indicates the location of the tornado in the occlusion where the RFD gust front has overtaken the FFD gust front. From Lemon and Doswell (1979).

In this chapter, attempts are made to further the current understanding of tornadogenesis by analyzing the processes important to the development of tornado-like vortices in simulated supercells. The idealized model that is used represents the environment as horizontally homogeneous - following many prior supercell modeling studies (e.g Weisman and Klemp 1982,84, Adlerman et al. 1999). Previous observational and modeling studies have suggested that non-homogeneous features (i.e., pre-existing baroclinic regions and vertical vorticity) can influence low-level rotation and tornado potential in supercells (e.g. Maddox et al. 1980, Markowski et al. 1998, Atkins et al. 1999, Fierro et al. 2006; Richardson et al. 2007). By excluding these non-homogeneous features, the ability (or inability) of a storm to produce a tornado should be based primarily on the near-storm environment (NSE). However, aspects of the model itself and internal storm processes may influence tornadogenesis, particularly the microphysics parameterization (through its impact on the cold pool and baroclinic horizontal vorticity production).

The following questions will be addressed:

- **What is the most likely source region of near surface vertical vorticity in the tornadic cases?** Are descending parcels (i.e. rear flank downdraft) or near surface parcels (i.e. inflow parcels along the forward flank) the primary contributor of tornadic vertical vorticity in a majority of the cases?
- **What is the relative importance of baroclinic and barotropic vertical vorticity?**

Both processes are inevitably present in supercells. However, is one process (and source region) consistently dominant in the tornadic supercells?

Methodology

The model setup is identical to that in Chapter 5. That is, simulations were performed with 100 m grid spacing in both the vertical and horizontal for 2 hours. For more details about the model configuration, refer to Chapters 2 and 5.

Trajectory Analysis

Trajectory analysis was performed with all of the tornadic cases from Chapter 5 at the time of tornadogenesis—defined as the first instance that the tornado detection algorithm was triggered (see Chapter 5 for details on the tornado detection algorithm). Trajectories were seeded within the tornado (at the time of tornadogenesis) at grid points where the pressure perturbation was less than –3 mb (between z=100 m and z=500 m) and were traced backwards 900 s (consistent with previous studies utilizing trajectories to determine the source region of air parcels—e.g. Adlerman et al. 1999), using model history files generated at 5 s intervals. In the interest of computational expense, an upper limit for the number of trajectory parcels was set. This limit was 100 trajectory parcels for each simulation, and all simulations reached this limit. Dahl et al. (2012) showed that this temporal resolution is sufficient to compute accurate backwards trajectories. Parcel positions were calculated using a 4th order, multi step Runge-Kutta technique—the same as used by Lee and Wilhelmson (1997). After each step along the integration, the scalar and wind vector properties of the parcel were determined using tri-linear interpolation from the surrounding eight grid points. In addition, vorticity tendencies along the trajectories were calculated using first-order discretizations of the following equations from Klemp and Rotunno (1983):

$$\frac{d\zeta}{dt} = \omega_h \cdot \nabla_h w + \zeta \frac{\partial w}{\partial z}, \tag{6.1}$$

$$\frac{d\omega_h}{dt} = \text{[illegible]} \nabla v_h + \nabla \times \left(B\hat{\mathbf{k}} \right), \tag{6.2}$$

where ω_h is the horizontal component of the vorticity vector, w is the vertical velocity, B is buoyancy, and v_h is the horizontal component of velocity. The terms on the rhs of (6.1) represent the generation of vertical vorticity through the tilting of horizontal vorticity and stretching of existing vertical vorticity, respectively. These two terms are referred to simply as ‘tilting’ and ‘stretching’ herein. In the absence of existing vertical vorticity, positive tilting produces cyclonic vertical vorticity (and “negative tilting” produces anticyclonic vertical vorticity). The stretching term acts to increase (or decrease, depending on the sign of the vertical acceleration) the magnitude of the anticyclonic or cyclonic rotation. Additional terms such as solenoidal generation of vertical vorticity—which vanishes due to use of Boussinesq approximation—and turbulent mixing are neglected, following prior studies (e.g. Klemp and Rotunno 1983; Wicker and Wilhelmson 1995; Adlerman et al. 1999). Those neglected processes may also influence vorticity generation/dissipation in the actual model. Equation (6.2) represents the production of horizontal vorticity. The first term on the rhs of (6.2) is the production of horizontal vorticity through the stretching and tilting of existing vorticity while the second term represents baroclinic generation. The baroclinic term in (6.2) is separated into streamwise and crosswise components by projecting it onto the horizontal wind vector, $\boldsymbol{v}_h$.

In upcoming trajectory plots the seeding time is called t=900s. At each point along the trajectory, the terms in (6.1) and (6.2) are calculated. Once the trajectories have been traced backwards to their origin positions (at t=0 s), they are separated into the following categories:

1. Trajectories that descend from aloft to the surface, without a significant upward motion during the trajectory.
2. Trajectories that originate aloft but experience a substantial upward motion before

descending to the surface.

3. Trajectories that originate near the surface, rise upwards, and then descend towards the surface
4. Trajectories that originate near the surface and steadily rise as they approach the tornadic circulation.

These trajectories are illustrated conceptually in Fig 6.2.

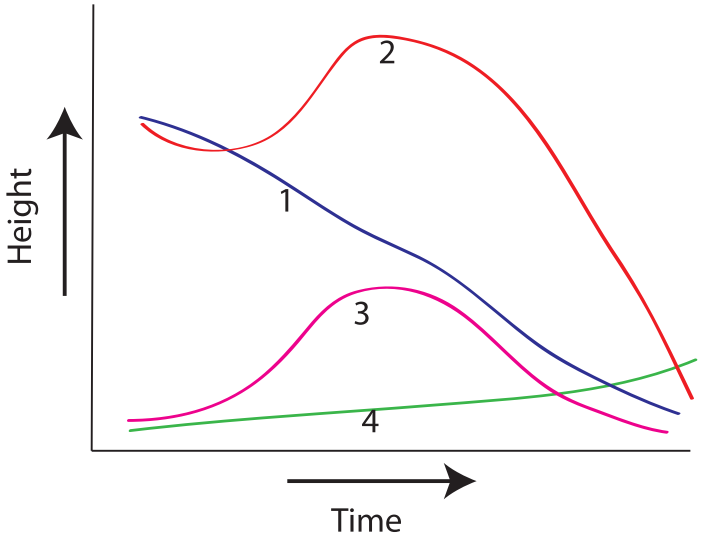

Figure 6.2: Conceptual diagram of the different trajectory classifications.

Results

As discussed in Chapter 5, 21 cases produced tornadoes. Here, trajectory analysis is only performed for those cases that produce an initial tornado that is mesocyclone-associated. Because two of the cases produced an initial brief tornado not associated with the main mesocyclone, 19 tornadic cases are left for analysis. An overview of these simulations is shown in Fig. 6.3. Note that trajectory types 1, 2, and 3 (cf., Fig 6.2) follow very similar horizontal paths and all descend. Thus these three groups are combined into one category herein and simply referred to as ‘descending’ trajectories. The trajectories in category 4 primarily originate to the east of the tornadoes along or south of the forward flank gust front and will be referred to as ‘rising’ trajectories. From Fig. 6.3, three distinct types of tornadoes are evident: tornadoes fed primarily by rising air parcels; tornadoes fed primarily by descending air parcels; and tornadoes that contain both rising and descending air parcels. The tornadoes composed primarily of rising parcels are the most rare, with only two cases producing tornadoes containing more than 90% rising parcels (Fig. 6.4). There are six cases in which 90% of the tornado trajectories are descending, with the remaining eleven cases containing at least 20% trajectories from each category. Even in the cases containing both rising and descending trajectories, there are usually more descending than rising trajectories (Fig. 6.4). However, since there are cases that produced a tornado with only rising air parcels, and several more that produced a tornado almost entirely with descending parcels, it seems that descending parcels and rising parcels alone are capable of initiating tornadogenesis. What needs to be determined is how these parcels produce large values of vertical vorticity.

Figure 6.5a shows the net production of vertical vorticity, ζ, via the tilting of horizontal vorticity (a vorticity vector contained within the horizontal plane). The net value of a particular variable is determined for each case by integrating that variable along the trajectory and then averaging over all trajectories in the group. Here, positive net tilting in a particular case means that, on average, positive ζ production via tilting along a trajectory was larger in magnitude than negative production via tilting. Net tilting by rising parcels is larger than in descending parcels in eight of the ten cases that contain air parcels from both categories (Fig 6.5a). Three of these cases are characterized by descending air parcels with negative net tilting. However, the net ζ production via

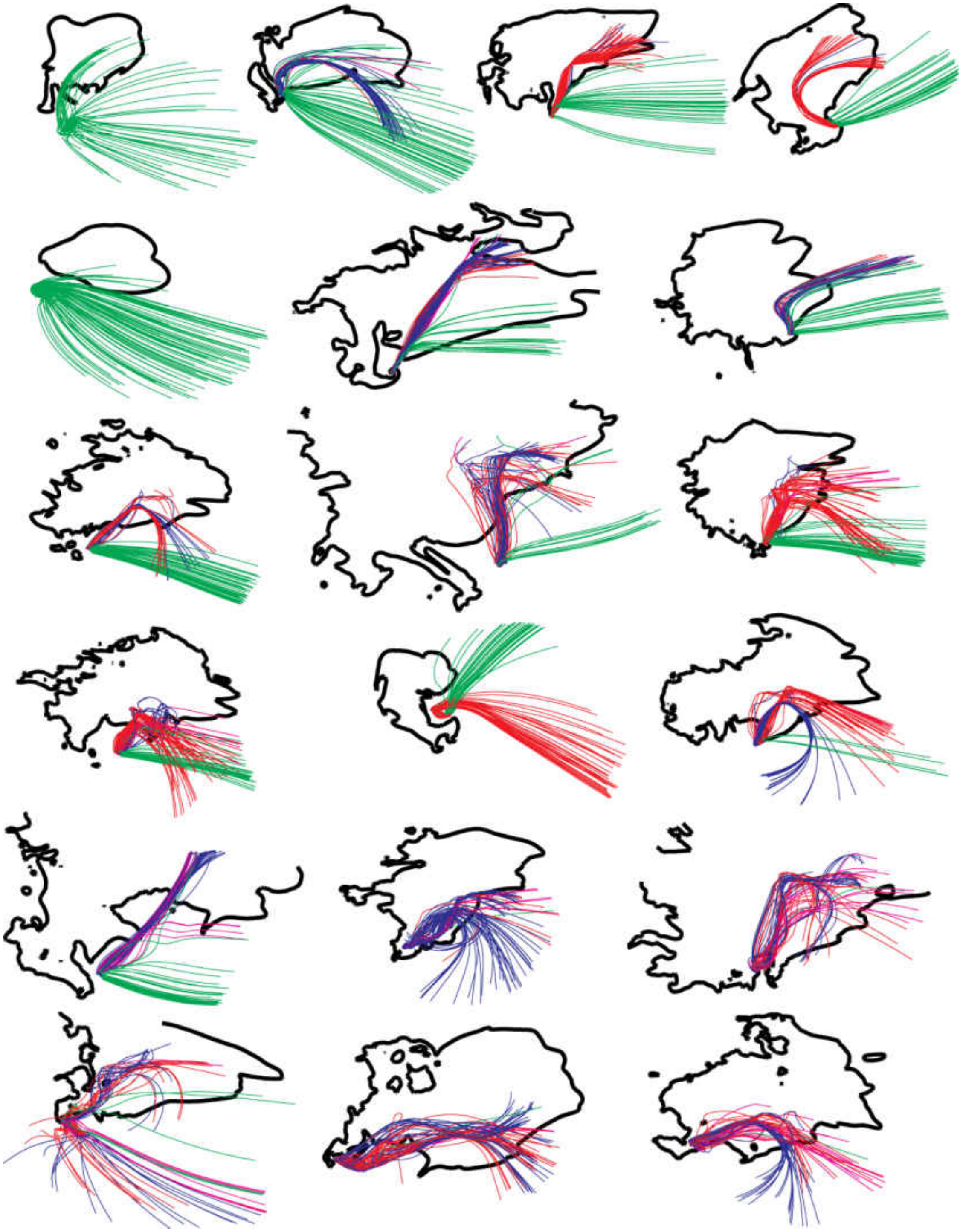

Figure 6.3: Overview of the 19 tornadic cases analyzed in this chapter. The thick black line is the 30 dBZ contour of simulated radar reflectivity. Air parcel trajectory paths are shown by the thin colored lines. Colors are the same as those shown in Fig. 6.2.

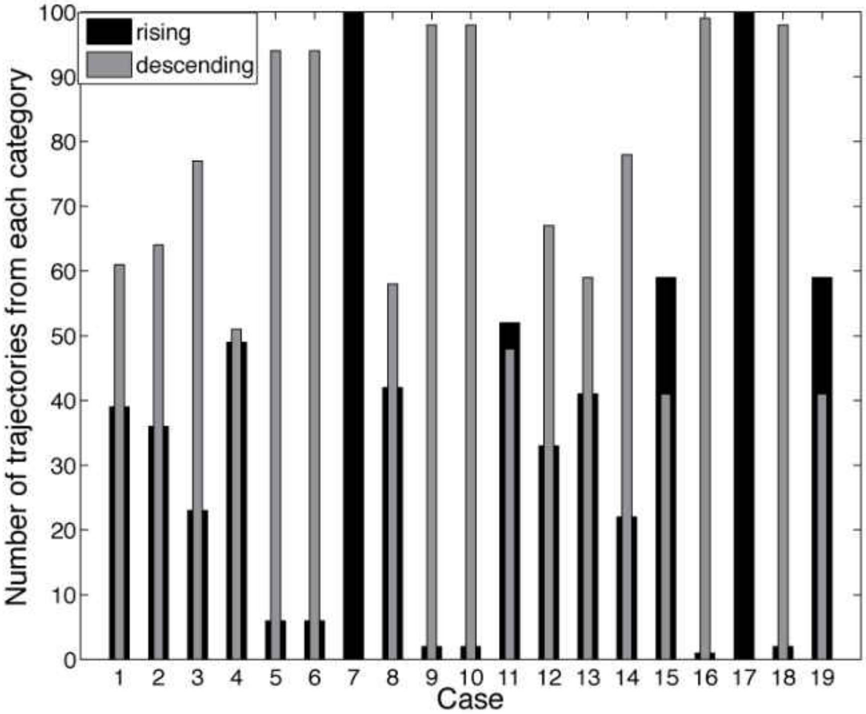

Figure 6.4. Number of trajectories from the descending and rising categories for each case. The total number of trajectories in each case is 100.

stretching (Fig 6.5b) is *positive* in these three cases and the average ζ at the end of the trajectories is also positive (Fig. 6.5c).

For each case, the sum of the tilting and stretching terms shown in Fig. 6.5 was integrated along the path of each trajectory and then averaged (Fig 6.6a)—representing the average net vertical vorticity for each case (assuming the trajectories began with zero vertical vorticity and that tilting and stretching are the only sources of vertical vorticity). These values were compared to the average ending vertical vorticity in each case (Fig. 6.6b). The difference between these two quantities (i.e. average error) is shown in Fig. 6.6.c, with positive (negative) values meaning that the integrated form of (6.1) is larger (smaller) than the final vertical vorticity calculated from model output. In general, most

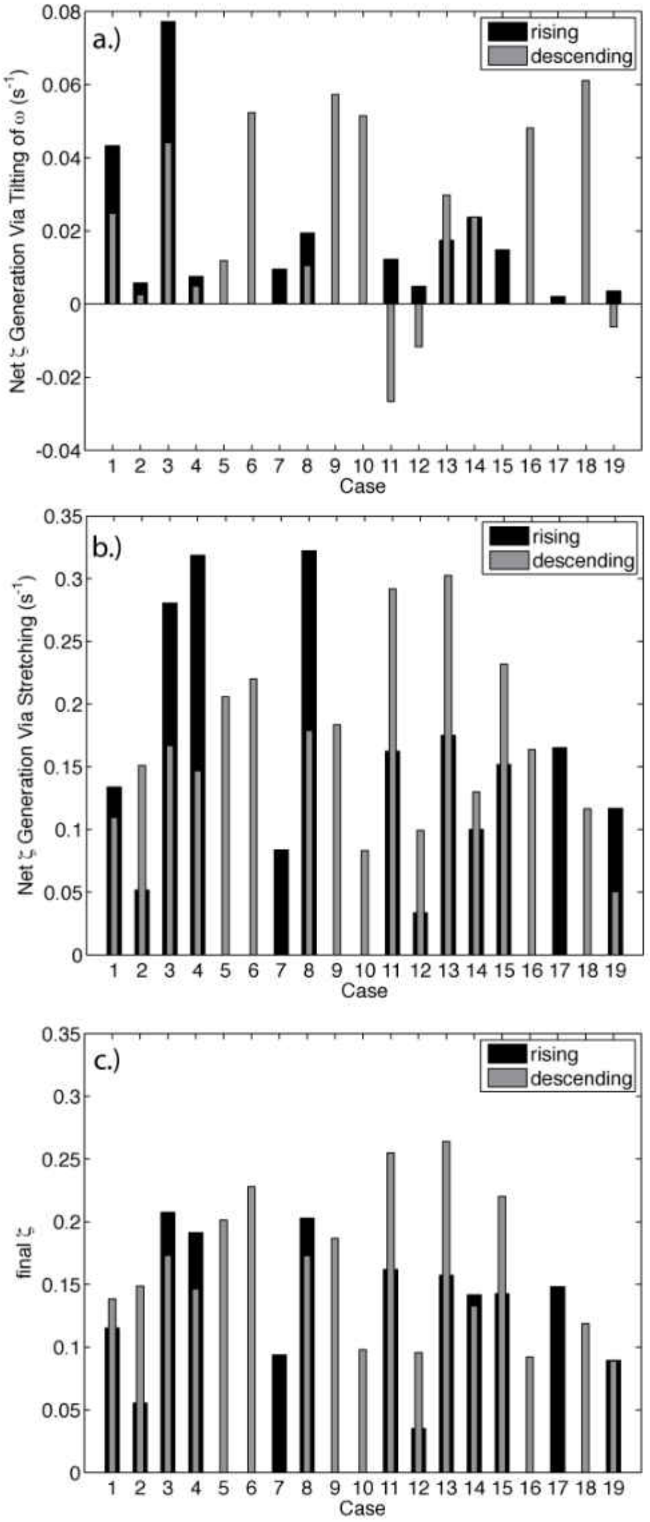

Figure 6.5: Comparison of (a) net tilting, (b) net stretching, and (c) average vertical vorticity at tornadogenesis time for the various cases. In all plots, the value from a trajectory group (i.e. rising or descending) is set to 0 in a particular case if less than 10% of all parcels are from that group.

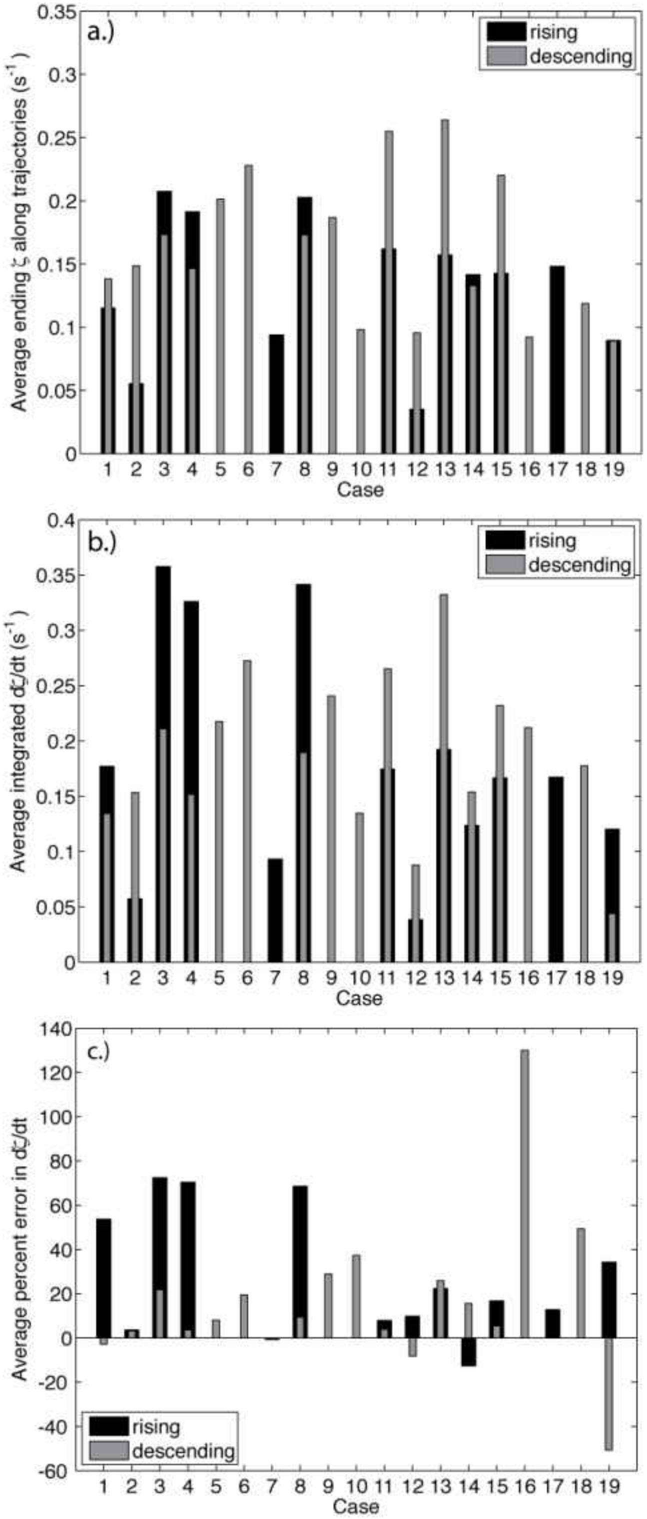

Figure 6.6. Comparison of (a) average integrated vorticity generation via tilting and stretching, (b) average ending vertical vorticity values along the trajectories, and (c) the percent difference between these two terms.

of the error values are positive—meaning that the terms in (6.1) are greater than the final value of vertical vorticity. This is not surprising since sub-grid mixing in the numerical model (not considered in equation 6.1) should act to reduce the magnitude of ζ. In just over half of the cases, the magnitude of the error is less than 30%. Most of the large errors (i.e. > 40%) occur in the rising parcels.

To better understand how the terms in (6.1) evolve over the history of the trajectories, vorticity production is examined at all times along all trajectories for all cases (Fig. 6.7). A distinct contrast between vertical vorticity evolution in the descending and rising parcels is present (Figs. 6.7a,d). Almost all of the rising trajectories maintain a positive value of ζ, while many of the descending parcels have negative ζ. Strong positive tilting occurs at the end of both the descending (Fig. 6.7b) and rising trajectories (Fig. 6.7e), with the tilting in the descending parcels being of larger magnitude—likely due to stronger horizontal gradients in vertical velocity. However, negative tilting in many of the descending parcels seems to counteract the large values of positive tilting. This explains why, in many cases, the net tilting in descending parcels (Fig. 6.5a) was relatively small, or even negative. A similar trend is seen in the stretching term (Figs 6.7c,f). Positive values of stretching in the descending parcels seem to be counteracted by negative values, while stretching in the rising parcels is mainly positive

Several cases were further analyzed to investigate the vorticity evolution in different scenarios: large positive net tilting in descending and rising parcels (case 3; Fig. 6.5); negative net tilting in descending parcels and small net positive tilting in rising parcels (case 12; Fig. 6.5); net positive tilting in descending parcels with minimal contribution from rising parcels (case 5; Fig. 6.5); and small positive net tilting in rising parcels with large net stretching (case 17; Fig. 6.5).

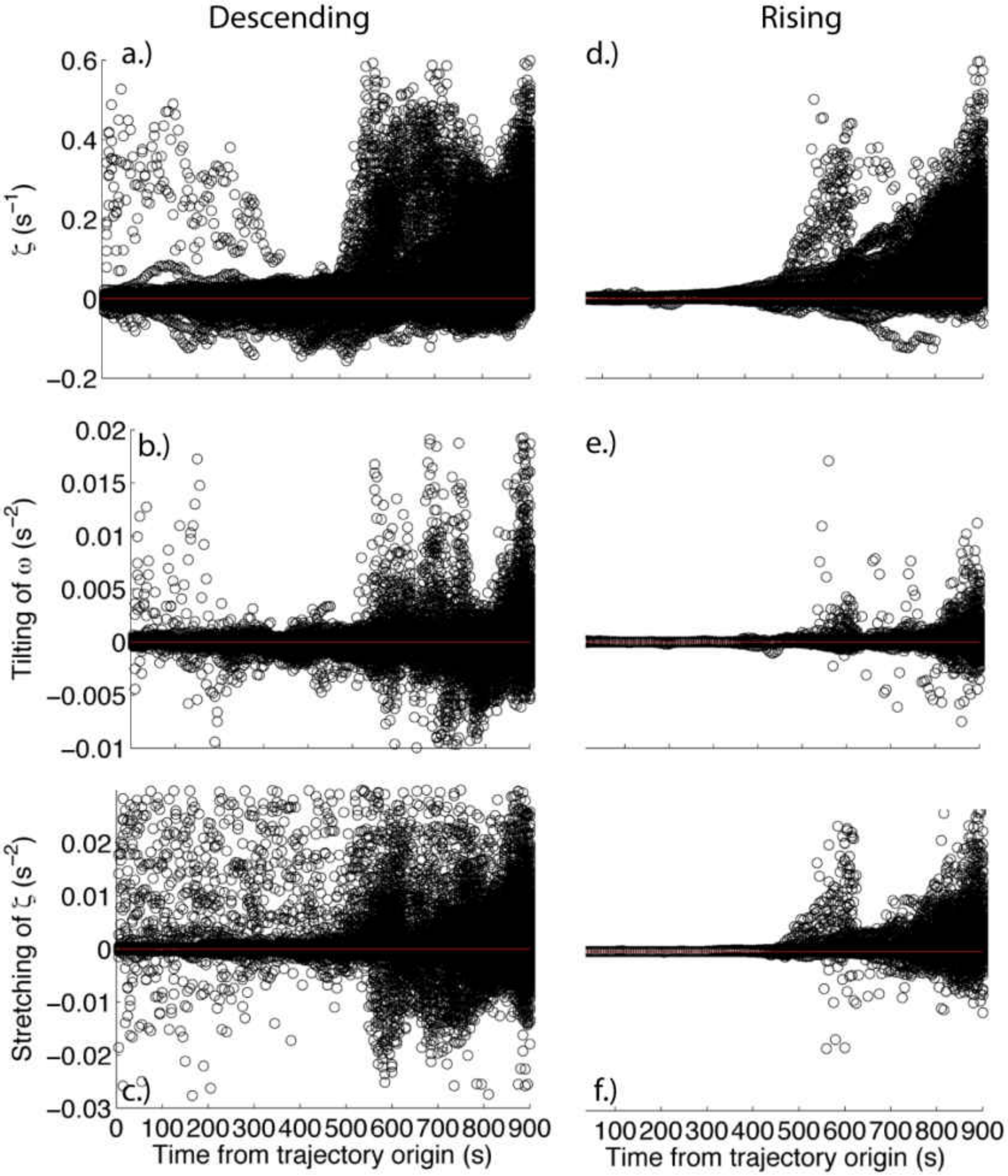

Figure 6.7. Time series of vorticity production along every trajectory in every case for the descending parcels (a-c) and rising parcels (d-f). The x-axis shows the *relative* time beginning at t=900 s (tornadogenesis) and ending at t=0 s. Tornadogenesis happens at a different cloud time in each simulation.

Case 3

Figure 6.8 shows an overview of the trajectories in case 3. The descending parcels approach the tornadic circulation from the north-northeast, while the rising parcels approach from the east and turn towards the southwest at later times. The vertical vorticity along the trajectories does not become large until the latter half of the trajectory paths (Fig. 6.9a,b). One difference between the two groups of trajectories is that the rising parcels maintain positive vertical vorticity along their path, while many of the descending parcels develop negative vertical vorticity during the first half of the trajectory path. This negative vertical vorticity corresponds with negative tilting in many of the parcels (Fig. 6.9b). In contrast, almost all of the rising parcels maintain near zero or slightly positive tilting during the first half of their path (Fig. 6.9e). In both the rising and descending groups, the sharp increase in vertical vorticity that occurs around t=600 s corresponds to large values of tilting (Figs. 6.9b,e) and stretching (Figs. 6.9c,f).

The time evolution of vertical vorticity and tilting are again shown in Fig 6.10. An interesting feature in the descending parcels is that negative vertical vorticity and negative tilting (Figs 6.10a,b) occur primarily when the parcels are descending (Fig. 6.10c). Although there is a small, short-lived increase in tilting at t=400 s that corresponds to descending motion, most of the positive values of ζ and tilting occur only *after* the parcels reach the surface and begin ascending towards the tornadic circulation. The same is true in the rising parcels—positive values of vertical vorticity and tilting mainly occur after the parcels begin to ascend (Figs. 6.10,e-g). For both trajectory groups, production of positive ζ is associated with increases in baroclinic generation of horizontal vorticity. Horizontal stretching production is not calculated. Note that in Fig.

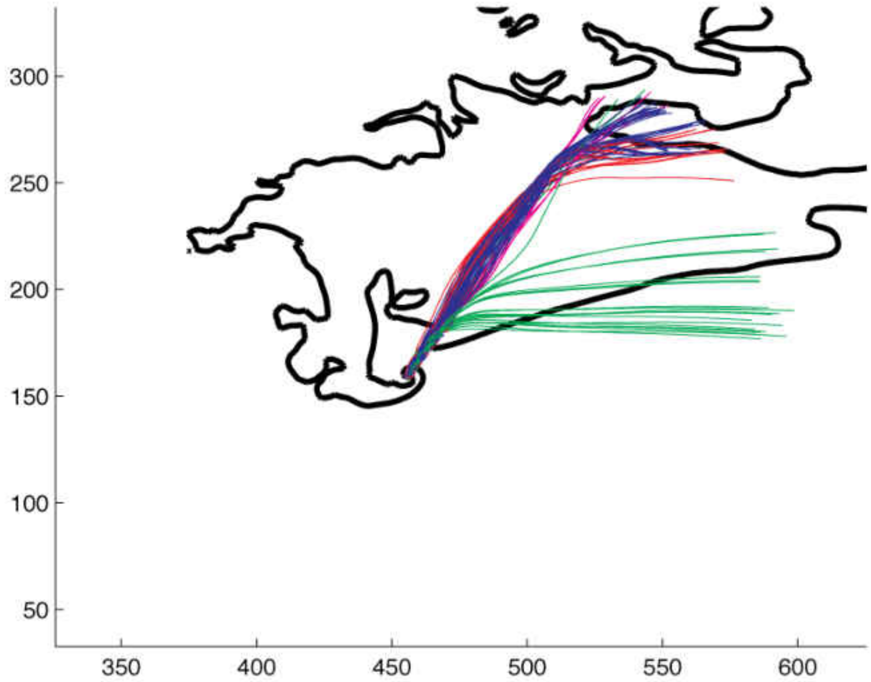

Figure 6.8. Overview of case 3. The thick black line is the 30 dBZ contour of simulated radar reflectivity. Air parcel trajectory paths are shown by the thin colored lines. The colors are the same as those shown in Fig. 6.2.

6.10 (and herein), only the streamwise component of baroclinic generation is analyzed in the rising parcels. In the descending parcels, total baroclinic generation is analyzed.

While it is widely believed that the streamwise component is the most important in rising (i.e. forward flank) parcels, several studies have suggested that the crosswise component of baroclinicity in descending parcels may also be of importance [e.g. Straka et al. (2007); Markowski et al. (2008)] and this is why the total baroclinic generation is shown for descending parcels.

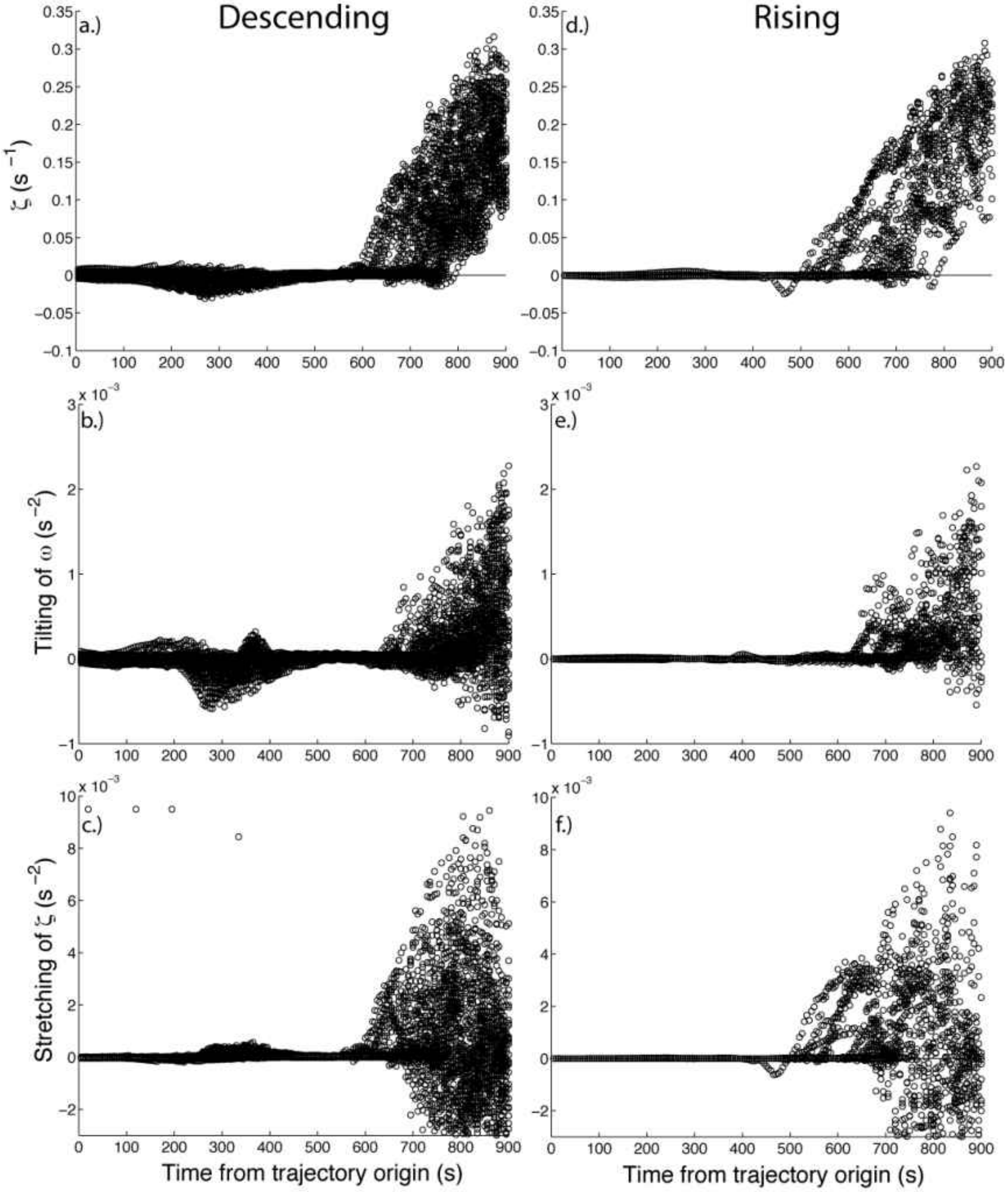

Figure 6.9. Vertical vorticity production vs. time for (a-c) the descending parcels and (d-f) the rising parcels in case 3.

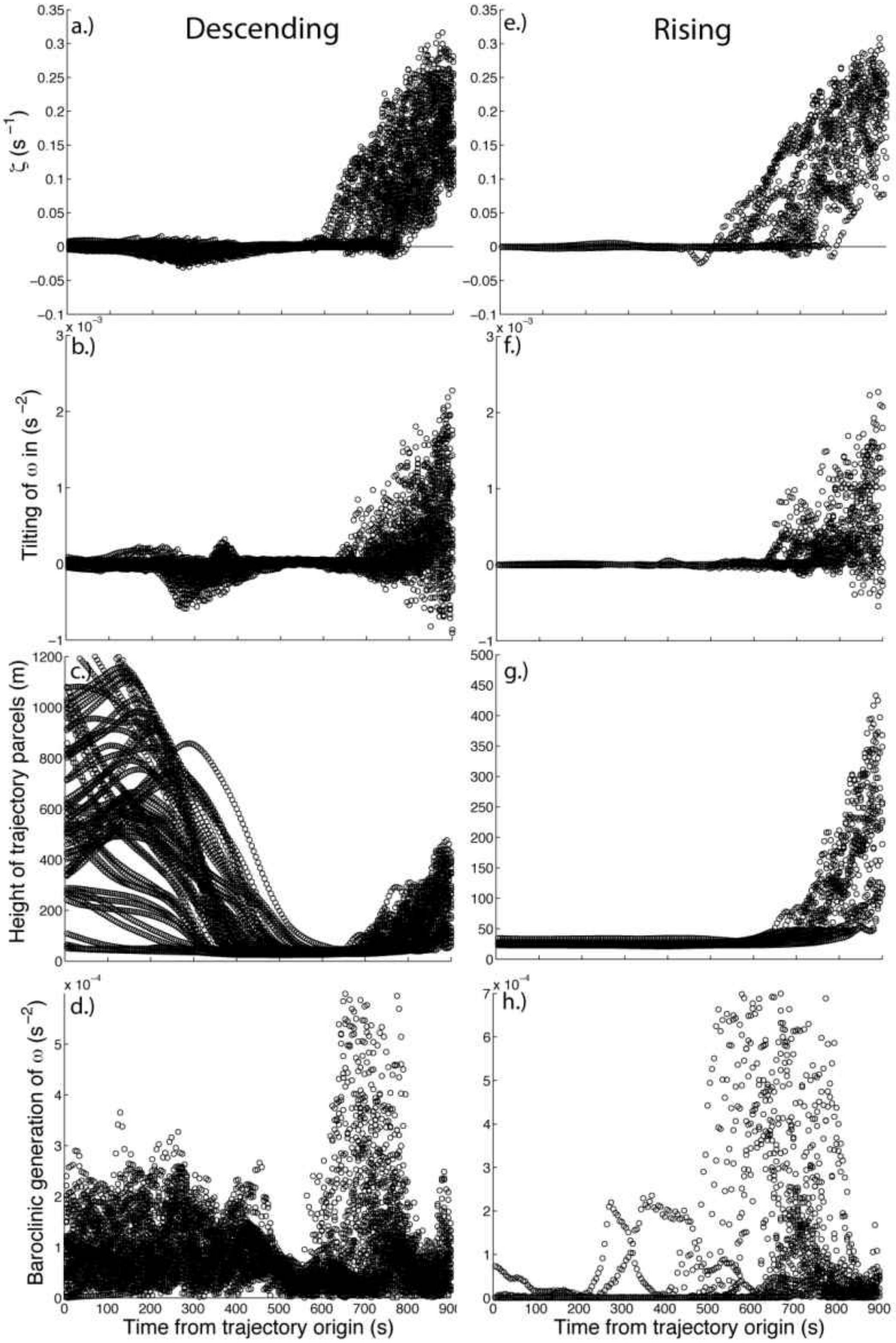

Fig. 6.10. Time tendencies of vertical vorticity (a,e), tilting (b,f), parcel height (c,g) and baroclinic generation of horizontal vorticity (d,h) in case 3. Descending parcels are shown in the left column and rising parcels in the right column. Note that only the streamwise component of baroclinic horizontal vorticity generation is shown in h.

Case 12

In case 12, the rising parcels approach the tornadic circulation from the northeast while the descending parcels approach from the southeast and wrap around the main updraft (Fig. 6.11). In this case, the descending group of trajectories is dominated by parcels that experience some ascent before descending to the surface. This ascent occurs as the parcels wrap around the north side of the updraft. When the parcels move towards the western edge of the updraft, they begin to descend to the surface.

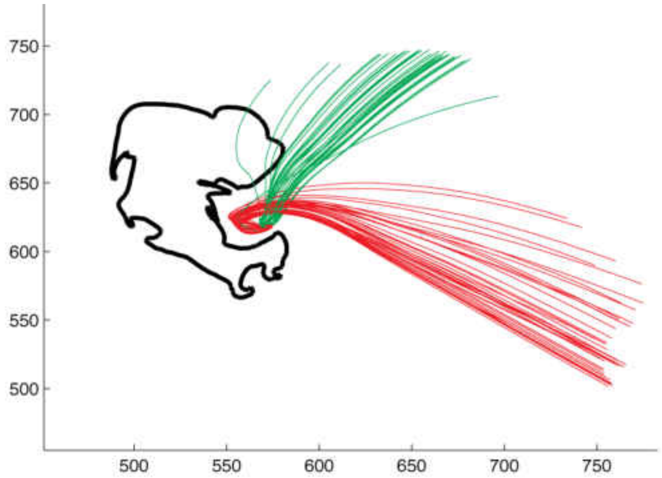

Figure 6.11. Overview of case 12. The thick black line is the 30 dBZ contour of simulated radar reflectivity. Air parcel trajectory paths are shown by the thin colored lines. The colors are the same as those shown in Fig. 6.2.

The descending parcels in case 12 do not experience any large change in vertical vorticity until after *t*=600 s (300 s prior to tornadogenesis; Figs. 6.12,a-c), while the rising parcels only produce substantial vertical vorticity during the last 100 s of their path (Figs. 6.12, d-f). Similar to case 3, the rising parcels produce mainly positive ζ while the descending parcels first produce negative ζ, primarily through tilting. After this initial production of negative ζ, tilting and stretching becomes positive in some trajectories, and ζ becomes positive (or at least less negative) during the last 60 s or so. An interesting feature of the descending parcels is that positive stretching (Fig. 6.12c) is associated with both negative and positive ζ around t=800 s. From equation (6.1), if the stretching term is positive and ζ is negative, $\frac{\partial w}{\partial z}$ is also negative—suggesting that positive stretching is occurring in downdrafts with negative ζ, thereby making ζ less negative with time. This is illustrated in Fig. 6.13. For the first 600 s of the descending trajectories, ζ and tilting are near zero (Figs. 6.13a,b). During this time, the parcels are traveling horizontally or rising (Fig. 6.13c). After 600 s, many parcels begin to descend and ζ and tilting become negative. Once the parcels descend to the surface (or slightly above) around t=800 s, tilting and stretching both become positive—changing the sign of ζ to positive. As in case 3, baroclinic production of horizontal vorticity sharply increases after the parcels reach the surface (Fig. 6.13d), and is coincident with positive tilting.

The rising parcels behave similarly to those in case 3 in some ways and different in other ways (Figs 6.13e-g). Similarly, during the latter half of the trajectory paths, the production of positive ζ is coincident with rising motions as the trajectories approach the incipient tornado and occurs after an increase in baroclinic generation (Fig. 6.13h). The production of negative ζ along these trajectories is small. Different from case 3, large values of tilting and stretching in rising parcels occur only during the last 100 s.

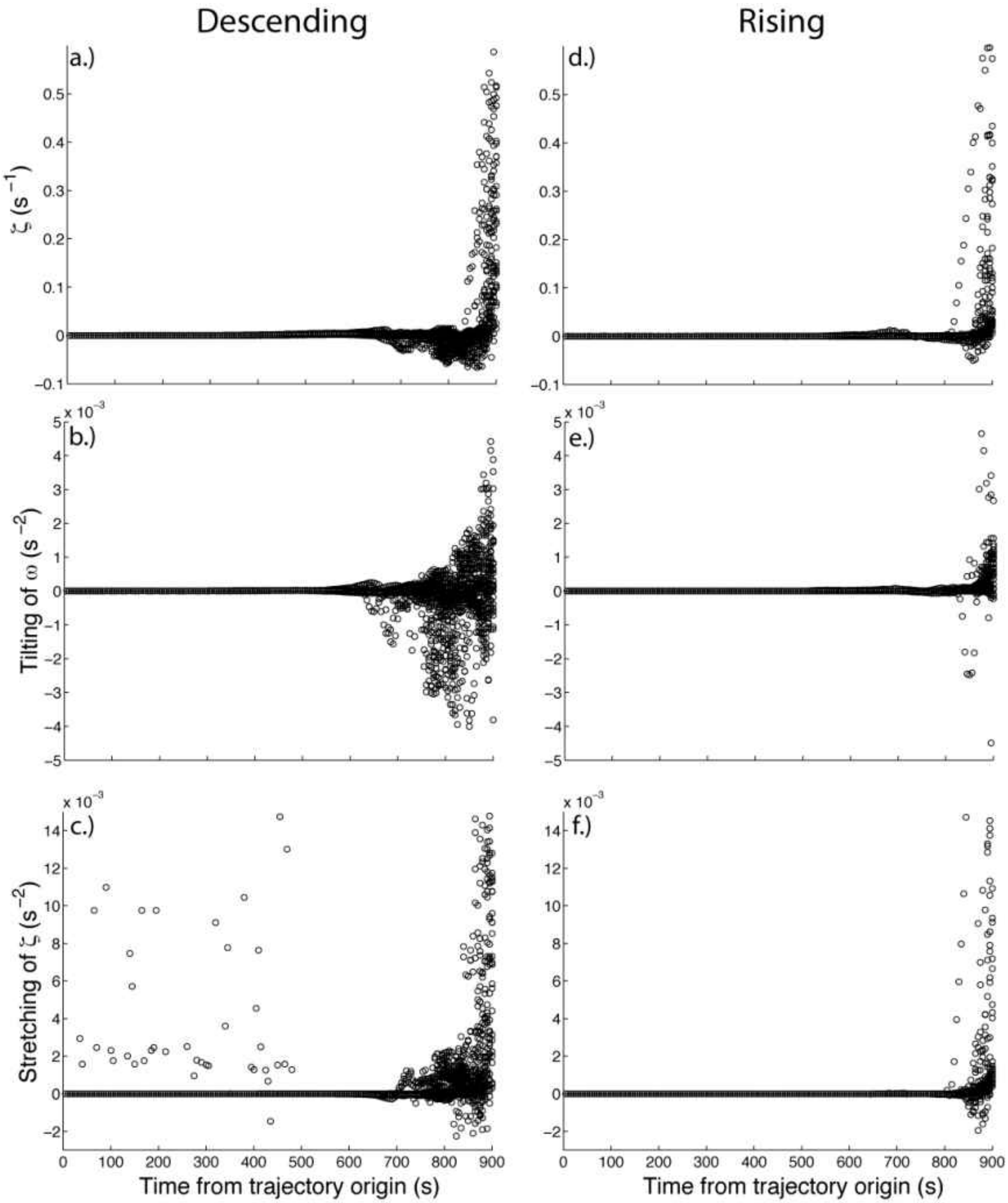

Figure 6.12. Vertical vorticity production vs. time for (a-c) the descending parcels and (d-f) the rising parcels in case 12.

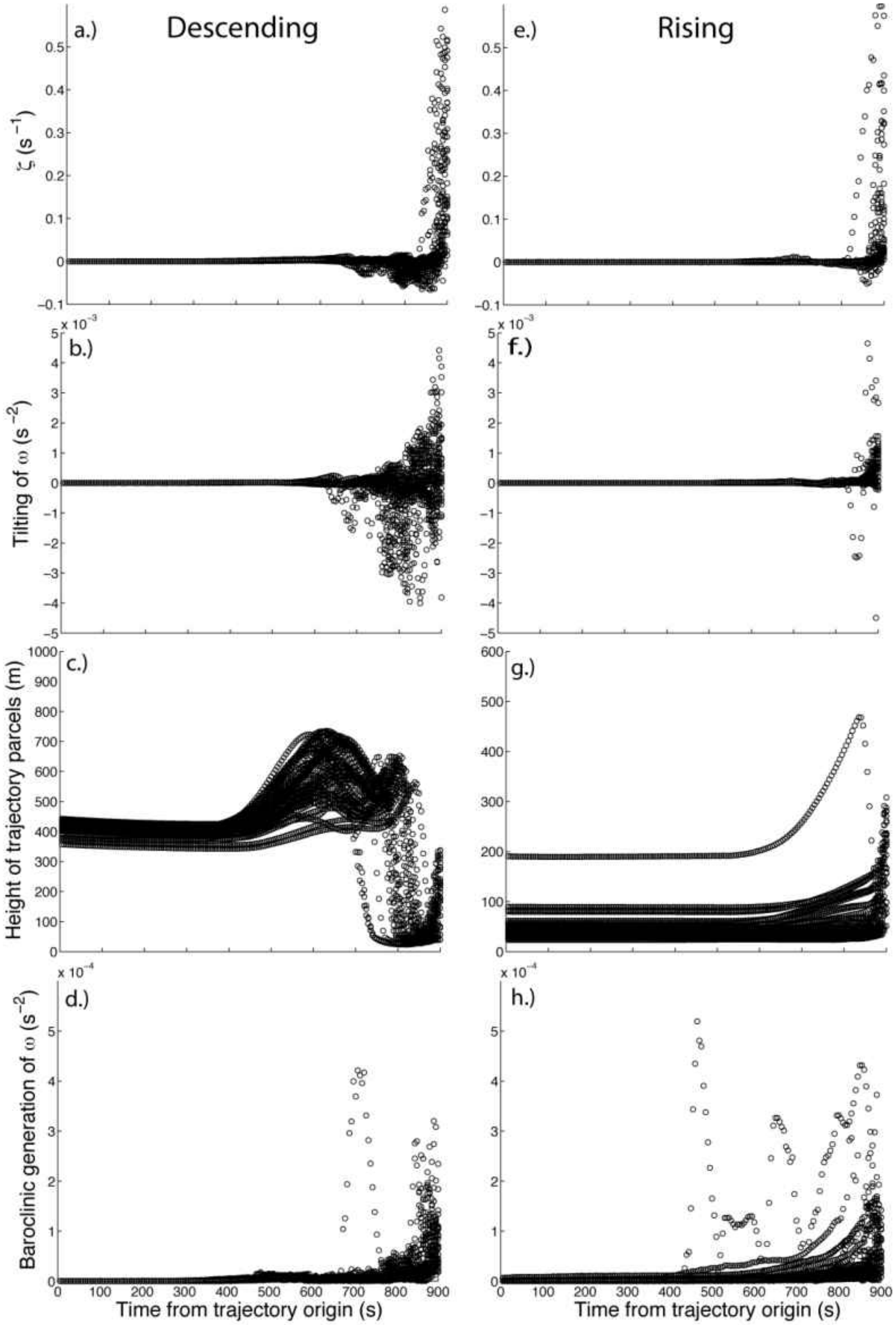

Figure 6.13. Time tendencies of vertical vorticity (a,e), tilting (b,f), parcel height (c,g) and baroclinic generation of horizontal vorticity (d,h) in case 12. Descending parcels are shown in the left column and rising parcels in the right column. Note that only the streamwise component of baroclinic horizontal vorticity generation is shown in h.

Case 5

In this case, less than 10% of the trajectories were from the rising category, so the contribution of these parcels to the total vorticity budget is considered negligible and they are not considered in the analysis of this case. Fig. 6.14 shows that there are two primary groupings of the descending parcels. One group consists of parcels that originate to the south of the main updraft and wrap cyclonically around the north side of the updraft before descending on the western updraft edge. The second group of parcels originates more to the east of the updraft and experiences some upward motion before descending to the surface. A few of the descending parcels gain positive ζ early on, although most do not until after t=700 s (Fig. 6.15a). As was the case in the previous two examples, many of the descending parcels experience both positive and negative tilting (Fig. 6.15b) with most of the positive stretching occurring shortly before or after the parcels reach the surface (Fig. 6.15c, Fig. 6.16c). Also similar to the previous cases is that descending motion produces negative tilting (Fig. 6.16b,c) and positive tilting becomes large only after parcels reach the surface, where baroclinic generation also becomes large (Fig. 6.16d).

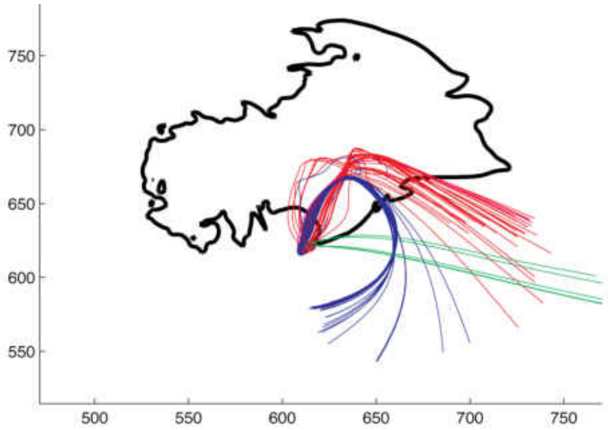

Figure 6.14. Overview of case 5. The thick black line is the 30 dBZ contour of simulated radar reflectivity. Air parcel trajectory paths are shown by the thin colored lines. The colors are the same as those shown in Fig. 6.2.

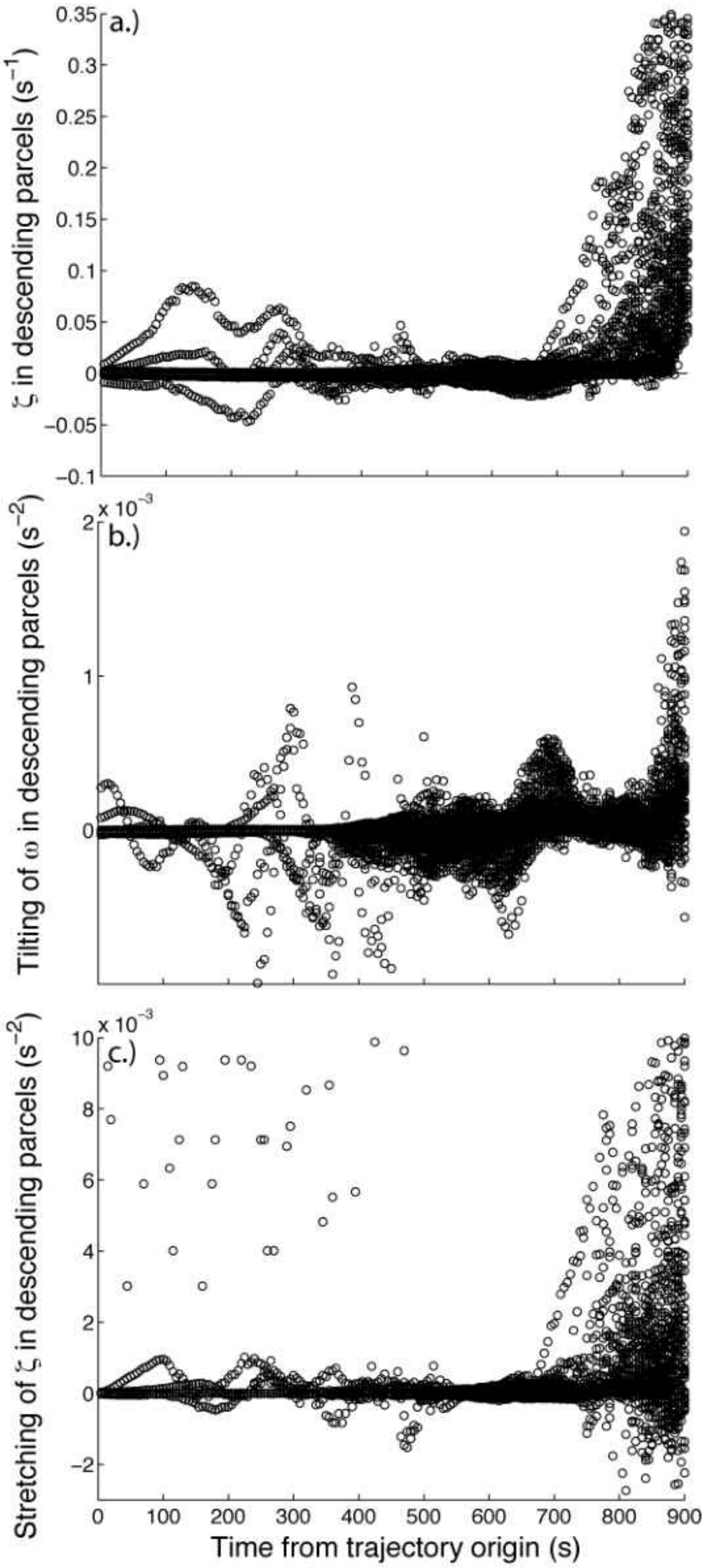

Figure 6.15. Vertical vorticity production vs. time for the descending parcels in case 5.

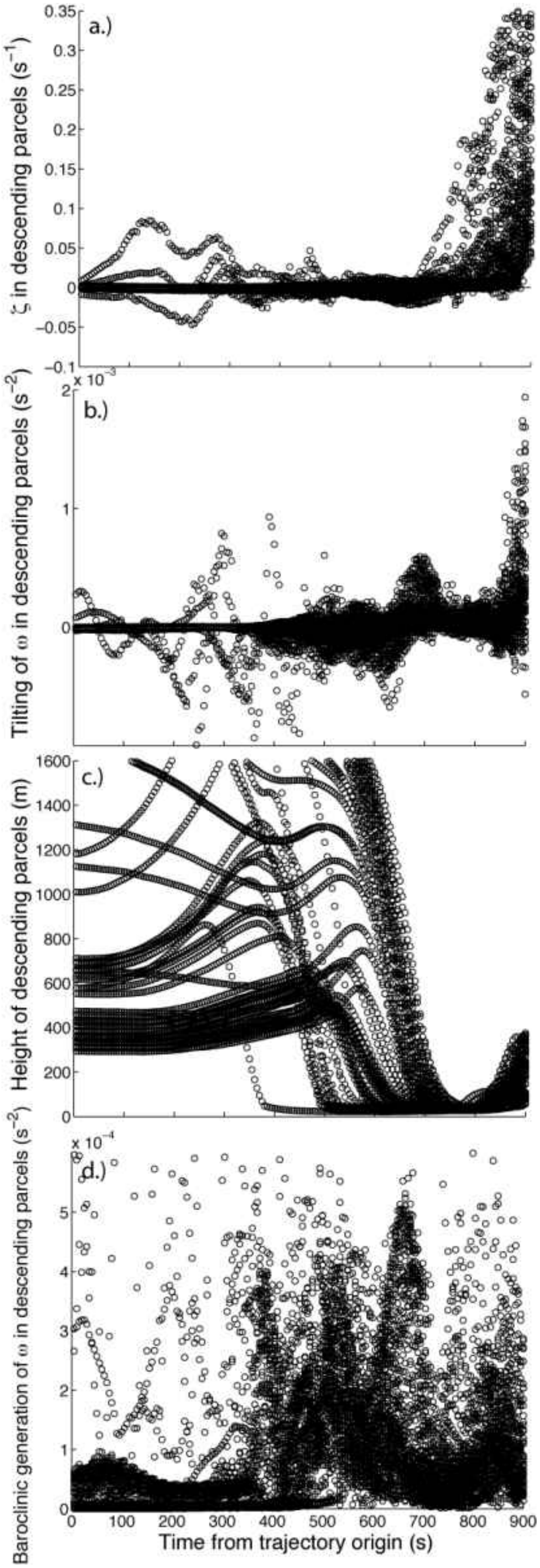

Figure 6.16. Time tendencies of vertical vorticity (a), tilting (b), parcel height (c) and baroclinic generation of horizontal vorticity (d) in case 5.

Case 17

This case differs from the previous three example cases since all of the parcels entering the tornadic circulation are from the rising group (Fig. 6.17). Although all parcels are from the same trajectory category, there appears to be three different source regions for these parcels. One group of parcels approaches the tornadic circulation from the north-northeast. Another group approaches from the east-northeast, and the third group approaches from the southeast. Note that, although the tornadic circulation itself seems to be somewhat separated from the main precipitation region, it is coincident with the midlevel mesocyclone (not shown).

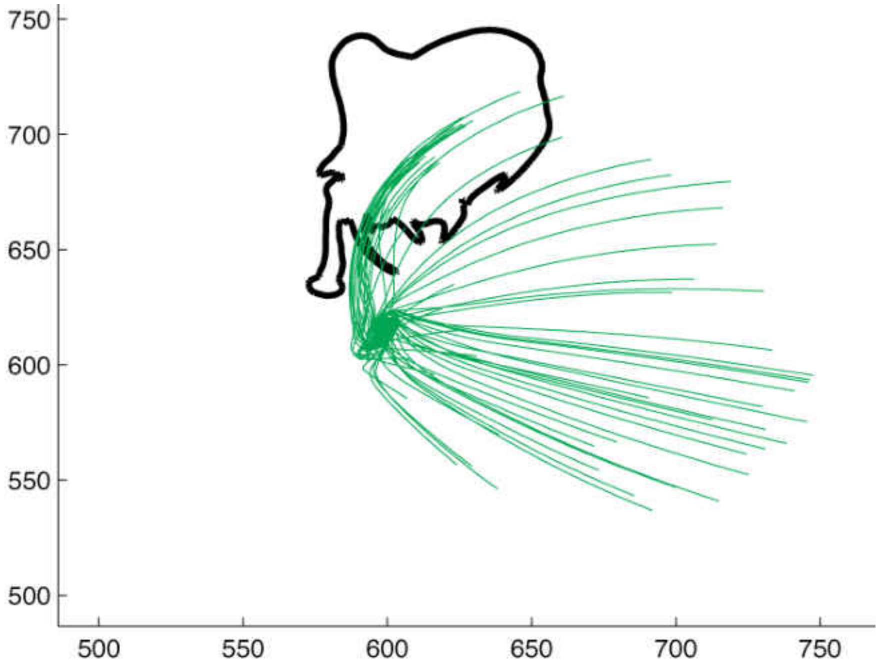

Figure 6.17. Overview of case 17. The thick black line is the 30 dBZ contour of simulated radar reflectivity. Air parcel trajectory paths are shown by the thin colored lines. The colors are the same as those shown in Fig. 6.2.

Vertical vorticity along the trajectories begins increasing shortly after *t*=300 s. (Fig. 6.18a). This increase in ζ corresponds to positive stretching (Fig. 6.18c), but not to positive tilting (Fig. 6.18b). In fact, there is near zero tilting along the trajectories prior to

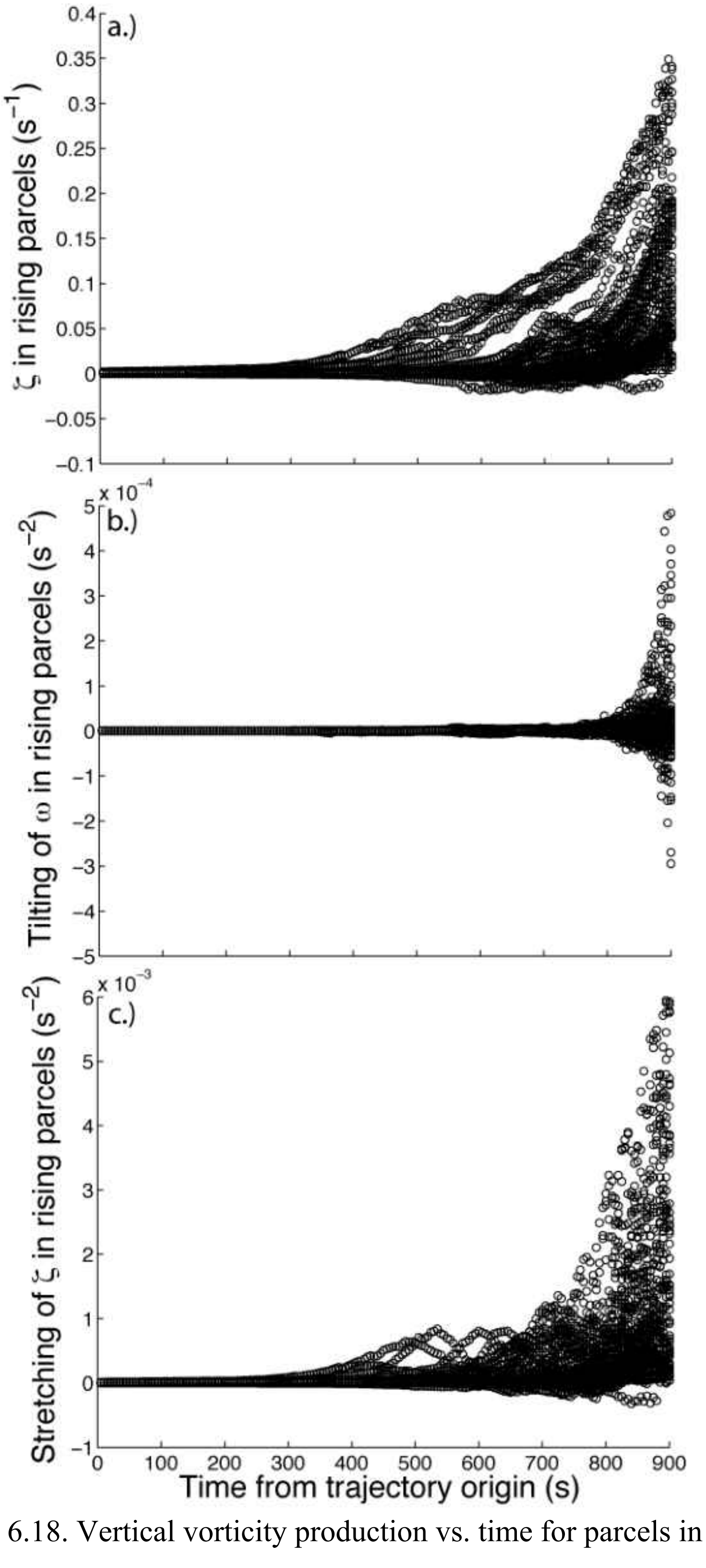

Figure 6.18. Vertical vorticity production vs. time for parcels in case 17.

the development of positive ζ at t=400 s. In addition, the parcels do not have any vertical motion when ζ first begins increasing (Fig. 6.19c) and there is little baroclinic generation of horizontal vorticity along the trajectories (Fig. 6.19d). The question then is where did the vertical vorticity come from if not from the tilting of horizontal vorticity? As mentioned earlier in this chapter, equation (6.1) is derived using the Boussinesq approximation, which ignores horizontal gradients in density. If the Boussinesq approximation is not applied, then (6.1) is written as

$$\frac{D\zeta}{Dt} = tilting + stretching + \frac{1}{\rho^2}\left(\frac{\partial \rho}{\partial x}\frac{\partial p}{\partial y} - \frac{\partial \rho}{\partial y}\frac{\partial p}{\partial x}\right), \tag{6.3}$$

where the first two terms on the RHS are the same is in (6.1) and the third term represents the solenoidal generation of ζ via horizontal density gradients. This term is generally ignored because it is believed to be several orders of magnitude smaller than the tilting and stretching terms.

Fig 6.20a shows that solenoidal generation of ζ is strongest in a narrow band to the north-northeast of the tornadic circulation. With maximum values of approximately 1.4 x 10^{-5} s^{-2}, solenoidal generation is two orders of magnitude smaller than the tilting and stretching terms in the example cases shown in this chapter, but one order of magnitude greater than the tilting occurring before t=700 s in this case (Fig. 6.18b). The area of maximum solenoidal generation occurs in a narrow line over 2 km in length. Many of the trajectories followed a path parallel to this zone, and may have traveled through it for an extended period of time (see Fig. 6.17). In addition, solenoidal generation is co-located with a region of vertical acceleration (Fig. 6.20b). Referring back to Fig. 6.18a, ζ increases between t=300 s and t=400 s by approximately 0.01 s^{-1}.

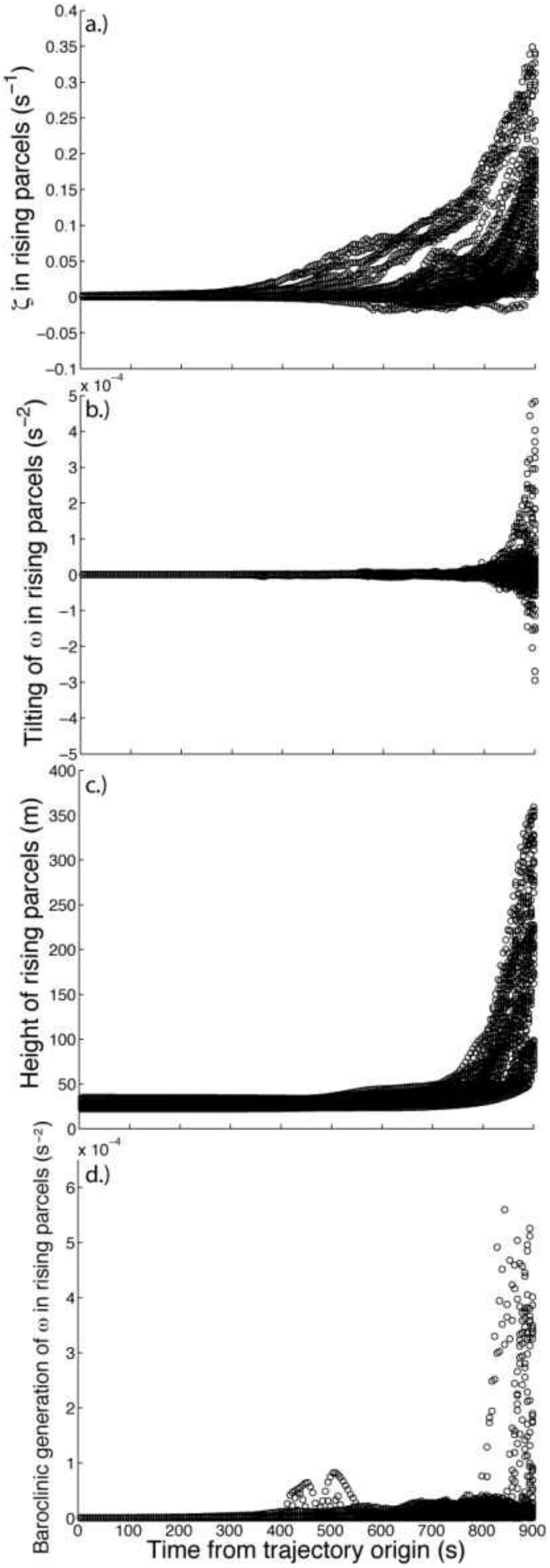

Figure 6.19. Time tendencies of vertical vorticity (a), tilting (b), parcel height (c) and streamwise baroclinic generation of horizontal vorticity (d) in case 17.

Assuming that the trajectories traveled through the solenoidal generation zone for 100 s between t=300 and t=400 s, and experienced solenoidal generation on the order of $1\text{x}10^{-5}\ \text{s}^{-2}$ and $\frac{\partial w}{\partial z}$ is on the order of 0.03 s^{-1}, then ζ would still be several orders of magnitude smaller than that shown in Fig. 6.18a.

Thus, the source of ζ in this case is inconclusive. It should be noted that the tornado in this case—along with the other case that was composed entirely of rising parcels (case 7)—occurred only about 5 min after updraft nudging was disabled. These were the two earliest occurring tornadoes in the dataset. Most of the remaining tornadoes occurred more than 20 min or more after nudging was disabled and all occurred at least 10 min after nudging was disabled. It is possible that during the updraft nudging process, some vertical vorticity was created due to the intense updraft acceleration at low levels. In fact, the mean ζ at the beginning of the trajectory path (model time of t=360 s) is $5\text{x}10^{-4}\ \text{s}^{-1}$. However, the presence of non-zero initial ζ alone does not explain tornadogenesis, as the mean initial ζ in this case is the same order of magnitude as in many other cases. Perhaps in this case the initial ζ, possibly created by the updraft nudging technique, was later stretched as the parcels traveled through the area of strong $\frac{\partial w}{\partial z}$ shown in Fig. 6.20b. More work is needed to determine if (and how) updraft nudging affected tornadogenesis in the simulations—particularly the two cases composed entirely of rising trajectories.

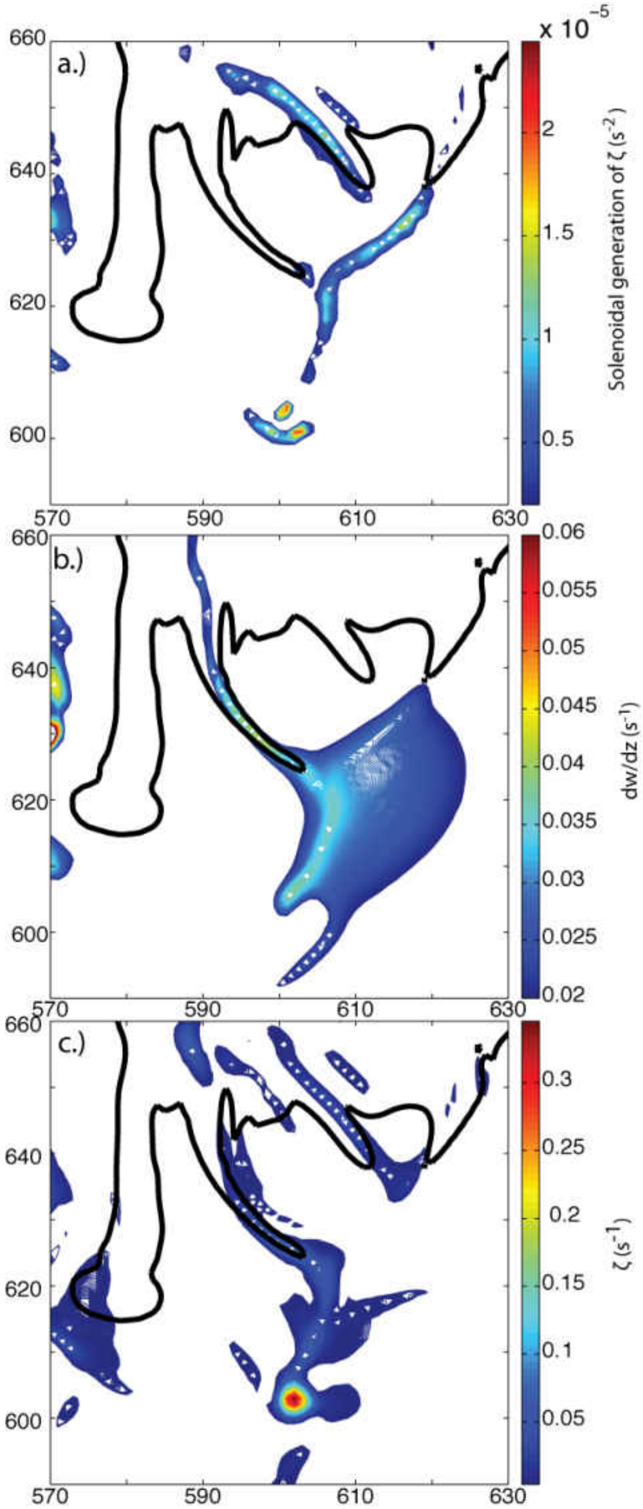

Figure 6.20. Vertical vorticity generation in case 17 at the time of tornadogenesis (*t*=1260 s). (a.) solenoidal generation of vertical vorticity, (b) change in vertical velocity with height (component of stretching term) and (c) vertical vorticity. The tornado is located at x=603 and y=602.

Summary of Relevant Processes

The case studies examined in this chapter have many similarities (with the exception of case 17; discussed in previous section). Descending parcels produce large, positive vertical vorticity only after descending to the surface. During the descent, the parcels mainly experience negative tilting resulting in negative vertical vorticity, with some positive tilting occurring when the parcels are just above the surface. As the parcels approach the surface from above, $\frac{\partial w}{\partial z}$ becomes negative and stretching becomes positive—reducing the magnitude of ζ regardless of sign. Once the parcels reach the surface, baroclinic generation of horizontal vorticity becomes large. Coincident with baroclinic generation is positive tilting and upward motion. In contrast, in the rising parcels, tilting is small while the parcels travel horizontally and becomes large only once the parcels begin to ascend.

All trajectories in all cases were examined to determine if these findings apply to all cases. The parcels were grouped into quadrants, based on the sign of vertical velocity and the sign of the production term being analyzed. In the rising trajectory parcels, the majority of the positive tilting is associated with rising motion (Fig. 6.21). While the total number of instances of positive tilting associated with updrafts (42 596) is similar to the total instances of negative tilting in updrafts (38 995), the positive tilting is, on average, an order of magnitude larger than the negative tilting associated with updrafts (6.02×10^{5} s^{-2} vs. 6.89×10^{6} s^{-2}). In downdrafts, positive tilting and negative tilting are similar in both magnitude (2.99×10^{-5} s^{-2} vs. 2.43×10^{-5} s^{-2}) and total number of instances (21 277 vs. 16 614). Thus, positive tilting is stronger and more frequent when associated with updrafts as opposed to downdrafts—in agreement with the findings from the example cases.

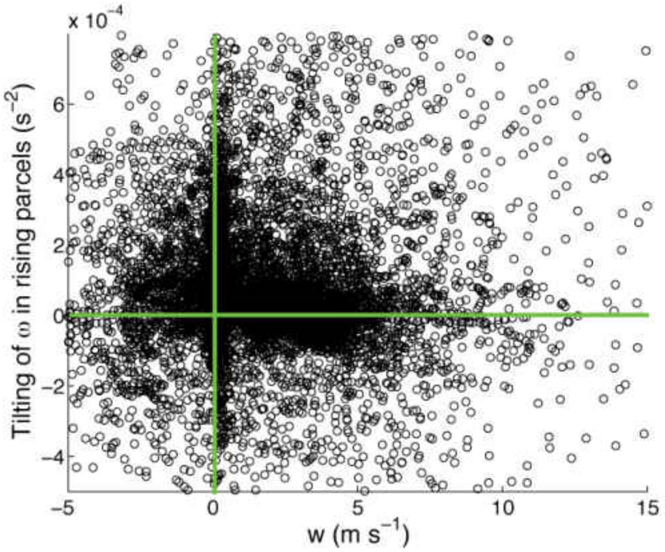

Figure 6.21. Tilting vs. vertical velocity for all rising parcels in all cases at all times. The green lines denote zero values for tilting and vertical velocity.

In the descending parcels, more than half of the points associated with downdrafts produce some negative tilting (69 151 negative tilting vs. 60 468 positive tilting; Fig. 6.22a). However, the negative tilting is weaker on average compared to the positive tilting produced in downdrafts (1.84 x10^{-4} s^{-2} vs. 2.58x10^{-4} s^{-2}). Positive tilting is slightly stronger (on average) when it is associated with updrafts as opposed to downdrafts (3.56 x 10^{-4} s^{-2} vs. 2.58 x 10^{-4} s^{-2}), but occurs more frequently in downdrafts (45 828 vs. 60 468). These findings agree with the results from the case studies: negative tilting is more common in downdrafts than positive tilting, and positive tilting has larger magnitude in updrafts than downdrafts. Most of the large magnitude tilting occurred below *z*=1 km (Fig. 6.22c), with much of the negative tilting occurring slightly higher above ground than the positive tilting. The majority of large positive tilting occurred below z=500 m—also in agreement with the example cases. Stretching of vertical vorticity is largest when coincident with updraft, with a mean value of 1.2 x 10^{-3} s^{-2} (Fig. 6.22b). The mean negative stretching coincident with updraft is two orders of magnitude smaller than the positive stretching. In downdrafts, negative stretching was more common and larger in magnitude than positive stretching. Larger magnitude stretching should be expected in downdrafts (as opposed to updrafts) at low levels since the vertical acceleration in this region will be stronger in downdrafts.

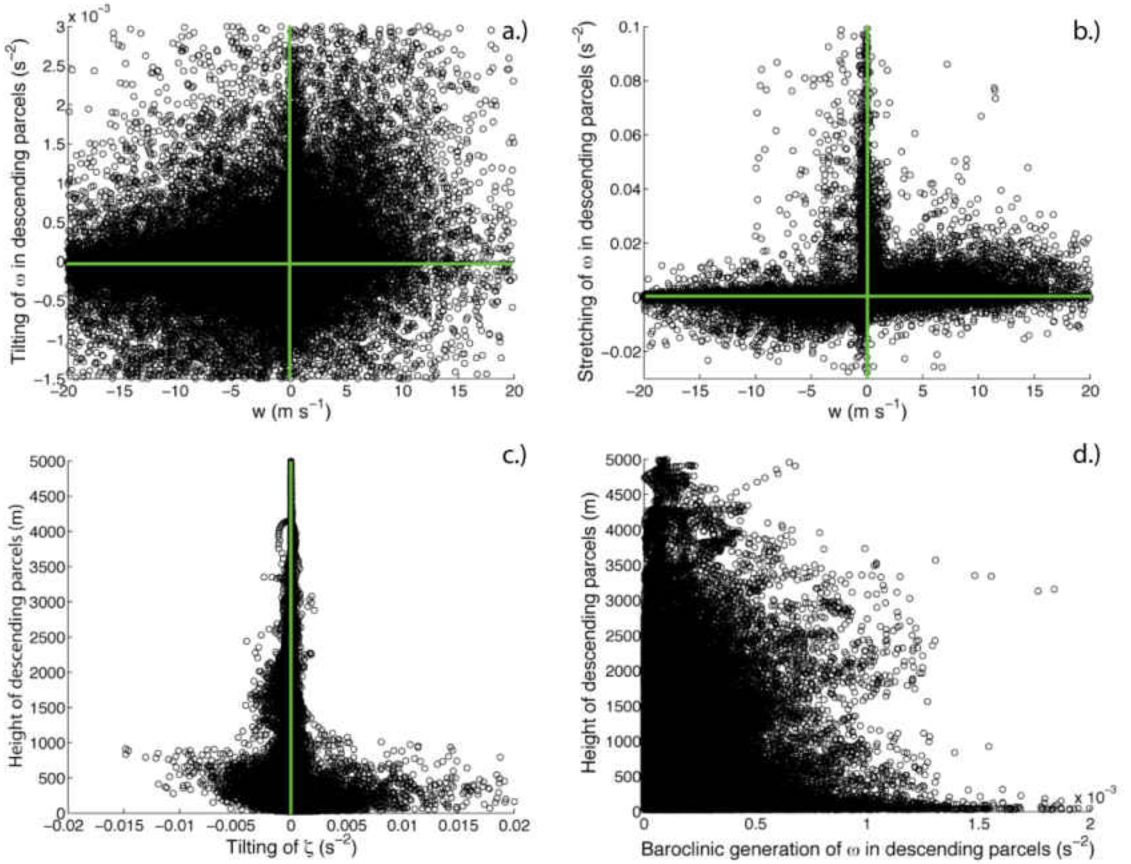

Figure 6.22. Comparison of vertical vorticity production via (a) tilting and (b) stretching vs. vertical velocity as well as height vs. (c) tilting and (d) baroclinic generation of horizontal vorticity for all descending trajectory parcels in all cases at all times. Green lines denote zero values for tilting and vertical velocity.

Fig. 6.22d shows that the largest values of baroclinic ω generation occurred below z=500 m, corresponding to the height of maximum tilting. However, relatively large baroclinic generation also occurred at heights well above this. In the example cases presented earlier, it was implied that the tilting of baroclinically generated horizontal vorticity helped to convert the negative ζ generated during descent to positive values. In agreement with this statement, Fig 6.23 shows that the smallest values of ζ correspond to the smallest values of baroclinic generation. As ζ increases to zero, baroclinic generation also increases. When ζ is greater than zero, there is an inverse relationship with baroclinic generation, possibly since baroclinic generation decreases as parcels rise towards the tornado.

Further evidence of the importance of baroclinic generation in descending parcels is found by examining the initial environment of the cases. In all but three cases, total baroclinic generation in descending parcels is at least four times larger than barotropic vorticity (computed from z=0-1 km) (Fig. 6.24). Two of these cases (7 and 17) did not have any descending trajectories and the third (case 11) was discussed above. Additionally, if tilting of barotropic horizontal vorticity were the dominate mechanism for the production of ζ, it would seem reasonable that net tilting in descending parcels would be larger given larger values of barotropic vorticity. However, this is not the case. Figure 6.25 shows that 0-1 storm relative environmental helicity—which is proportional to barotropic vorticity—does not have a strong relationship with tilting in descending parcels.

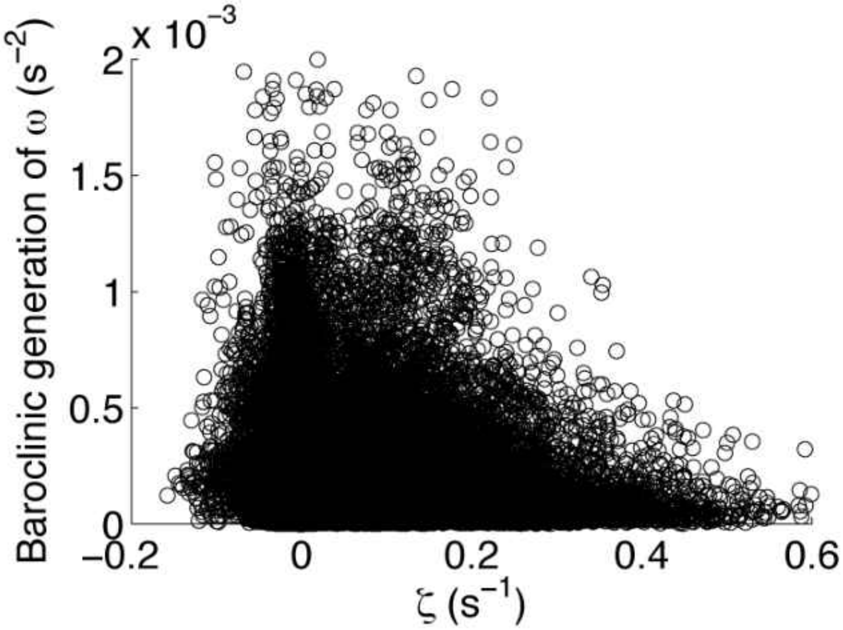

Figure 6.23. Scatterplot of vertical vorticity vs. baroclinic generation of horizontal vorticity at all points along all trajectories in all cases.

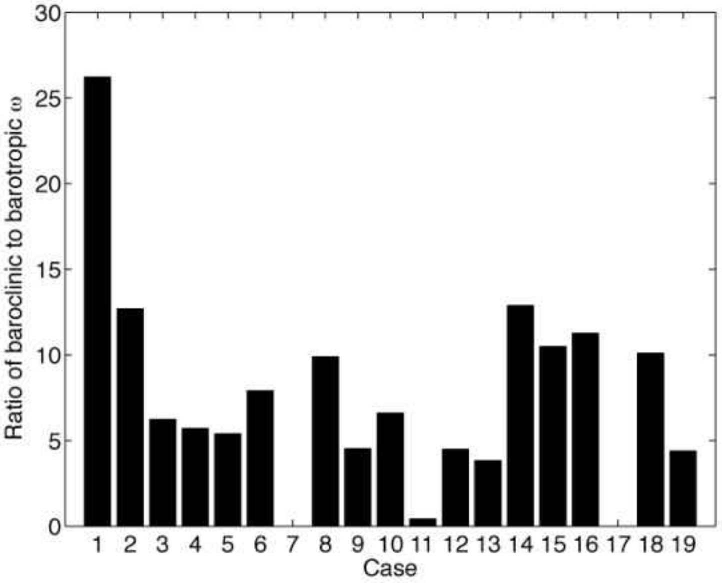

Figure 6.24. Ratio of baroclinic generation of horizontal vorticity in descending parcels to barotropic vorticity for all tornadic cases. Barotropic vorticity is calculated over the lowest 1 km depth.

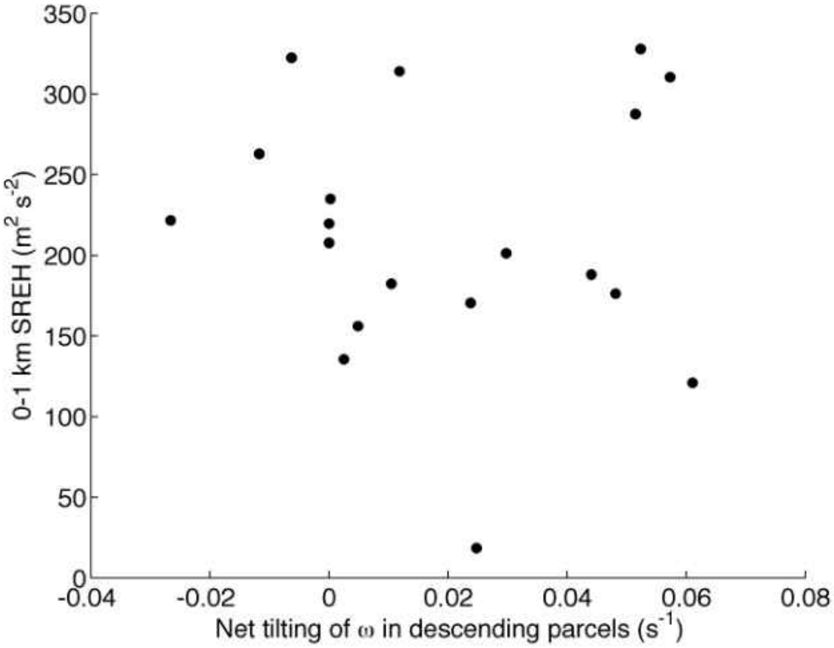

Figure 6.25. Scatterplot of 0-1 km storm relative environmental helicity (SREH) vs. average net tilting in descending parcels for each case.

Summary and Conclusions

In this chapter, the processes responsible for the generation of tornado-like vortices were analyzed with the aid of backwards-integrated trajectories. The trajectories were classified based on trajectory origin height and path taken to the tornadic circulation. Two primary categories were found: rising parcels, which typically originate near the surface and steadily rise towards the tornado; and descending parcels, which, at some point in their path, descend from aloft to the surface.

There were only two cases that did not contain any descending trajectories, and the validity of those two cases has been questioned (see ‘case 17’ section). All other cases contained both rising and descending parcels, although the number of trajectories from each category varied by case. In addition to comparing the trajectories from all cases, several cases were examined in detail. The following results were found:

- Of the nineteen cases analyzed, thirteen (68%) contained substantially more descending parcels than rising parcels. Only four cases had more rising than descending, and two cases had a nearly equal number of both.
- Rising parcels produced positive vertical vorticity primarily through the tilting of horizontal vorticity that occurred during ascent. The production of vertical vorticity generally proceeded baroclinic production of horizontal vorticity. Negative vorticity production along these trajectories was negligible compared to positive vorticity production.
- Descending parcels did not produce large, positive values of vertical vorticity until after they reached the surface. In many parcels, negative vertical vorticity developed during their descent.
- In descending parcels, positive tilting of horizontal vorticity and the development of positive vertical vorticity mainly occurred below z=500 m and often occurred in conjunction with the baroclinic generation of horizontal vorticity. In many of the descending parcels, negative vertical vorticity and negative tilting were present during their descent. The overall magnitude of tilting production was larger in descending parcels than in rising parcels.
- The net baroclinic generation of horizontal vorticity in descending parcels (determined for each case by integrating over trajectory path and averaging over all trajectories in that case) was larger than environmental barotropic vorticity in almost every case.

These results suggest that baroclinically-generated vorticity in rising parcels could be an important source of vorticity that results in tornadogenesis, since it occurs just before the generation of vertical vorticity via tilting in both the rising and descending parcels. However, it is unclear from the analysis exactly how much of the vorticity in the tornado was produced barotropically or baroclinically. In rising parcels, streamwise baroclinic horizontal vorticity is generated as the parcels flow along a horizontal density gradient. As the parcels ascend, this vorticity is tilted into the vertical and later intensified by stretching. In descending parcels, baroclinic vorticity appears to help 'dampen' negative vertical vorticity that is generated as the parcels descend. The tilting of baroclinically generated horizontal vorticity appears to be strongest at heights of approximately 500 m or less.

CHAPTER 7

COMPARISON OF VORTICITY PRODUCTION IN TORNADIC AND NONTORNADIC SIMULATED SUPERCELLS

While many studies have examined the structure and behavior of tornadic supercells, there has been relatively little focus on nontornadic supercells. Much of the research involving nontornadic storms has only focused on understanding differences in the *environments* of tornadic and nontornadic storms [e.g. Darkow 1969; Maddox 1976; Davies and Johns 1993; Brooks et al. 1994; Rasmussen and Blanchard 1998; Thompson et al. 2003,2012; Togstad et al. 2011]. Such research has led to great advancements in the current understanding of tornadic storms. For example, it is now known that tornadic supercells occur more often in environments with large values of storm relative environmental helicity and low LCL heights (Rasmussen and Blanchard 1998, Thompson et al. 2003). However, there are still many questions regarding the storm-scale differences between tornadic and nontornadic supercells.

Trapp (1999) compared six supercells (three nontornadic and three tornadic) observed during the Verification of the Origins of Rotation in Tornadoes Experiment (VORTEX) and found that the storms possessed many similar characteristics. The main difference was that the nontornadic supercells experienced less stretching of vertical vorticity and less low-level convergence. Using a similar dataset from VORTEX, Markowski et al. (2008) found that both tornadic and nontornadic storms have vortex line ‘arches’ that straddle the hook echo of the supercell and that the development of near-surface rotation in both types of supercells is aided by baroclinic vorticity generation in the rear flank downdraft. Wakimoto and Cai (2000) also found many similar characteristics in their comparison of the 2 May 1995 nontornadic supercell near Hays, KS and the 16 May 1996 Garden City, KS tornadic supercell, including the presence of an occlusion downdraft in both storms and a horseshoe-shaped updraft/downdraft signature at low-levels (both previously known to be present in tornadic supercells). The main differences between the two storms included stronger precipitation in the rear flank, stronger inflow, and stronger updrafts along the rear flank in the nontornadic supercell. Zeigler et al. (2001) concluded that the main difference between nearby tornadic and nontornadic supercells was that strong, low-level vertical vorticity stretching was present in the tornadic storm, while the nontornadic storm was characterized by negative stretching. However, they also note that low-level vertical vorticity intensification in the tornadic supercell may have been aided by a pre-existing vortex in the boundary layer.

Observational studies have also shown that the evaporatively-chilled storm outflow in significantly tornadic supercells often has smaller negative buoyancy (not too cold/dense) relative to the pre-storm environment compared to nontornadic supercells (e.g. Markowski et al. 2002, Shabbott et al. 2006, Grzych et al. 2007). Tornado simulations by Markowski et al. (2003) using a model with 2-D axisymmetric coordinate system (radius versus height) show that downdrafts that are excessively negatively buoyant cannot be lifted by the updraft, thus disrupting near-surface convergence and stretching of vertical vorticity. Markowski et al. (2011) computed trajectories in three nontornadic supercells (without surface thermodynamic data) and found that the air entering the near-surface circulation only ascends for a short distance, before abruptly descending again, whereas air parcels in tornadic circulations ascend to much higher altitudes. This is additional evidence that ascending parcels in nontornadic storms may generally have less buoyancy. Although small negative buoyancy in the storm outflow is easier to lift against gravity by the vertical pressure gradient in the low-level updraft, there is an implied tradeoff in reduced baroclinic generation for parcels flowing into the tornado along the forward flank of the storm. Thus, more low-level environmental wind shear (barotropic vorticity) may need to be present in such cases.

The purpose of this chapter is to compare the results of tornadic simulations (shown in the previous chapter) to nontornadic simulations and to determine important differences between these two supercell categories. The following questions are addressed:

- **What is the most likely tornadogenesis failure mechanism?** Is it more likely for nontornadic supercells to simply have less vorticity production than tornadic supercells, or for the nontornadic supercells to fail to achieve the near-surface balance necessary to lift and stretch the vorticity-rich air in/along the storm outflow?
- **What is the relative importance of baroclinic and barotropic vorticity?** Both processes are inevitably present in supercells. However, is one process (and source region) consistently dominant in the tornadic supercells while less influential in nontornadic supercells? Recall that tornadic near-storm environments have more SREH and barotropic vorticity than non-tornadic near-storm environments (e.g. Thompson et al. 2003). However, numerous studies have concluded that tornadogenesis resulted from the tilting of baroclinically generated horizontal

vorticity. It is hypothesized then that those tornadic supercells forming in environments with stronger barotropic vorticity will depend less upon baroclinic generation, while total vorticity production in the nontornadic cases will depend more on baroclinic generation.

Methodology

To compare with the nineteen tornadic simulations from the previous chapter, additional simulations were performed to develop a nontornadic set of simulations. All 454 nontornadic RUC-2 proximity soundings were simulated with the lower-resolution model configuration used in Chapters 3 and 4 (at 1 km horizontal resolution, 250 m vertical resolution with updraft nudging applied for the first 900 s of model time). Of these 454 simulations, 155 produced supercells lasting at least 1 hr in duration—determined using the updraft helicity threshold determined in Chapter 3. A subset of 40 of these cases was randomly selected for simulation using the model configuration from the previous two chapters (100 m spacing in the vertical and horizontal, 1 s large time step, and 2 hr run time).

Backward Integrated Trajectories

In the tornadic simulations, trajectories were seeded in the tornado, which was easily identifiable due to the large pressure drop associated with it. Such a large pressure drop is not always present in the low-level mesocyclones of nontornadic supercells. Thus, a different method seeding trajectories is needed for the nontornadic simulations.

The purpose of this analysis is to examine the low-level airflow in the nontornadic supercells at the time of tornadogenesis ‘failure’, which is assumed to occur when the near-surface mesocyclone is at maximum intensity. However, a widely accepted measure for mesocyclone intensity does not exist. Trapp (1999) simply used the time of peak vertical vorticity in the near-surface mesocyclone to denote the time of tornadogenesis failure. However, multiple circulation centers may occur along the leading gust front of the storm. Simply using the maximum value of vertical vorticity does not assure that the circulation is associated with a strong updraft. Markowski et al. (2011) used the minimum value of the Okubo-Weiss number to define the near-surface mesocyclone center. Small values of the Okubo-Weiss number are associated with decreased pressure, large vertical vorticity, and small deformation. The benefit of this technique seems to be ensuring that large vertical vorticity is coincident with a minimum in pressure.

This study uses a somewhat similar approach, except that the method used herein ensures that large vertical vorticity is coincident with updraft instead of a pressure drop, as was the case in Markowski et al. (2011). This is achieved by defining the near-surface mesocyclone as an area with large values of updraft helicity. In Chapter 3, updraft helicity was shown to successfully detect midlevel mesocyclones. Near-surface mesocyclones should be detectable by modifying the updraft helicity integration depth. Instead of the 2-5 km depth found to be optimal for midlevel mesocyclone detection in Chapter 3, near-surface mesocyclone detection uses updraft helicity integrated from 0-1 km. This method not only ensures that vertical vorticity and updraft are co-located, but that the co-location extends over a substantial depth, which should lessen the likelihood of detecting near-surface mesocyclones having significant vertical tilt (such as caused by a rapidly propagating gust front).

Thus, the time and location of maximum mesocyclone strength and tornadogenesis failure is based on the domain maximum value of 0-1 km updraft helicity.

A 1 km x 1 km box is then centered on this location, and trajectories are seeded at points inside this box having vertical vorticity greater than 0.05 s^{-1} between the same range of altitudes as in the tornadic cases: z=0-500 m. The box is defined such that it is large enough to encompass the primary circulation on the scale of a tornado (if one were to form), and the vorticity criteria is used to remove points that fall outside the primary circulation. As in Chapter 6, the trajectories are followed backwards in time for 900 s and vorticity production terms [see equations (6.1) and (6.2), Chapter 6] are calculated along the trajectories every 5 s.

Forward Integrated Trajectories

In both the tornadic and non-tornadic simulations, forward trajectories are also calculated to investigate the influence of outflow thermodynamics on tornadogenesis and tornadogenesis failure. Parcels residing in the tornado and/or near-surface mesocyclone were followed forward in time to observe the maximum vertical extent of these parcels. It is hypothesized that many of the non-tornadic supercells will be characterized by updrafts that are unable to lift these parcels until they become positively buoyant.

Forward trajectory calculations are the same as back trajectory calculations (every 1 s using history files generated every 5 s), except they are computed forward for 1200 s instead of backward for 900 s.

Results

Of the 40 nontornadic cases simulated at 100 m resolution, 24 produced supercells with a duration of 1 hr or more (determined based on combined subjective/objective approach used in Chapter 5). Of these, 14 were nontornadic and 10 were tornadic. Only the 14 nontornadic cases are considered for comparison with the 19 tornadic simulations from the previous chapter. An overview of the trajectory paths for these 14 cases is shown in Fig. 7.1. As was the case in the tornadic simulations in Chapter 6, the trajectories are categorized as simply ‘descending’ and ‘rising’. This means that three of the trajectory types shown in Figs 6.2 and 7.1 (blue, red, and magenta lines) are grouped into the “descending” category. The rising parcels generally originate at low levels, downshear of the near-surface mesocyclone, and move parallel to the forward flank gust front as they approach the circulation. The descending parcels typically approach the near-surface circulation from the north, often wrapping cyclonically around the north side of the midlevel mesocyclone. From Fig. 7.1, it is evident that the vast majority of the nontornadic mesocyclones are located at the edge of the strong reflectivity contour. Thus, it is unlikely that tornadogenesis failure occurred simply because the storms ‘gust out’. In fact, all cases remain a supercell for at least 20 min after the time of tornadogenesis failure.

In the previous chapter, it was shown that the rising parcels in the tornadic simulations (herein referred to as TOR) develop vertical vorticity as they rise towards the low-level circulation. Positive vertical vorticity generation initially occurs via tilting of horizontal vorticity, and is mainly coincident with rising motion. Many of these features are also apparent in the nontornadic simulations (herein NON). The (average) total ζ generation via tilting is very similar between the TOR and NON simulations (Fig. 7.2a), as is the baroclinic generation of streamwise horizontal vorticity (Fig. 7.2b), with streamwise generation being slightly larger in the NON simulations. The largest difference between the TOR and NON rising parcels is the stretching of vertical vorticity (Fig 7.2c). However, the largest differences in stretching occur at the very end of the

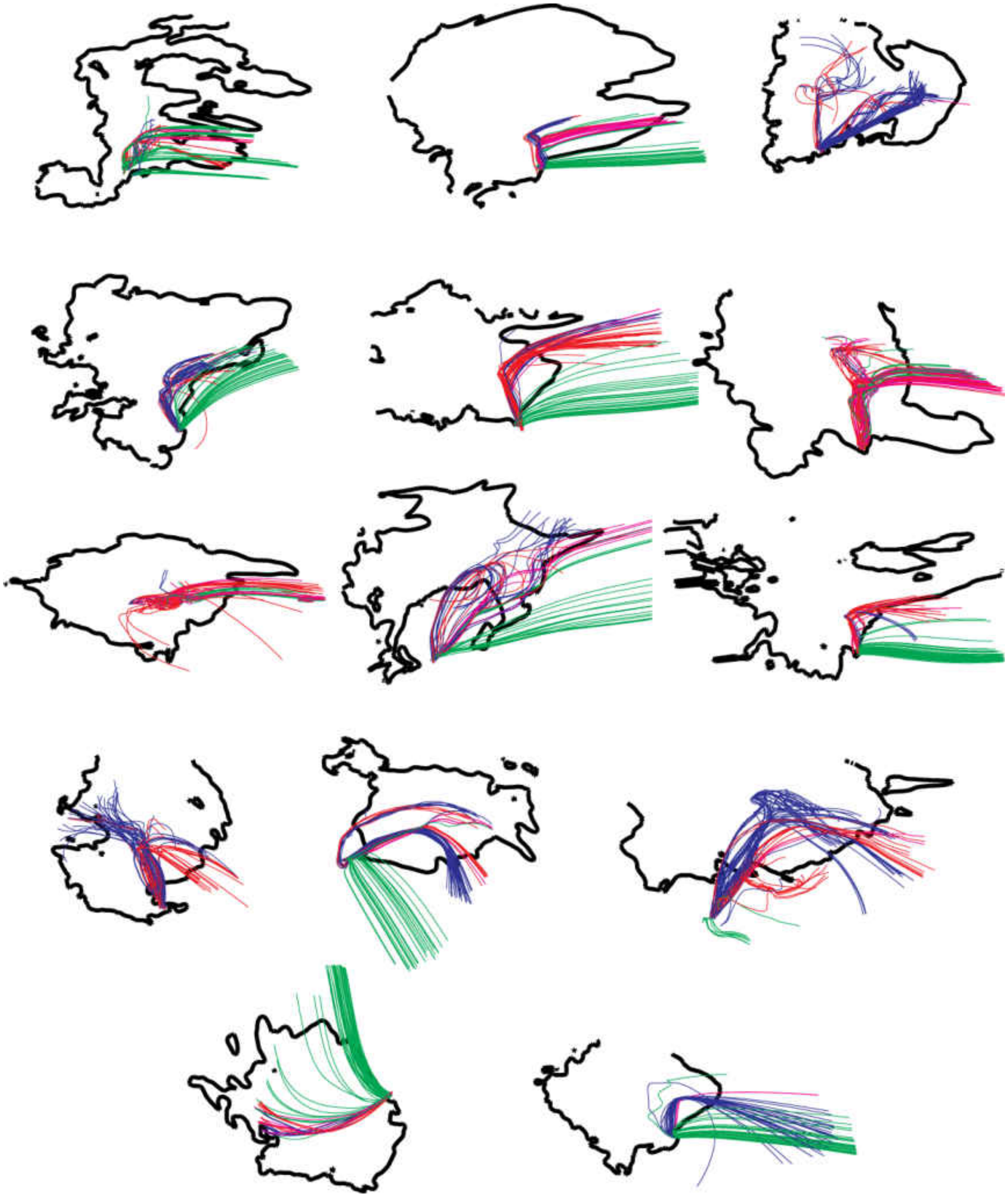

FIGURE 7.1: Overview of the nontornadic cases analyzed in this chapter. The thick black line is the 30 dBZ contour of simulated radar reflectivity. Air parcel trajectory paths are shown with the thin colored lines. The colors are the same as those shown in Fig. 6.2.

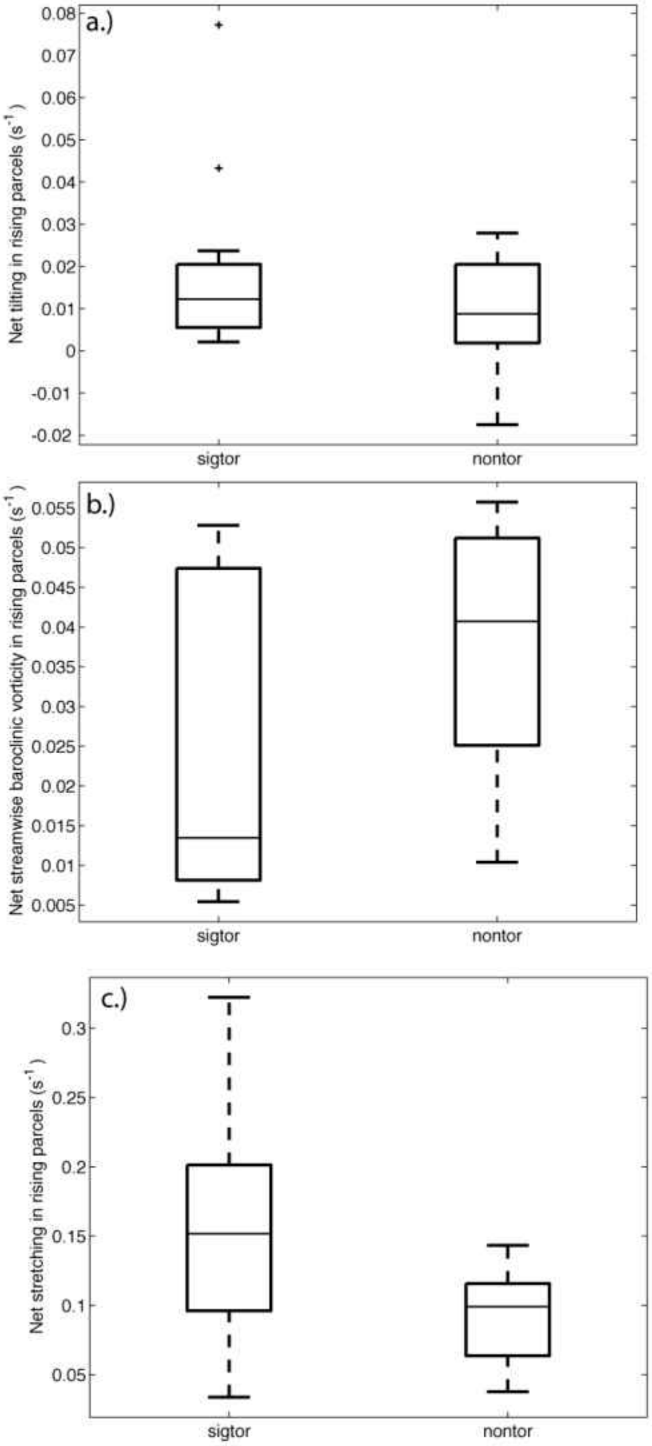

FIGURE 7.2. Net vorticity generation in the rising trajectory parcels of the TOR and NON simulations due to (a) tilting of horizontal vorticity, (b) streamwise baroclinic generation of horizontal vorticity and (c) stretching of vertical vorticity. Values are calculated (for one case) by integrating the vorticity production over the length of the trajectory and averaging over all rising trajectories in that case.

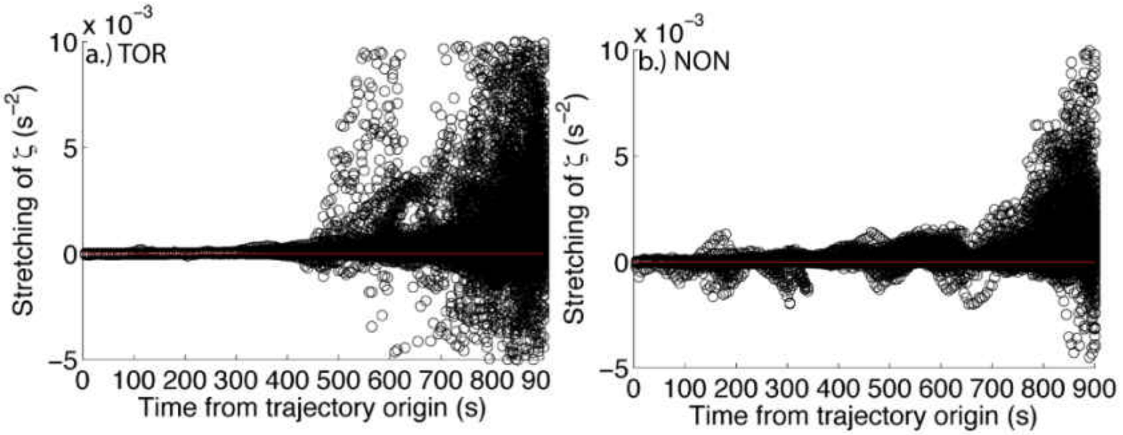

FIGURE 7.3. Comparison of vertical vorticity stretching in all cases, along all trajectories, at all times for the (a) TOR and (b) NON simulations.

trajectories, where the values are much greater in the TOR simulations (Fig. 7.3a,b). This is likely caused by the intense convergence in the tornado itself, and is probably not due to storm-scale differences in airflow. What is needed is an analysis of the vorticity evolution prior to reaching the incipient tornado.

Due to the similarities in the rising parcels, it does not appear that they play a role in determining if tornadogenesis or tornadogenesis failure occurs. In both the TOR and NON simulations, rising parcels contribute to the low-level circulation by tilting baroclinically generated horizontal vorticity and amplifying it via stretching. There are, however, some interesting differences in the descending parcels.

The descending parcels in the TOR simulations have larger average net tilting than those in the NON simulations (Fig. 7.4a). In the previous chapter, it was found that strong tilting in the descending TOR parcels often occurred in conjunction with increased baroclinic generation of horizontal vorticity. It was inferred that much of the baroclinically-generated vorticity was then tilted. However, the NON simulations have slightly larger (net) median baroclinic generation than the TOR cases (Fig 7.4b). Thus—as was the case in the rising parcels—larger net baroclinic generation of horizontal

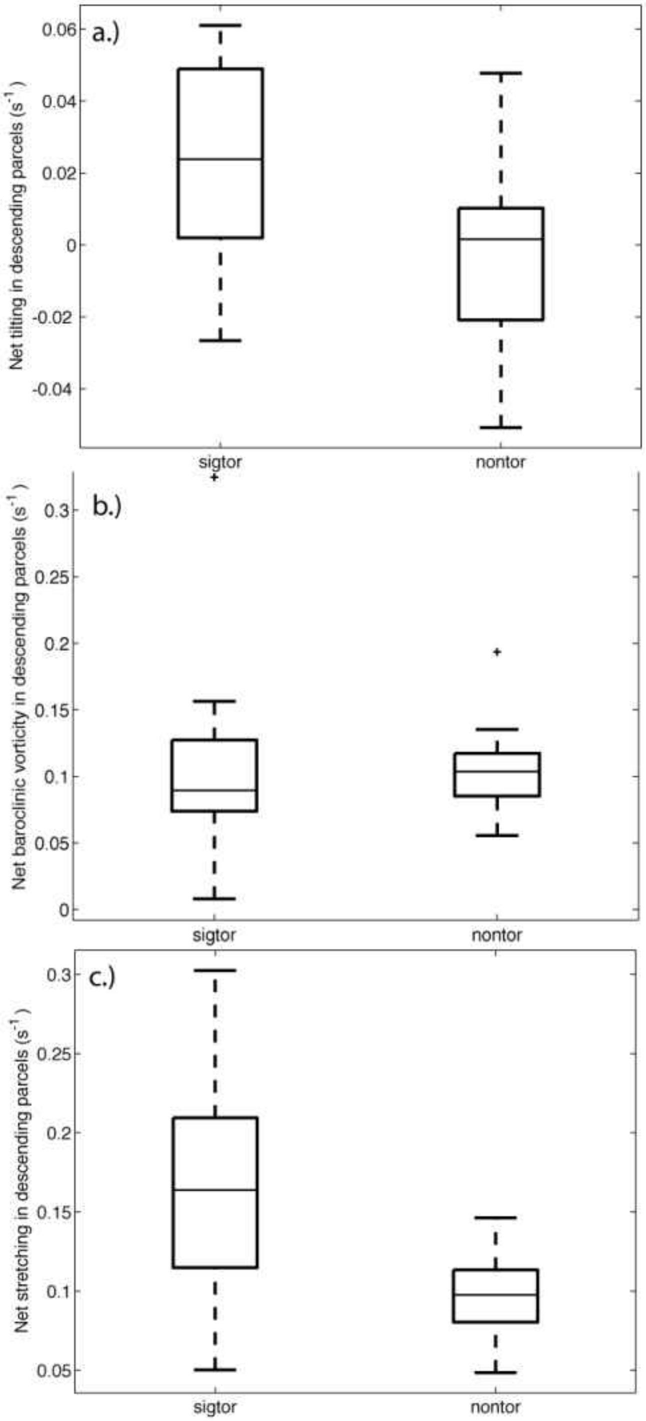

FIGURE 7.4. Net vorticity generation in the descending parcels of the TOR and NON simulations due to (a) tilting of horizontal vorticity, (b) baroclinic generation of horizontal vorticity and (c) stretching of vertical vorticity. Values are calculated (for one case) by integrating the vorticity production over the length of the trajectory and averaging over all descending trajectories in that case.

vorticity is not associated with net larger tilting of horizontal vorticity. As expected, stretching was also larger in the TOR simulations (Fig. 7.4c).

The large difference in tilting production between the TOR and NON simulations was further explored by analyzing tilting production to determine when (and where) the largest differences occurred (Fig. 7.5). During the first 500 s or so of the trajectories, there is not much difference between tilting in the TOR and NON simulations (Fig. 7.5a,b). After this time, the magnitude of the tilting in the TOR simulations becomes much larger. In particular, there is much more negative tilting in the TOR simulations. After 800 s or so, the differences between the TOR and NON simulations become even larger. However, towards the end of the TOR trajectories, large magnitude tilting could be caused by the strong vertical velocity gradients in the developing tornado.

Much of the large negative tilting in the TOR simulations is associated with downdrafts (Fig. 7.5c) and occurs below z=1 km (Fig. 7.5e). In the NON simulations, negative tilting in downdrafts appears to be much weaker (Fig. 7.5d,f). Additionally, the strong positive tilting below z=1 km in the TOR simulations is also absent in the NON simulations. Although Fig.7.5 illustrates significant differences in the behavior of descending parcels in the TOR and NON simulations, two important questions remain: (a) what processes are responsible for the stronger near-surface tilting in the TOR cases? and (b) is the stronger tilting the cause of tornado development or simply a product of it?

The tilting of horizontal vorticity is a function of the strength of the horizontal gradients of vertical velocity and the amount of horizontal vorticity in the atmosphere. An increase in either of these quantities leads to an increase in tilting. In both the TOR and NON simulations, the large low-level tilting below z=1 km (Figs. 7.5e,f) corresponds

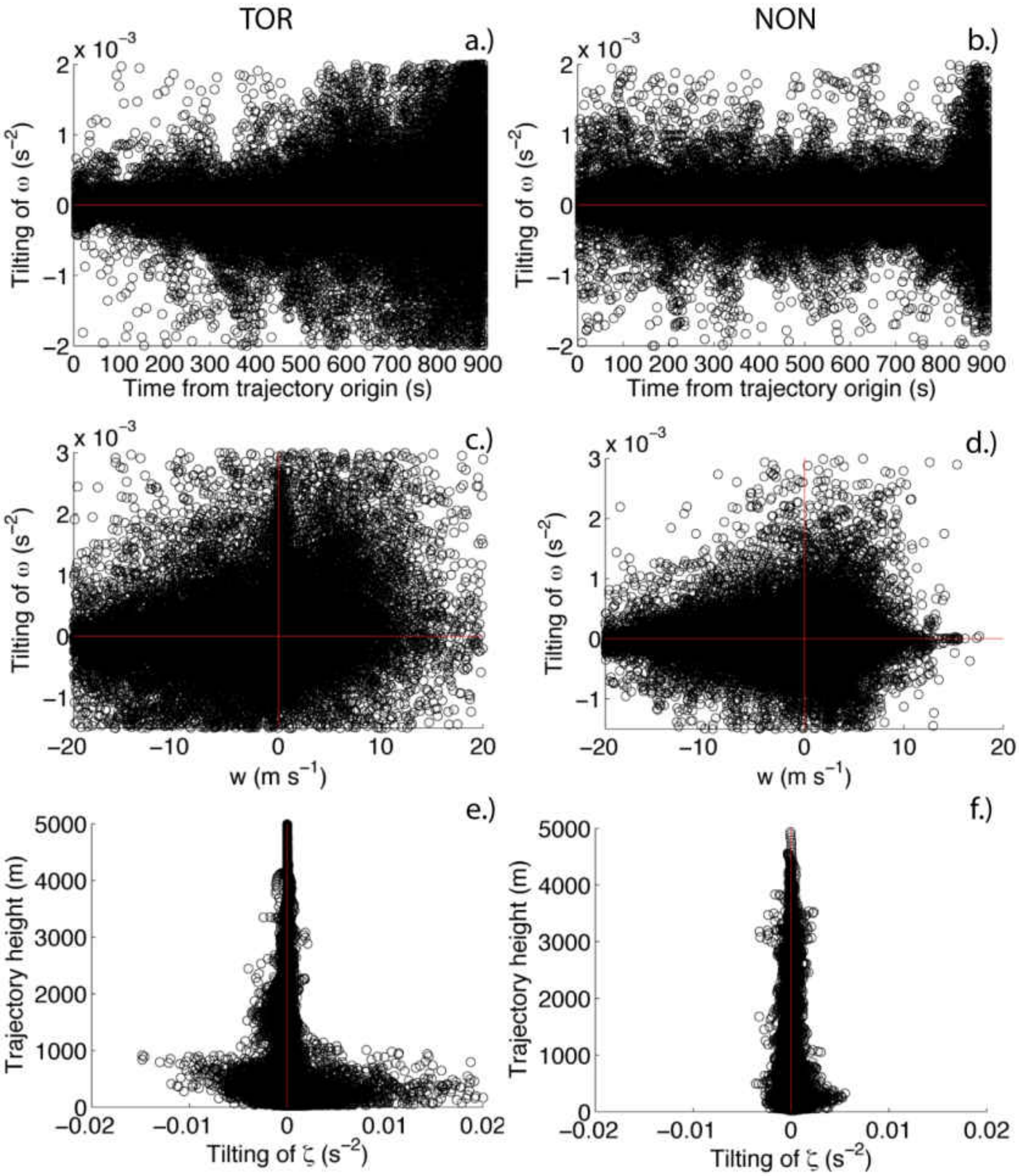

FIGURE 7.5. Vertical vorticity generation via the tilting of horizontal vorticity in the TOR and NON simulations as a function of (a-b) time, (c-d) vertical velocity, and (e-f) height.

to large values of horizontal vorticity (Fig. 7.6a,b), with the magnitude of this horizontal vorticity being much larger in the TOR simulations. The values of horizontal vorticity along the trajectories are similar in the TOR and NON simulations during the first few hundred seconds. However, this changes around *t*=500 s (400 s prior to trajectory initialization) when horizontal vorticity begins steadily increasing in the TOR simulations, while remaining relatively unchanged in the NON simulations. The second component of tilting—the horizontal gradient of vertical velocity—also shows a sharp increase below z=1 km in the TOR simulations (Fig. 7.7a) and relatively little increase in the NON simulations (Fig. 7.7b). This suggests that the strong low-level tilting in the TOR simulations (relative to NON) is a result of both larger horizontal vorticity and larger gradients of vertical velocity.

With the scatterplots shown in this chapter, it is difficult to determine the 'typical' behavior of a TOR or NON simulation. To better understand how differences in vorticity production between the TOR and NON simulations evolve with time, and to help identify the time period(s) along the trajectories where these differences are largest, a single composite trajectory was created for both the TOR and NON simulations. This was done by averaging all trajectories from all cases at each time step along the trajectories. However, this technique will 'smear' the data since the trajectories do not all follow the same path at the same time. Even with this limitation, substantial differences in the (average) vorticity production between the TOR and NON simulations are evident.

The TOR and NON composite trajectories are very similar for the first 500 s of trajectory time. Both generate weakly negative vertical vorticity between t=200 s and t=500 s (Fig. 7.8a) through negative tilting (Fig. 7.8b). After this time, vertical vorticity in the TOR composite sharply increases, while the NON trajectory remains fairly stagnant (Fig. 7.8a). This increase in vertical vorticity corresponds to positive tilting (Fig. 7.8b) and positive stretching (Fig. 7.8c). Around t=600 s, a fairly large difference in vertical vorticity between the TOR and NON composites has arisen due to a sudden spike in

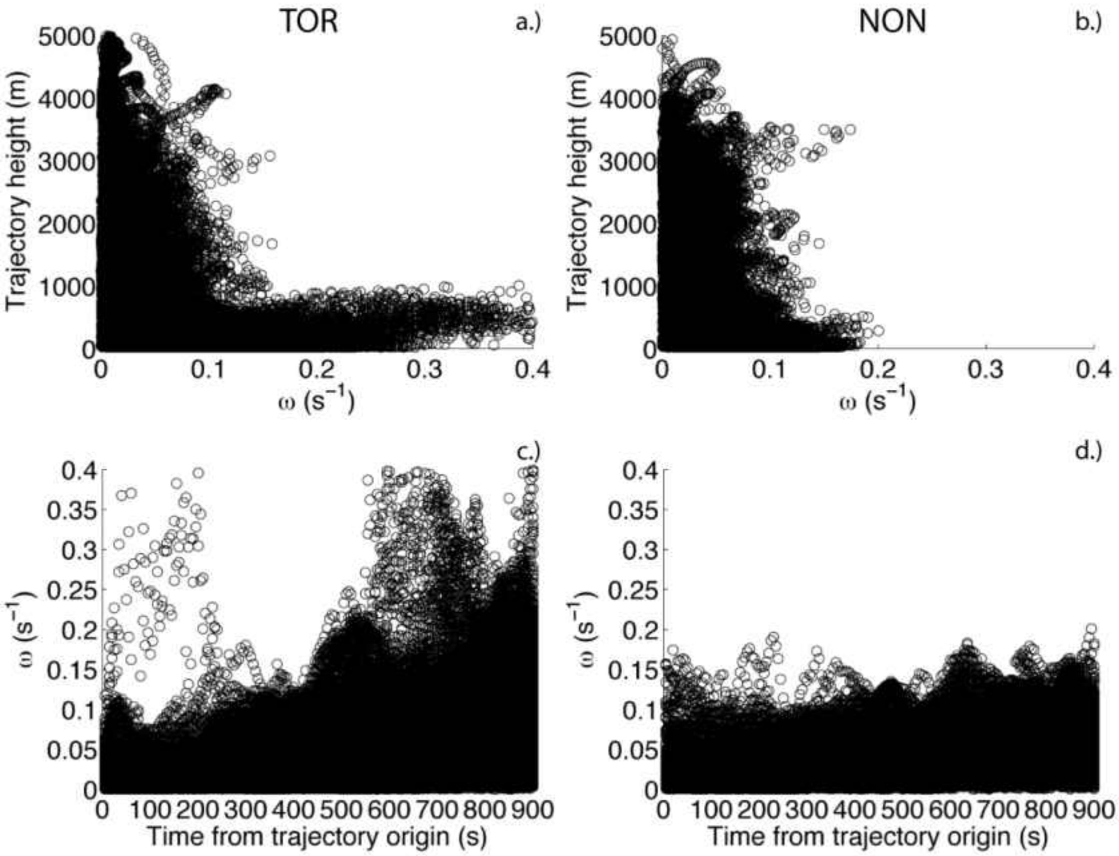

FIGURE 7.6. Magnitude of the horizontal vorticity vector in the TOR and NON simulations as a function of (a-b) height, and (c-d) time.

vertical vorticity in the TOR composite. Between *t*=600 s and *t*=800 s, the relative difference remains unchanged as vertical vorticity in the TOR composite quickly decreases, and both composite soundings experience a steady increase in vertical vorticity. Shortly after *t*=800 s, vertical vorticity in both composites increases sharply, with the increase in the TOR composite being substantially greater. Just before this sharp increase in vertical vorticity, there is relatively strong negative tilting occurring in the TOR composite (Fig. 7.8b) that is coincident with strong positive stretching (Fig. 7.8c). After *t*=800 s, vertical vorticity, tilting, and stretching all increase rapidly in the TOR composite as they near the developing tornado. The NON composite shows relatively large stretching and vertical vorticity as well, but tilting is very weak.

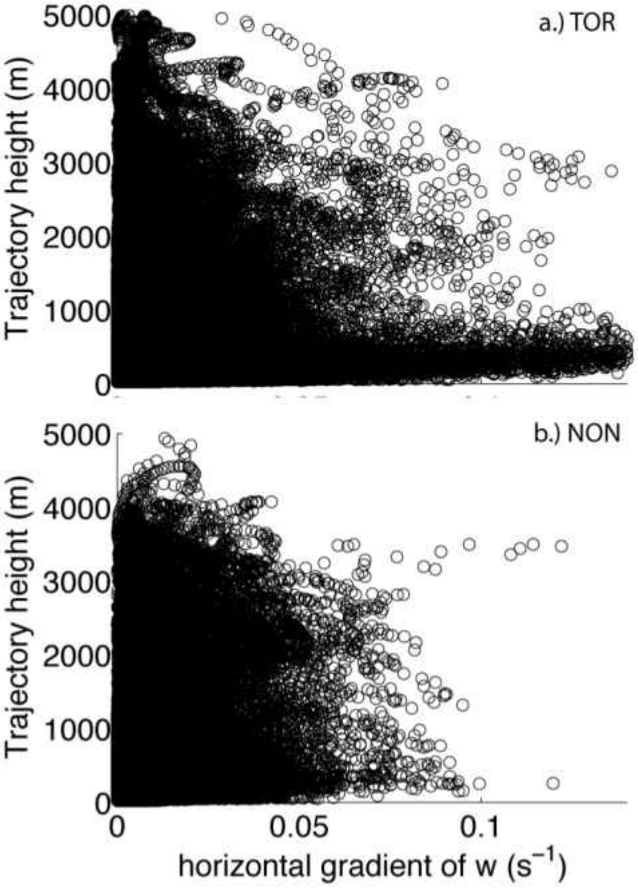

FIGURE 7.7. Horizontal gradient of vertical velocity vs. height for all trajectories in all (a) TOR and (b) NON simulations.

Figure 7.8 demonstrates that differences between the TOR and NON simulations are evident well before tornadogenesis (and tornadogenesis failure). Thus, the larger values of tilting and stretching in the TOR simulations discussed throughout this chapter are not simply a *result* of the tornadoes themselves, but appear to occur early enough that they are the *cause* of the tornadoes. However, because of the 'smearing' that results from downdraft trajectories arriving at the surface at different times in many of simulations (owing to initializing the trajectories at various heights in the tornado), it is difficult to tell what processes are most responsible for the differences shown in Fig. 7.8. To adjust for this, the individual trajectories were shifted forward or backward in time so that they

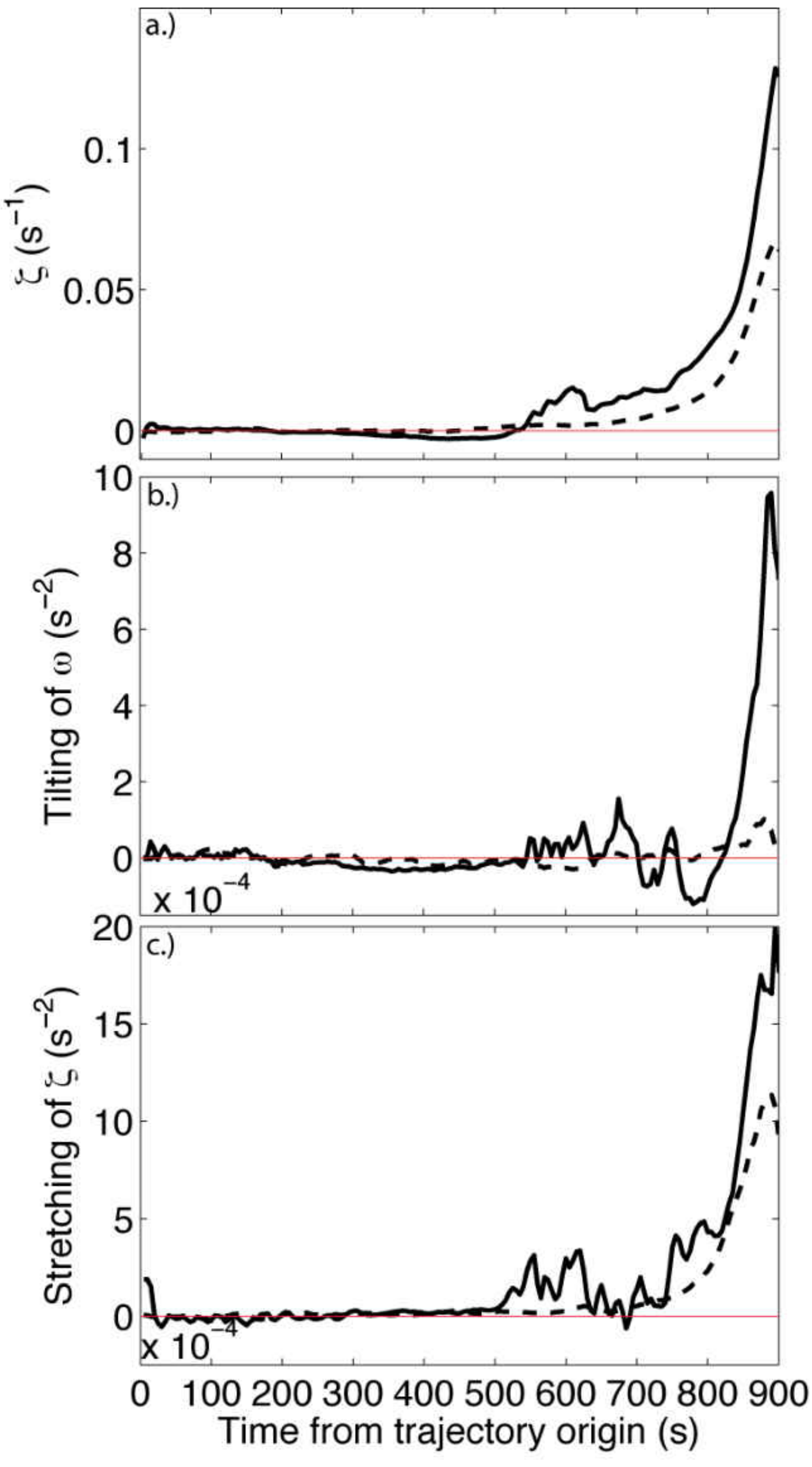

FIGURE 7.8. Composite trajectories for the TOR (solid line) and NON (dashed line) simulations showing (a) vertical vorticity, (b), tilting, and (c), stretching. Composites were created by averaging all trajectories from all cases at each time along the trajectories.

are synchronized to arrive at z=100 m simultaneously. This time is referred to as the "time of parcel descent". Vorticity production terms were then again analyzed, but only in a 400 s window centered on the time of descent. The remaining figures in this chapter use this new synchronized time framework.

As the parcels descend, negative ζ is produced in both the TOR and NON simulations (Fig. 7.9a). In both composite trajectories, a minimum in ζ occurs approximately 50 s before the time of descent, with the magnitude of this minimum being larger in the TOR composite. In both composites, this minimum in ζ occurs just after a minimum in tilting (Fig. 7.9b) and at approximately the same time as a maximum in stretching (Fig. 7.9c), with the peaks being of larger magnitude in the TOR composite. The decrease in tilting between -200 s and -50 s is associated with increases in horizontal vorticity (Fig. 7.9d), horizontal gradients of vertical velocity (Fig. 7.9e), and baroclinic generation (Fig 7.9f). Again, the peaks are larger in magnitude in the TOR composite. Baroclinic generation is more than two times larger than the tilting/stretching of horizontal vorticity (Fig. 7.9g) at this time, suggesting that the baroclinic generation is the dominant production term of horizontal vorticity as the parcels descend.

As mentioned in the previous chapter, if ζ is negative and stretching is positive, then $\frac{\partial w}{\partial z}$ is also negative. In a descending parcel, $\frac{\partial w}{\partial z}$ becomes negative when the parcel begins to decelerate as it approaches the surface. In the TOR composite, downdrafts are stronger, with a minimum (average) value of -8 m s^{-1} occurring around t=50 s (vs. -6 m s^{-1} in the NON composite; Fig. 7.9h) and thus would experience a stronger

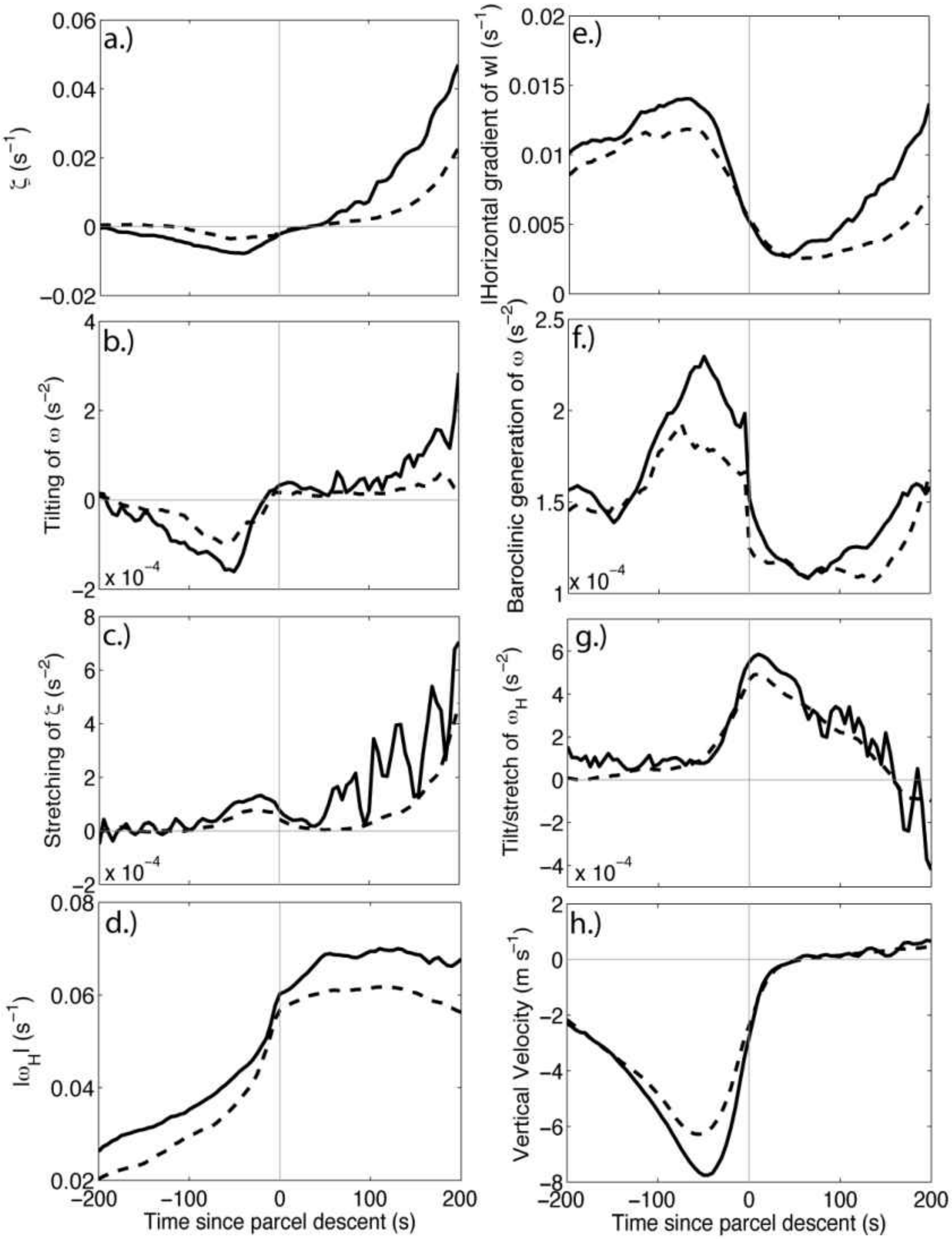

FIGURE 7.9. Composite trajectories for the TOR (solid line) and NON (dashed line) simulations showing time series of (a) vertical vorticity, (b) tilting of horizontal vorticity, (c) stretching of vertical vorticity, (d), magnitude of the horizontal vorticity vector, (e) magnitude of the horizontal gradient in vertical velocity, (f) baroclinic generation of horizontal vorticity, (g) tilting/stretching of horizontal vorticity, and (h) vertical velocity. The x-axis is relative to the time when descending parcels first descend below *z*=100 m.

deceleration as they approach the surface. Hence, stretching is larger in the TOR composite because $\frac{\partial w}{\partial z}$ and ζ are both more negative in the TOR composite.

Between t=-50 s and t=0 s, ζ increases towards zero in both composites (Fig. 7.9a). This increase is associated with increases in tilting and positive stretching (Figs 7.9b,c). As t approaches zero, the differences between the two composites become smaller in nearly every field shown in Fig. 7.9, except baroclinic generation (Fig. 7.9f), which exhibits the largest difference between the two composites during this time frame. The relatively large baroclinic generation in both composites occurs in conjunction with increasing horizontal vorticity (Fig. 7.9d), and increasing tilting/stretching of horizontal vorticity (Fig. 7.9g).

As the parcels descend below z=100 m, ζ continues increasing (but remains negative) in both the TOR and NON composites, with the values being very similar. Horizontal vorticity continues to increase in both the TOR and NON composites (Fig. 7.9d) despite drastic reductions in baroclinic generation (Fig. 7.9f), suggesting that the increase at this time is primarily due to the tilting/stretching term (Fig. 7.9g). The increase is more rapid in the TOR composite (Fig. 7.9d). After t=0 s, the increasing horizontal vorticity occurs while tilting/stretching of horizontal vorticity is large (Fig. 7.9g), ζ is slightly negative (but increasing) and tilting of ζ is positive in both composites (Fig. 7.9b). This suggests that ζ is increasing towards zero, not only due to positive stretching, but also because negative ζ is being tilted into the horizontal.

At approximately t=100 s, differences in vertical vorticity production between the TOR and NON composites become larger. Both composites show increases in ζ (Fig. 7.9a), tilting (Fig. 7.9b), and stretching (Fig. 7.9c) after t=100 s, however the rate of increase in these fields is much larger in the TOR composite. The larger tilting in the TOR composite is associated with greater horizontal vorticity (Fig. 7.9d) and larger gradients in vertical velocity (Fig. 7.9e).

The results thus far have demonstrated that parcels in the TOR simulations arrive at the surface with more horizontal vorticity than the NON simulations. As the parcels travel towards the near-surface circulation, the TOR parcels experience stronger tilting (due to larger horizontal vorticity and stronger gradients in vertical velocity) and stronger stretching (likely due to stronger upward accelerations). These results suggest that that either the low-level updraft is stronger in the TOR simulations, or the TOR parcels are less negatively buoyant than those in the NON simulations and can be more easily lifted by the updraft (or possibly both). Analysis of forward trajectories seeded in the near-surface circulation shows that, on average, parcels in the TOR simulations are lifted to higher altitudes than those in the NON simulations (Fig. 7.10a,c). The differences become even more apparent when relating trajectory height to environmental LFC height (Fig. 7.10b,d). Only three (16%) of the TOR cases have an average parcel height that is well below LFC height, while eight (57%) of the NON simulations have parcels that (on average) do not approach the environmental LFC height.

To determine if the differences in maximum parcel height between the TOR and NON simulations were related to differences in negative buoyancy, perturbations of pseudoequivalent potential temperature (θ_{ep}) were calculated in a 1 km x 1 km box centered on the location of the tornado in the TOR simulations and on the location of maximum 0-1 km UH in the NON simulations at the trajectory initialization time (Fig. 7.11). Perturbations are relative to the surface value of θ_{ep} in the base state environment

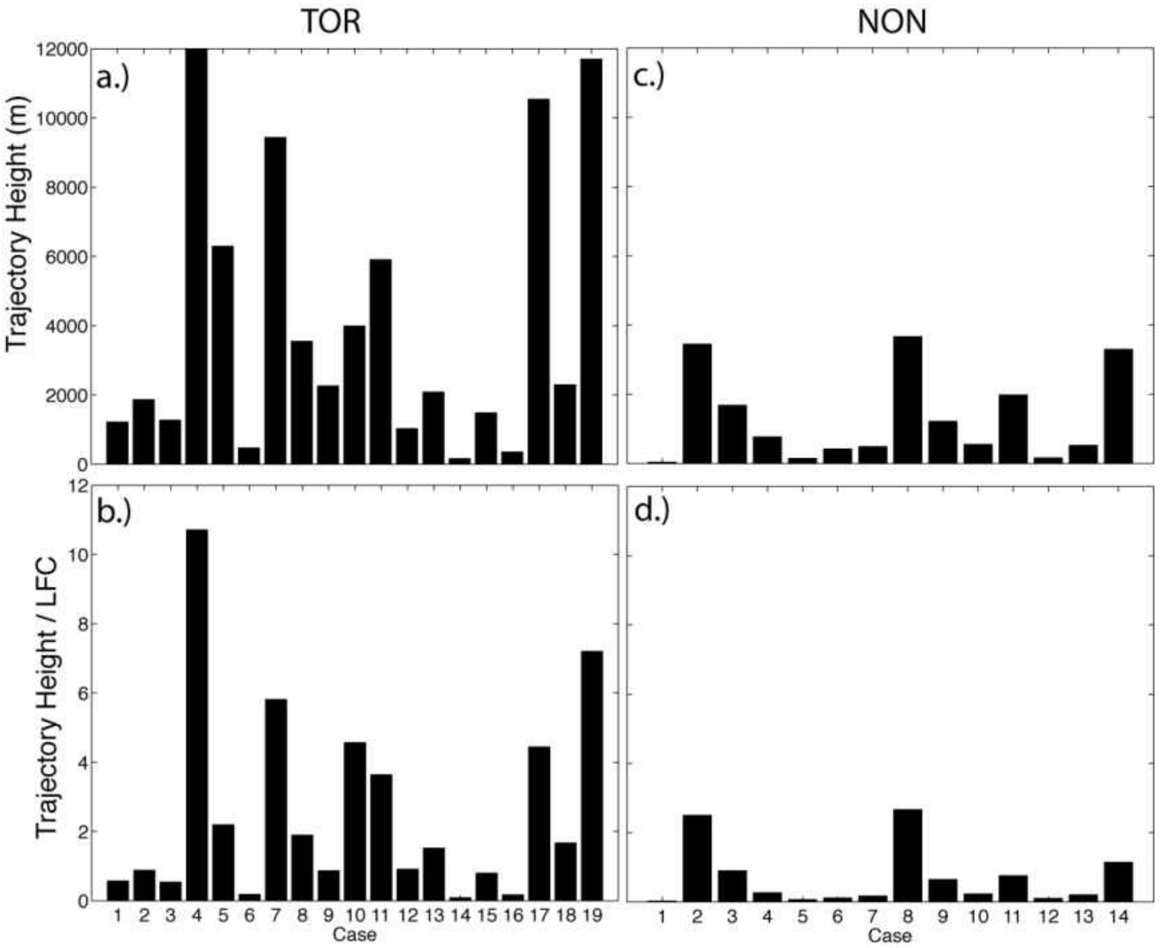

FIGURE 7.10. Average maximum height of forward trajectories for the TOR and NON cases (a & c), and ratio of maximum trajectory height to environmental LFC height (b & d).

and θ_{ep} was calculated following Bolton (1980). The results from this analysis show that the majority of the NON simulations had small magnitude θ_{ep} deficits (i.e. similar to base state environment) whereas many of the TOR simulations had much larger magnitude deficits (i.e. much lower than the base state environment). This suggests that the larger stretching of ζ (Fig. 7.9c) and higher maximum parcel height (Fig. 7.10) in the TOR simulations are due to stronger updrafts, and are not strongly related to differences in cold pool thermodynamics between the TOR and NON simulations. Thus, this result conflicts with the hypothesis derived from observational studies (e.g. Markowski et al. 2002) that non-tornadic storms simply have colder low-level outflow.

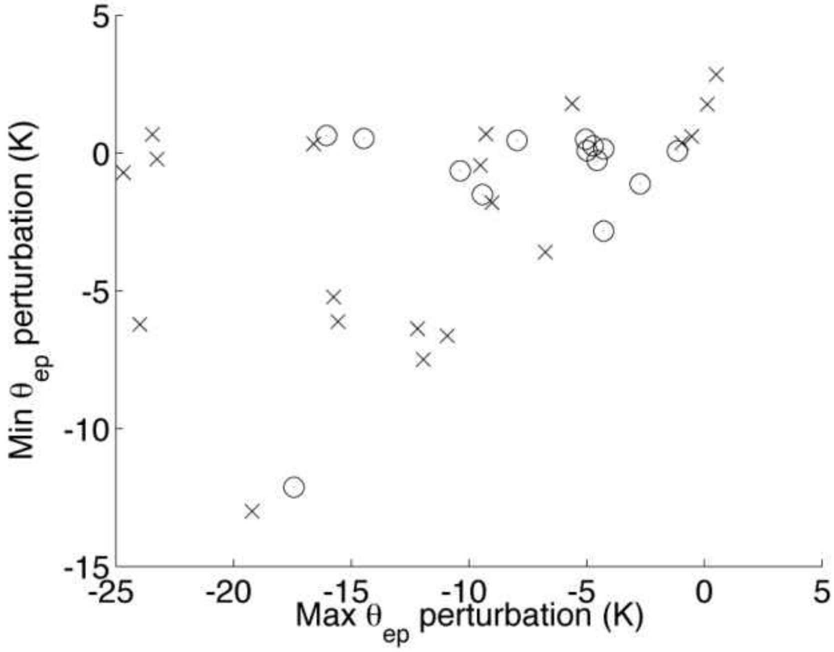

FIGURE. 7.11. Maximum and minimum perturbations of pseudoequivalent potential temperature (θ_{ep}) for the TOR (x's) and NON (o's) simulations. Perturbations are relative to the surface value in the base state environment.

Discussion

In this chapter, it was shown that differences in the TOR and NON simulations are mainly apparent in processes occurring in descending parcels. In the TOR simulations, parcels produce more negative ζ while they descend than parcels in the NON simulations. It appears that as the parcels in both categories reach the surface, this negative ζ developed during descent (which is reduced in magnitude to some degree by stretching during the final part of the descent) is tilted back into the horizontal. The parcels then travel horizontally and, as they rise, the horizontal vorticity is tilted back into the vertical by strong horizontal gradients in vertical velocity. Thus, it seems that the main differences between the TOR and NON simulations is that the TOR simulations have larger horizontal vorticity after they reach the surface—due in part to larger initial (i.e. environmental) horizontal vorticity and also more baroclinic generation and more tilting of negative ζ produced during descent—that is tilted in the vertical by stronger low-level updrafts.

Certainly, these variations in vorticity production are due to differences in the initial environments of the TOR and NON simulations. Thompson et al. (2003) showed that two of the most statistically significant differences between the significantly tornadic and nontornadic proximity soundings were mixed layer CAPE, and 0-1 km SREH. It was found that both CAPE and SREH were smaller in the nontornadic soundings. The same is true for the soundings used in this study, albeit with substantially less overlap. Nearly every TOR simulations had larger CAPE than the NON simulations (Fig. 7.12a). Thus, it should not be surprising that the horizontal gradients of vertical velocity were larger in the TOR simulations, since CAPE is proportional to vertical velocity (e.g. Weisman and Klemp 1982). Additionally, the NON simulations had larger magnitude CIN (Fig. 7.12b), which has been shown to reduce the strength of the low-level updraft (Naylor et al. 2012).

The discrepancies in CAPE and CIN are also likely to influence outflow thermodynamics. Numerous studies have suggested that the cold pools in nontornadic supercells are more negatively buoyant (i.e. larger θ_{ep} deficits) than tornadic supercells. However, the results in this chapter show that the largest θ_{ep} deficits actually occurred in the TOR simulations. Since CAPE is substantially larger in the TOR simulations, it seems reasonable to expect that these simulations will also have stronger downdrafts (e.g. Srivastava 1987), and more precipitation production (e.g. Weisman and Klemp 1982)—hence more evaporational cooling and melting. Additionally, the NON simulations have

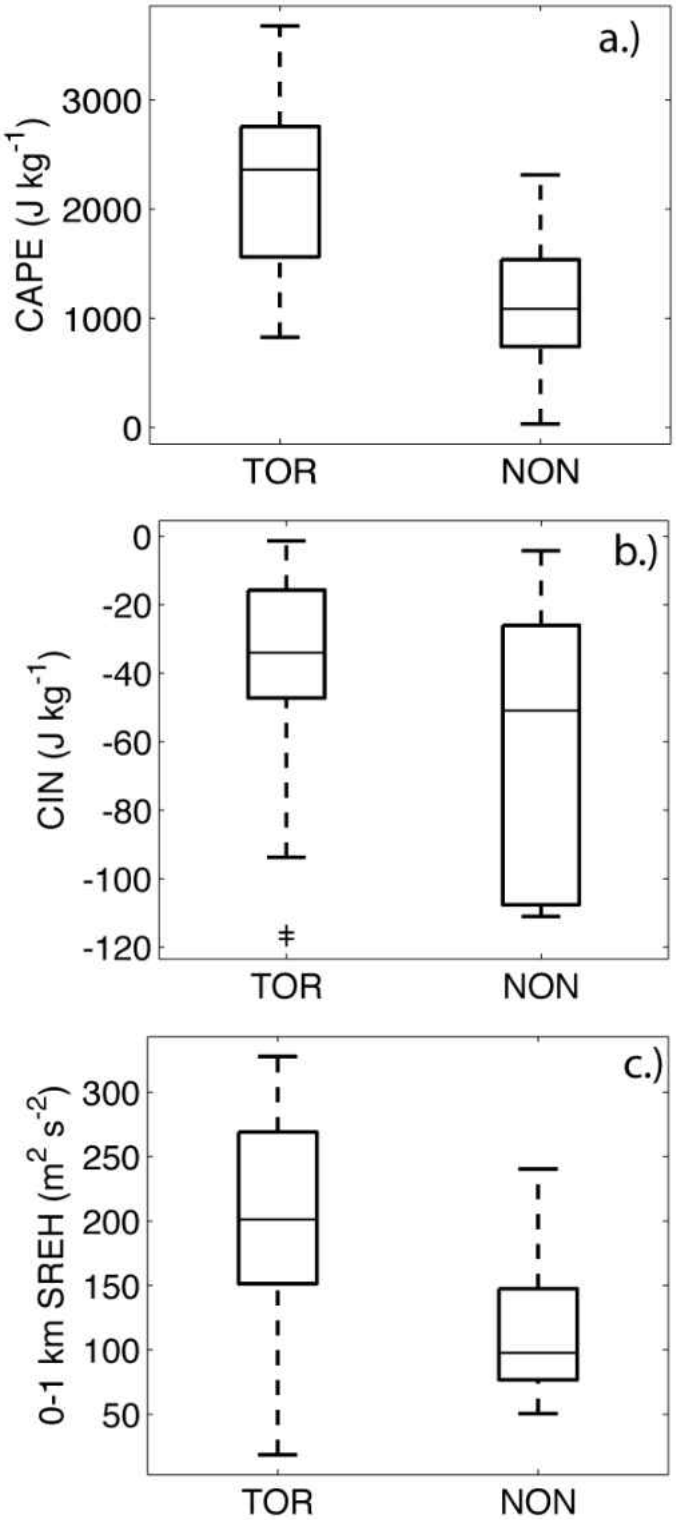

FIGURE 7.12. Box and whisker plots of (a) CAPE, (b), CIN, and (c) 0-1 km SREH. CAPE and CIN are calculated using a 500 m mixed layer and the virtual temperature correction from Doswell and Markowski (2004). Storm motion in SREH calculations follows Bunkers et al. (2000).

more CIN on average, which has been shown by Naylor et al. (2012) to reduce θ_{ep} deficits in the cold pool.

There are several possible reasons why the cold pool characteristics of these simulations seemingly disagree with past studies. Markowski et al. (2002)—the first study to link tornadogenesis to cold pool characteristics—showed that the largest differences in cold pools are between significantly tornadic and nontornadic supercell, whereas in the analysis presented in this chapter, no distinction is made between weak tornadoes and significant tornadoes. Secondly, observations of cold pool temperature may have not been taken precisely at the time of tornadogenesis or tornadogenesis failure. Many of these studies state that cold pool measurements were taken "within 5 min" of tornadogenesis (i.e. Markowski et al. 2002, Grzych et al. 2007). It is possible that many of the observations were taken *after* tornadogenesis occurred. Thus, perhaps the 'warm' outflow air near the tornado is a result of the tornado and not a precursor to its formation, as has been suggested by some numerical simulations (M. Gilmore, personal communication). It is also possible that the NON environments in this study did not adequately represent the range of CAPE values typical of nontornadic storms. The CAPE in nearly every NON simulation in this study was less than the median value in the full Thompson et al. (2003) dataset. Lastly, limitations in the microphysics parameterization may have led to enhanced cold pools. Kumjian (2011) found that hydrometeor dropsize distributions have large spatial variability in and around the hook echo of supercells, including regions dominated by large raindrops. Such distributions are more common in storms occurring in environments with large SREH (Kumjian and Ryzhkov 2007, 2010), which would make them more likely in tornadic supercells than nontornadic. However, this type of dropsize distribution is not possible with the microphysics scheme used in this study. The single moment scheme used here resets the dropsize distribution to an inverse exponential form after each time step. This results in the artificial insertion of numerous small raindrops, which easily evaporate (e.g. Dawson et al. 2010). This added evaporation might enhance downdrafts and bring lower θ_{ep} air to the surface.

It seems that both barotropically and baroclinically generated horizontal vorticity were important in the TOR simulations. The larger barotropic vorticity in these cases (i.e. larger SREH; Fig. 7.12c) not only results in larger initial vorticity along the trajectories, but should also produce a larger vertical pressure gradient force that strengthens low-level updrafts (e.g. Rotunno and Klemp 1982, Brooks and Wilhelmson 1993)—thus enhancing stretching and horizontal gradients of vertical velocity. The larger barotropic vorticity in the TOR simulations may also explain differences in negative ζ production between descending parcels in the TOR and NON simulations. Davies-Jones and Brooks (1993) state that tilting of horizontal vorticity produces downdrafts with anticyclonic vorticity (i.e. negative ζ) when the horizontal vorticity is purely streamwise, and zero net ζ when the flow is purely crosswise, owing to symmetry. Although Davies-Jones and Brooks only discuss these two extremes, it seems reasonable that there is a continual increase in net anticyclonic vorticity production as the flow becomes more streamwise—which is proportional to SREH. In fact, Fig. 7.13 does show a somewhat linear association between SREH and negative ζ in descending parcels. Thus, the larger SREH in the TOR simulations seems to result in larger negative ζ as the parcels descend, which then tilts into the horizontal as it reaches the surface and increases the magnitude of horizontal vorticity.

However, there is also evidence suggesting that baroclinic generation is extremely important to the evolution of vorticity in the descending parcels. Peaks in baroclinic generation occurred in conjunction with peaks in tilting of ζ and increases in horizontal vorticity in the descending parcels of both the TOR and NON simulations. In addition, baroclinic generation was an order of magnitude larger than the production of horizontal vorticity via tilting/stretching throughout a large portion of parcel descent.

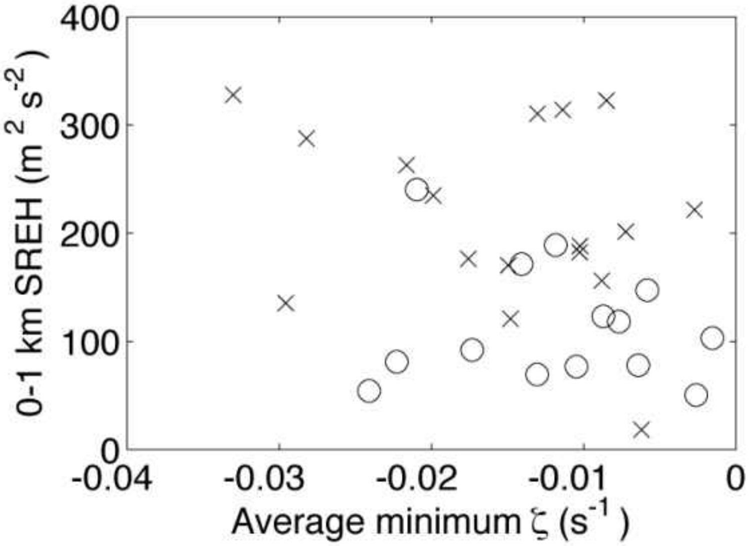

FIGURE 7.13. Scatter plot of 0-1 km storm relative environmental helicity vs. average minimum vertical vorticity in descending parcels from the TOR (x's) and NON (o's) simulations.

Overall, vorticity production in the TOR simulations agrees quite well with previous studies. Parcels that descend from aloft primarily generate negative vertical vorticity as they descend [e.g. Brandes (1984), Davies-Jones and Brooks (1993), Wicker and Wilhelmson (1995), Adlerman et al. (1999)]. During descent, tilting is negative, while stretching is positive [Wicker and Wilhelmson (1995), Adlerman et al. 1999]. As parcels approach the surface, baroclinic generation of horizontal vorticity increases [Davies-Jones and Brooks (1993), Wicker and Wilhelmson (1995), Adlerman et al. (1999)]. Only after the parcels reach the surface do they acquire positive ζ [in agreement with Wicker and Wilhelmson (1995)].

CHAPTER 8

SUMMARY AND CONCLUSIONS

In this study an idealized cloud model was used to investigate storm-scale mechanisms important for tornadogenesis and tornadogenesis failure. Simulations were initialized with supercell proximity soundings associated with significantly tornadic (>= F2 or lasting longer than 5 min) and nontornadic supercells. Theses soundings were taken from the RUC-2 model, and were used by Thompson et al. (2003,2007).

The vast majority of these soundings contain capping inversions, making convective initiation in the idealized cloud model difficult. The traditional thermal bubble initiation technique proved ineffective at producing strong, sustained supercells. Recently, a sustained updraft nudging technique has been used to initiate storms in capped environments (Ziegler et al. 2010). However, this technique is relatively new and the optimal configuration was not known prior to this study.

Over 1000 simulations were planned for the convective initiation tests, making it impossible to subjectively analyze all times in every case. Before convective initiation experiments could be performed, an automated method for determining supercell strength and longevity was needed. In Chapter 3, three techniques were tested: the Pearson Correlation between vertical vorticity and vertical velocity; a modified version of the Pearson Correlation that calculated the correlation coefficient at multiple locations in the domain; and updraft helicity. It was found that updraft helicity (integrated from 2-5 km) had the most skill at detecting supercells in course resolution simulations (dx=2 km), with the modified Pearson Correlation (averaged from 2-5 km) performing best at finer resolution (dx < 500 m). At resolutions between these two values, both the updraft helicity and modified Pearson Correlation techniques performed nearly equally well. In both of these techniques, false alarms were decreased by imposing the additional criteria that the detection threshold be exceeded for at least 20 min.

With a reliable method for supercell detection established, convective initiation tests were conducted in Chapter 4. While the thermal bubble technique only produced supercells in a small number of the simulations, the updraft nudging technique (with the nudging spheroid centered at z=1.5 km) produced supercells in nearly every simulation, regardless of nudging duration. It was found that the updraft nudging technique resulted in the strongest and longest-lived supercells (on average) when applied for the first 15 min of simulation time. Additionally, the updraft nudging technique was less effective when the nudging spheroid was placed near the surface.

Using the optimal updraft nudging settings found in Chapter 4, simulations were generated using the RUC-2 soundings using 100 m grid spacing in the horizontal and vertical—a grid spacing small enough to allow the presence of tornado-like vortices. Of the 113 significantly tornadic RUC-2 soundings, 60 were chosen for the 100 m simulations, based on supercell properties in these soundings simulated with 1 km horizontal gridspacing. Of these 60 simulations, 21 produced tornadic supercells, 9 produced nontornadic supercells (not analyzed), and 30 did not produce a supercell (not analyzed). Supercell presence was determined based on a combined subjective/objective approach, with the objective portion relying on the updraft helicity technique, with a detection threshold extrapolated from the results of Chapter 3. Tornado detection was also automated, with the assumption that the tornadoes resembled a Rankine vortex.

The properties of the tornadoes in the 21 tornadic simulations were presented in Chapter 5 and were found to be largely determined by the magnitude of 0-3 km storm relative environmental helicity (SREH) in the initial sounding. Increases in 0-3 km SREH were strongly associated with longer tornado durations, and greater pressure drops at the center of the tornadoes. A statistically significant signal was also found using 0-1 km SREH, although the relationship was stronger when SREH was integrated from 0-3 km.

In Chapter 6, trajectories were seeded at low-levels at the time of tornadogenesis (i.e. first tornado detection) in all 21 tornadic simulations. Two cases were removed from analysis due to the tornado detection not being associated with the main mesocyclone. These trajectories were followed backwards for 900 s to determine the source region(s) of the parcels entering the tornadic circulation and also to analyze vorticity production as the parcels travel towards the tornado. There were two primary types of trajectories: those that originated near the surface in the inflow region ahead of the storm, traveled along the forward flank gust front and steadily rose as they approached the tornado (‘rising’ parcels), and parcels that originated aloft and descended to the surface (‘descending’ parcels). In the rising parcels, positive vertical vorticity was first produced by tilting of horizontal vorticity as the parcels ascend. Tilting frequently occurred only after the generation of baroclinic horizontal vorticity. In the descending parcels, positive vertical vorticity appeared to occur primarily after the parcels had reached the surface. During descent, negative vertical vorticity was produced in many of the trajectories. The production of positive vertical vorticity at the surface was associated with relatively large generation of baroclinic vorticity.

Finally, in Chapter 7, a subset of the nontornadic RUC-2 soundings was simulated at 100 m resolution in order to compare vorticity production terms in nontornadic simulations with the tornadic simulations of Chapter 6. Forty of the RUC-2 soundings that produced strong supercells in 1 km simulations were randomly selected for simulation at 100 m resolution. Of these 40 simulations, 16 produced nontornadic supercells, 10 produced tornadic supercells (not analyzed), and 14 did not produce a supercell (not analyzed). The 14 nontornadic supercells were then compared to the 19 tornadic simulations analyzed in Chapter 6. The following conclusions were reached. In comparing the tornadic and nontornadic simulations,

- vertical vorticity production in rising parcels was similar. The nontornadic simulations tended to have more baroclinic generation while the tornadic simulations had larger stretching, with the largest differences in stretching occurring less than 60 s prior to tornadogenesis or tornadogenesis failure. However, the dramatic increase in stretching just prior to tornadogenesis was likely a result of the tornadoes themselves.
- vertical vorticity production in descending parcels was noticeably different. Tilting was much larger in magnitude in the tornadic simulations, with strong positive and negative tilting occurring along the trajectories. Differences in tilting became large nearly 400 s before the parcels ended in the near-surface circulation.

- the larger tilting in descending parcels in the tornadic simulations can be attributed to larger horizontal vorticity and stronger horizontal gradients of vertical velocity.
- the tornadic simulations had larger negative (anticyclonic) vertical vorticity production in the descending trajectories. This anticyclonic vertical vorticity was generated as the parcels descended to the surface. Peaks in anticyclonic vorticity occurred in association with peaks in negative tilting, positive stretching, and baroclinic generation—all of which were larger in the tornadic simulations.
- Vertical vorticity became positive in descending parcels only after they reached the surface (on average). The increase in vertical vorticity after descent was stronger in the tornadic simulations, owing to larger horizontal vorticity and stronger horizontal gradients in vertical velocity.
- forward-integrated trajectories reached higher altitudes (on average) in the tornadic simulations. Most of the trajectories in the nontornadic simulations were unable to reach the environmental LFC height.
- the strongest cold pools in the vicinity of the low-level mesocyclone were associated with the tornadic simulations. Most of the nontornadic simulations had cold cools with small deficits of pseudoequivalent potential temperature.

In conclusion, the largest differences between the tornadic and nontornadic supercells are related to vorticity production in parcels that descend from aloft. The tornadic (nontornadic) simulations produce more (less) anticyclonic vertical vorticity during parcel descent, which is generated by larger (smaller) tilting and stretching production. As the parcels reach the surface, they are tilted back into the horizontal.

After the parcels reach the surface, the magnitude of the horizontal vorticity is larger (smaller) in the tornadic (nontornadic) simulations due to the larger (smaller) initial horizontal vorticity (i.e. barotropic), larger (smaller) baroclinic generation during descent, and greater (weaker) anticyclonic vertical vorticity production during descent, which is tilted into the horizontal direction near the surface. This horizontal vorticity is then tilted into the vertical direction and stretched, with both of these processes being larger in the tornadic simulations due to stronger updrafts. The stronger (weaker) updrafts in the tornadic (nontornadic) simulations appear to be a result of larger CAPE, but not the thermodynamic properties of the descending parcels. Thus, tornadogenesis failure in the NON cases is due to weaker overall vorticity production (compared to the TOR cases), and is not simply a result of excess negative buoyancy in the storm outflow.

This work could be expanded in future studies by analyzing the tornadic simulations at multiple times to investigate the processes responsible for tornado maintenance and demise. In addition, several of the tornadic simulations contained multiple tornadoes. These tornadoes could be analyzed to determine if the processes related to initial tornadogenesis differ from subsequent tornadogenesis events. It would also be interesting to examine the nontornadic (tornadic) supercell simulations that resulted from the use of significantly tornadic (nontornadic) RUC-2 soundings.

APPENDIX A

Vorticity and Vortex lines

In order to discuss the origins of rotation in supercells and tornadoes, the concepts of vorticity and vortex lines must be introduced. Vorticity is defined as the curl of the wind field and is represented as

$$\vec{\omega} = \left[\left(\frac{\partial w}{\partial y} - \frac{\partial v}{\partial z} \right) \hat{i}, \left(\frac{\partial u}{\partial z} - \frac{\partial w}{\partial x} \right) \hat{j}, \left(\frac{\partial v}{\partial x} - \frac{\partial u}{\partial y} \right) \hat{k} \right], \tag{A1}$$

where u, v, and w are the Cartesian components of the wind field. Because supercells and tornadoes rotate about a vertically oriented axis, the development of the vertical component of $\boldsymbol{\omega}$ (herein denoted as ζ) is considered most important. By taking the curl of the anelastic, non-rotating form of the horizontal momentum equations,

$$\frac{\partial u}{\partial t} = -\vec{u} \cdot \nabla u - \frac{1}{\rho} \frac{\partial p}{\partial x}, \tag{A2}$$

$$\frac{\partial v}{\partial t} = -\vec{u} \cdot \nabla v - \frac{1}{\rho} \frac{\partial p}{\partial y}, \tag{A3}$$

where, ρ is density, and p is pressure, the local rate of change of ζ can be represented as

$$\frac{\partial \zeta}{\partial t} = -v \cdot \nabla \zeta + \left(\frac{\partial u}{\partial z} \frac{\partial w}{\partial y} - \frac{\partial v}{\partial z} \frac{\partial w}{\partial x} \right) + \zeta \frac{\partial w}{\partial z}. \tag{A4}$$

The three terms on the RHS of (A4) represent advection of vertical vorticity, tilting of horizontal vorticity, and stretching of vertical vorticity, respectively. It can be seen from (A4) that, in the absence of pre-existing vertical vorticity, the tilting of horizontal vorticity is the only source of vertical vorticity. Equations for the horizontal components of vorticity can be derived in a similar manner, however they are not shown. It is important to note that horizontal vorticity has an additional source that is important in supercell dynamics. Horizontal vorticity may be generated baroclinically by horizontal density gradients. This is believed to be an important process in supercells, particularly along the forward flank gust front.

A vortex line is then defined as a curve that is at all points tangent to the vorticity vector. Davies-Jones (1984) showed that, in the absence of baroclinic generation, vortex lines act as if they are frozen in the fluid. This behavior can be demonstrated by invoking the concept of potential vorticity (PV) in a simplied conceptual model. If friction and Coriolis forces are ignored, PV is defined as

$$PV = \frac{1}{\rho}\vec{\omega}\cdot\nabla\theta \ , \qquad \text{(A5)}$$

where ρ is the density of the air and θ is the potential temperature. PV is conserved following the motion in adiabatic, frictionless flow.

Consider a dry, homogeneous, initially hydrostatic atmosphere with $\frac{d\theta}{dz} > 0$. In addition, assume the fluid flow is towards the positive x direction with wind speed increasing with height (Fig A1a). In this scenario, the environment contains only horizontal components of vorticity, with the vortex lines pointing in the positive x direction. Note that since the environment initially has no vertical vorticity and no horizontal gradient of θ, PV=0. Since θ is a conserved quantity (in a dry atmosphere), lines of constant θ, or isentropes, can be considered material surfaces that deform with the fluid. Now, consider a thermal perturbation in the atmosphere that produces a positive vertical velocity (Fig A1b). As the thermal rises, the isentropic surfaces become deformed and also rise (i.e. the local derivatives of a θ are changing). On the left hand side of the thermal, $\frac{d\theta}{dz} \rightarrow 0$ while $\frac{d\theta}{dx}$ becomes negative. Thus, in order to conserve PV, ζ must become positive. On the right side of the thermal, $\frac{d\theta}{dz} \rightarrow 0$ and $\frac{d\theta}{dx}$ now becomes positive. To conserve PV, ζ becomes negative. Hence, the vortex lines act as if they are frozen in the flow and will deform as the fluid deforms. Rotunno and Klemp (1985) used a similar but more complex argument to explain the development of midlevel rotation in their supercell simulations. They used Ertel's equivalent potential vorticity to explain the development of rotation in a moist, three-dimensional atmosphere.

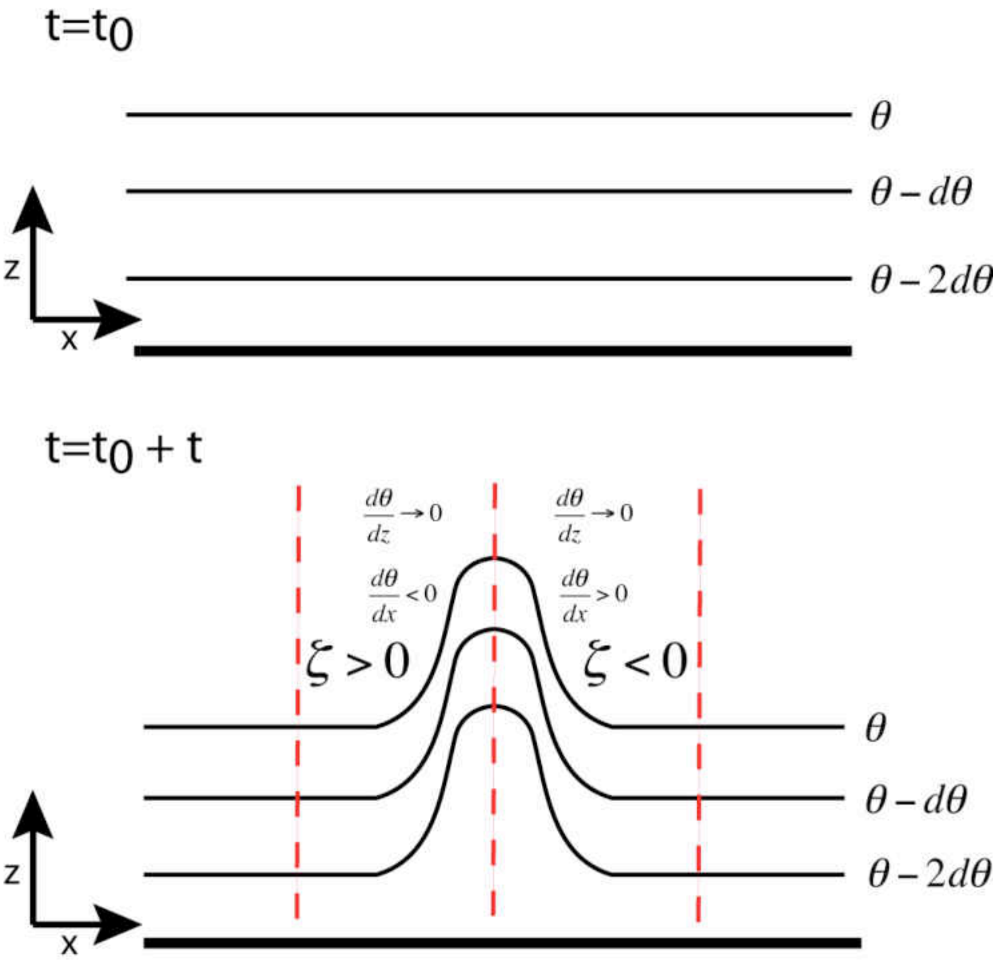

FIGURE A1. Illustration of how deformation of isentropes produces vertical vorticity through conservation of potential vorticity.

REFERENCES

Adlerman, E. J., K. K. Droegemeier, and R. Davies-Jones, 1999: A numerical simulation of cyclic mesocyclogenesis. *J. Atmos. Sci.*, **56**, 2045-2069.

____, and ____, 2005: The dependence of numerically simulated cyclic mesocyclogenesis upon environmental vertical wind shear. *Mon. Wea. Rev.*, **133**, 3595-3623.

Arakawa, A., and V. Lamb, 1977: Computational design of the basic dynamical processes in the UCLA general circulation model. *Methods of Computational Physics*. 17, Academic Press, 174-264.

Atkins, N. T., M. L. Weisman, and L. J. Wicker, 1999: The influence of preexisting boundaries on supercell evolution. *Mon. Wea. Rev.*, **127**, 2910-2927.

Beebe, R. G., 1955: Types of airmasses in which tornadoes occur. *Bull. Amer. Meteor. Soc.*, **36**, 349-350.

____, 1958: Tornado proximity soundings. *Bull. Amer. Meteor. Soc.*, **39**, 195-201.

Brandes, E. A., 1984: Vertical vorticity generation and mesocyclone sustenance in tornadic thunderstorms: The observational evidence. *Mon. Wea. Rev.*, 2253-2269.

Brooks, H. E., 1992: Operational implications of the sensitivity of modelled thunderstorms to thermal perturbations. Preprints, *Fourth AES/CMOS Workshop on Operational Meteorology*, Whistler, B.C., Canada. Atmospheric and Environmental Service and Canadian Meteorological and Oceanographic Society, 398-407.

____, C. A. Doswell III, and R. Davies-Jones, 1993: Environmental helicity and the maintenance and evolution of low-level mesocyclones. *The Tornado: Its Structure, Dynamics, Prediction, and Hazards, Geophys. Monogr.*, No 79, Amer. Geophys. Union, 97-104.

____, ____, and L. J. Wicker, 1993: STORMTIPE: A forecasting experiment using a three-dimensional cloud model. *Wea. Forecasting*, **8**, 352–362.

____, and R. B. Wilhelmson, 1993: Hodograph curvature and updraft intensity in numerically modeled supercell. *J. Atmos. Sci.*, **50**, 1824-1833.

____., C. A. Doswell III, and J. Cooper, 1994: On the environments of tornadic and nontornadic mesocyclones. *Wea. Forecasting*, **9**, 606-618.

Benjamin, S. G. et al., 2004: An hourly assimilation-forecast cycle: The RUC, *Mon. Wea. Rev.*, *132*, 495-518.

Brown, R. A., 1998: Nomogram for aiding the interpretation of tornadic vortex signatures measured by Doppler radar. *Wea. Forecasting*, **13**, 505–512.

_____. and V. T. Wood, 1991: On the interpretation of single-Doppler velocity patterns within severe thunderstorms. *Wea. Forecasting*, **6**, 32–48.

Browning, K. A., 1964: Airflow and precipitation trajectories within severe local storms which travel to the right of the winds. *J. Atmos. Sci.*, **21**, 634–639.

—, and F.A. Ludlam, 1962: Airflow in convective storms. *Quart. J. Roy. Meteor. Soc.*, **88**, 117–135.

—, and R.J. Donaldson, 1963: Airflow and structure of a tornadic storm. *J. Atmos. Sci.*, **20**, 533–545.

Bryan, G. H. and M. Fritsch, 2002: A benchmark simulation for moist nonhydrostatic numerical models. *Mon. Wea. Rev.*, **130**, 2917-2928.

____, J. C. Wyngaard, and J. M. Fritsch, 2003: Resolution requirements for the simulation of deep moist convection. *Mon. Wea. Rev.*, **131**, 2394-2416. *Wea. Forecasting*, **15**, 61-79.

Bunkers, M. J., B. A. Klimowski, J. W. Zeitler, R. L. Thompson, and M. L. Weisman, 2000: Predicting supercell motion using a new hodograph technique.

____, M. R. Hjelmfelt, and P. L. Smith, 2006: An observational examination of long-lived supercells. Part I: Characteristics, evolution, and demise. *Wea. Forecasting*, **21**, 673–688.

Chen, C. H. and H. D. Orville, 1980: Effects of mesoscale convergence on cloud convection. *J. Appl. Meteor.* ,**19**, 256-274.

Clark, T. L., 1979: Numerical simulations with a three-dimensional cloud model: Lateral boundary condition experiments and multicellular severe storm simulations. *J. Atmos. Sci.*, **36**, 2191-2215.

Dahl, J., M. Parker, and L. Wicker, 2012: Uncertainties in trajectory calculations within near-surface mesocyclones of simulated supercells. *Mon. Wea. Rev.*, in press.

Davies, J. M., and R. H. Johns, 1993: Some wind and instability parameters associated with strong and violent tornadoes. 1. Wind shear and helicity. *The Tornado: Its Structure, Dynamics, Prediction, and Hazards, Geophys. Monogr.*, No 79, Amer. Geophys. Union, 573-582.

Davies-Jones, R. P., 1982: Observational and theoretical aspects of tornadogenesis. Intense Atmospheric Vortices, L. Bengtsson and J. Lighthill, Eds., Springer-Verlag, 175-189.

____, 1984: Streamwise vorticity: The origin of updraft rotation in supercell storms. *J. Atmos. Sci*. **41**, 2991-3006.

____, 2008: Can a descending rain curtain in a supercell instigate tornadogenesis barotropically? *J. Atmos. Sci.*, **65**, 2469-2497.

____, and H. Brooks, 1993: Mesocyclogenesis from a theoretical perspective. *The Tornado: Its Structure, Dynamics, Prediction, and Hazards, Geophys. Monogr.*, No 79, Amer. Geophys. Union, 105-114.

_____, and V. T. Wood, 2006: Simulated Doppler velocity signatures of evolving tornado-like vortices. *J. Atmos. Ocean. Tech.*, **23**, 1029-1048.

Darkow, G. L., 1969: An analysis of over sixty tornado proximity soundings. Preprints, *Sixth Conference on Severe Local Storms*, Chicago, IL, Amer. Met. Soc., 218-221.

Davies, J. M., and R. H. Johns, 1993: Some wind and instability parameters associated with strong and violent tornadoes 1. Wind shear and helicity. *The Tornado: Its Structure, Dynamics, Prediction, and Hazards, Geophys. Monogr.* Vol. 79, Amer. Geophys. Union, 573–582.

Doswell, C. A III, 2001: Severe convective storms-An overview. *Severe Convective Storms*, *Meteor. Monogr.*, No. 50, Amer. Meteor. Soc., 1–26.

—–, and D. W. Burgess, 1993: Tornadoes and tornadic storms: A review of conceptual models. *The Tornado: Its Structure, Dynamics, Prediction, and Hazards, Geophys. Monogr.* Vol. 79, Amer. Geophys. Union, 161–172.

Dowell, D. C., and H. B. Bluestein, 2002: The 8 June 1995 McLean, Texas, Storm. Part II: Cyclic tornado formation, maintenance, and dissipation, *Mon. Wea. Rev., 130*, 2649-2670.

Droegemeier, K. K, S. M. Lazarus, and R. Davies-Jones, 1993: The influence of helicity on numerically simulated convective storms. *Mon. Wea. Rev.*, **121**, 2005-2029.

Elmore, K. L, D. J. Stensrud, and K. C. Crawford, 2002: Explicit cloud-scale models for operational forecasts: A note of caution. *Wea. Forecasting*, **17**, 873-884.

Fawbush, E. J., and R. C. Miller, 1952: A mean sounding representative of the tornadic airmass environment. *Bull. Amer. Meteor. Soc.*, **33**, 303-307.

____, and ____, 1954: The types of airmasses in which North American tornadoes form. *Bull. Amer. Meteor. Soc.*, **35**, 154-165.

Fierro, A. O., M. S. Gilmore, E. R. Mansell, L. J. Wicker, and J. M. Straka, 2006: Electrification and lightning in an idealized boundary-crossing supercell simulation of 2 June 1995. *Mon. Wea. Rev.*, **134**, 3149-3172.

Finley, C. A., W. R. Cotton, and R. A. Pielke Jr., 2001: Numerical simulation of tornadogenesis in a high-precipitation supercell. Part I: Storm evolution and transition into a Bow Echo. *J. Atmos. Sci.*, **58**, 1597-1629.

Fujita, T., 1958: Mesoanalysis of the Illinois tornadoes of 9 April 1953. *J. Meteor*., **15**, 288–296.

____, 1975: New evidence from April 3-4, 1974 Tornadoes. Preprints, *Ninth Conf. on Severe Local Storms*, Norman, OK, Amer. Met. Soc., 248-255.

Gaudet, B. J., and W. R. Cotton, 2006a: Low-level mesocyclonic concentration by nonaxisymmetric transport. Part I: Supercell and Mesocyclone evolution. *J. Atmos. Sci.*, **63**, 1113-1133.

____, and ____, 2006b: Low-level mesocyclonic concentration by nonaxisymmetric transport. Part II: Vorticity dynamics. *J. Atmos. Sci.*, **63**, 1134-1150.

Gilmore, M. S., and L. J. Wicker, 1998: The influence of midtropospheric dryness on supercell morphology and evolution. *Mon. Wea. Rev.*,**126**, 943-958.

____, J. M. Straka, and E. N. Rasmussen, 2004: Precipitation and evolution sensitivity in simulated deep convective storms: Comparisons between liquid-only and simple ice and liquid phase microphysics. *Mon. Wea. Rev*., **132,** 1897-1916.

Glickman, T. S., 2000: Glossary of Meteorology. 2d ed. American Meteorological Society, 855 pp

Grasso, L. D., and W. R. Cotton, 1995: Numerical simulation of a tornado vortex. *J. Atmos. Sci.*, **52**, 1192-1203.

Grzych, M. L., B. D. Lee, and C. A. Finley, 2007: Thermodynamic analysis of supercell rear-flank downdrafts from project ANSWERS. *Mon. Wea. Rev*., **135**, 240-246.

Hirth, B. D., J. L. Schroeder, and C. C. Weiss, 2008: Surface anaylsis of the rear-flank downdraft outflow in two tornadic supercells. *Mon. Wea. Rev*., **136**, 2344-2363.

Johnson, D. E., P. K. Wang, and J. M. Straka 1993: Numerical simulations of the 2 August 1981 CCOPE supercell storm with and without ice microphysics. *J. Appl. Meteor*., **32**, 745-759.

Kain, J. S., S. J. Weiss, J. J. Levit, M. E. Baldwin, and D. R. Bright, 2006: Examination of convective allowing configurations of the WRF model for the prediction of severe convective weather: The SPC/NSSL spring program 2004. *Wea. Forecasting*, **21**, 167-181.

____, S. J. Weiss, D. R. Bright, M. E. Baldwin, J. L. Levit, G. W. Carbin, C. S. Shwartz, M. L. Weisman, K. K. Droegemeier, D. B. Weber, and K. W. Thomas, 2008: Some practical considerations regarding horizontal resolution in the first generation of operation convective-allowing NWP. *Wea. Forecasting*, **23**, 931-952.

Kalnay, E., 2004: *Atmospheric Modeling, Data Assimilation, and Predictability*. Cambridge, 341 pp.

Kirkpatrick, J. C., E. W. McCaul, and C. Cohen, 2007: The motion of simulated convective storms as a function of basic environmental parameters. *Mon. Wea. Rev.*, **135**, 3033-3051.

Klemp J. B., and R. B. Wilhelmson, 1978: The simulation of three-dimensional convective storm dynamics. *J. Atmos. Sci*., **35**, 1070-1096.

____, ____, and P. S. Ray, 1981: Observed and numerically simulated structure of a mature supercell thunderstorm. *J. Atmos. Sci.*,38, 1558-1580

____, and R. Rotunno, 1983: A study of the tornadic region within a supercell thunderstorm. *J. Atmos. Sci*., **40**, 359-377.

Klimowski, B. A., M. J. Bunkers, M. R. Hjelmfelt, and J. N. Covert, 2003: Severe convective windstorms over the northern high plains of the United States. *Wea. Forecasting*, **18**, 502–519.

Knupp, K. R., J. R. Stalker, and E. W. McCaul Jr., 1998: An observational and numerical study of a mini-supercell storm. *Atmos. Res.*, **49,** 35–63.

Lee, B. D. and R. B. Wilhelmson, 1997: The numerical simulation of nonsupercell tornadogenesis. Part II: Evolution of a family of tornadoes along a weak outflow boundary. *J. Atmos. Sci.*, **54**, 2387-2415.

Lemon, L. R., 1977: New Severe thunderstorm radar identification techniques and warning criteria: A preliminary report. NOAA Tech. Memo. NWS NSSFC-1, 60 pp. [NTIS-PB-273049.]

—–, and C. A. Doswell III, 1979: Severe thunderstorm evolution and mesocyclone structure as related to tornadogenesis. *Mon. Wea. Rev.*, **106**, 48–61.

Lerach, D. G., B. J., Gaudet, and W. R. Cotton, 2008: Idealized simulations of aerosol influences on tornadogenesis. *Geophys. Res. Lett*., **35**, L23806.

Letkewicz, C. E., and M. D. Parker, 2011: Impact of environmental variations on simulated squall lines interacting with terrain. *Mon. Wea. Rev.*,**139**, 3163-3183.

Li X., W. K. Tao, A. P. Khain, J. Simpson, and D. E. Johnson, 2009: Sensitivity of a cloud-resolving model to bulk and explicit bin microphysical schemes. Part II: Cloud microphysics and storm dynamics interactions. *J. Atmos. Sci.*, **66**, 22-40.

Lin, Y. L., R. D. Farley, and H. D. Orville, 1983: Bulk parameterization of the snow field in a cloud model. *J. Climate Appl. Meteor.,* **22**, 1065-1092.

Loftus, A. M., D. B. Weber, and C. A. Doswell III, 2008: Parameterized mesoscale forcing mechanisms for initiating numerically simulated isolated multicellular convection. *Mon. Wea. Rev.*,**136**, 2408-2421.

Lorenz, E. N., 1960: Energy and numerical weather prediction. *Tellus*, **12**, 364-373.

Maddox, R. A., 1976: An evaluation of tornado proximity wind and stability data. *Mon. Wea. Rev.*, **104**, 133-142.

____, L. R. Hoxit, and C. F. Chappell, 1980: A study of tornadic thunderstorm interactions with thermal boundaries. *Mon. Wea. Rev.*, **108**, 322-336.

Markowski, P. M., E. N. Rasmussen, and J. M. Straka, 1998: The occurance of tornadoes in supercells interacting with boundaries during VORTEX-95. *Wea. Forecasting*, **13**, 852-859.

____, J. M. Straka, E. N. Rasmussen, and D. O. Blanchard, 1998: Variability of storm-relative helicity during VORTEX. Mon. Wea. Rev., **126**, 2959-2971.

____, ____, and ____, 2002: Direct thermodynamic observations within the rear-flank downdrafts of nontornadic and tornadic supercells. *Mon. Wea. Rev.*, **130**, 1692-1721.

____, ____, and ____, 2003: Tornadogenesis resulting from the transport of circulation by a downdraft: Idealized numerical simulations. *J. Atmos. Sci.*, **60**, 795-823.

____, E. Rasmussen, J. Straka, R. Davies-Jones, Y. Richardson, and R. J. Trapp, 2008: Vortex lines within low-level mesocyclones obtained from pseudo-dual-Doppler radar observations. *Mon. Wea. Rev.*, **136**, 3513-3535.

____, M. Majcen, Y. Richardson, J. Marquis, and J. Wurman, 2011: Characteristics of the wind field in three nontornadic low-level mesocyclones observed by the Doppler on Wheels radars. *Electronic J. of Severe Storms Meteor.*, **6**, 1-48.

Marshall, J. S., and W. M. Palmer, 1948: The distribution of raindrops with size. *J. Meteor.*, **5**, 165-166.

Marwitz, J. D., 1972: The structure and motion of severe hail-storms, Part I: Supercell storms. *J. Appl. Meteor*., **11**, 166–179.

McCaul, E. W. Jr., 1991: Buoyancy and shear characteristics of hurricane-tornado environments. *Mon. Wea. Rev.*, **119**, 1954–1978.

——, and M. L. Weisman, 1996: Simulations of shallow supercell storms in landfalling hurricane environments. *Mon. Wea. Rev*., **124**, 408–429.

____, and Cohen, 2004: The initiation, longevity, and morphology of simulated convective storms as a function of free tropospheric relative humidity. *22nd Conf. on Severe Local Storms*, Hyannis MA, Amer. Meteor. Soc.

McNider, R. T. and F. J. Kopp, 1990: Specification of the scale and magnitude of thermals used to initiate convection in cloud models. *J. Appl. Meteor.*, **29**, 99-104.

McPherson, R. A., and K. K. Droegemeier, 1991: Numerical predictability experiments of the May 20 1977 Del City, OK supercell storm. Preprints, *Ninth Conf. on Numerical Weather Prediction*, Denver, CO, Amer. Meteor. Soc., 734-738.

Milbrandt, J. A., M. K. Yau, J. Mailhot, S. Belair, and R. McTaggart-Cowan, 2010: Simulation of an orographic precipitation event during IMPROVE-2. Part II: Sensitivity to the number of moments in the bulk microphysics scheme, *Mon. Wea. Rev.*, *138*, 1152-1171.

Morrison, H., and J. Milbrandt, 2011: Comparison of two-moment bulk microphysics schemes in idealized supercell thunderstorm simulations, *Mon. Wea. Rev., 139*, 1103-1130.

Moller, A. R., C. A. Doswell III, M. P. Foster, and G. R. Woodall, 1994: The operational recognition of supercell thunderstorm environments and storm structures. *Wea. Forecasting*, **9**, 327–324.

Munoz, L. A., 1994: Structure and evolution of thunderstorms encountering temperature inversions. M. S. Thesis, University of Illinois at Urbana-Champaign, 62 pp.

Naylor, J., M. A. Askelson, and M. S. Gilmore, 2012: Influence of low-level thermodynamic structure on the downdraft properties of simulated supercells, *Mon. Wea. Rev.*,**140**, 2575-2589.

Newton, C. W., and S. Katz, 1958: Movement of large convective rain-storms in relation to winds aloft. *Bull. Amer. Meteor. Soc.*, **39**, 129–136.

Potvin, C. K., K. L. Elmore, and S. J. Weiss, 2008: Assessing the impact of proximity sounding criteria on the climatological significant tornado environment. *24th Conference on Severe Local Storms*, Savannah, GA. Amer. Meteor. Soc.

Purser, R. J., and L. M. Leslie, 1988: A semi-implicit, semi-Lagrangian finite-difference scheme using high-order spatial differencing on a nonstaggered grid. *Mon. Wea. Rev.*, **116**, 2069-2080.

Rasmussen, E. N., J. M. Straka, R. Davies-Jones, C. A. Doswell III, F. H. Carr, M. D. Elits and D. R. MacGorman, 1994: Verification of the origins of rotation in tornadoes experiment: VORTEX. *Bull. Amer. Met. Soc.*, **75**, 995-1006.

____, and ____ 1998: Variations in supercell morphology. Part I: Observations of the Role of upper-level storm-relative flow. *Mon. Wea. Rev.*, **126**, 2406-2421.

Richardson, Y. P., K. K. Dreoegemeier, and R. P. Davies-Jones, 2007: The influence of horizontal environmental variability on numerically simulated convective storms. Part I: Variations in vertical shear. *Mon. Wea. Rev.*, **135**, 3429-3455.

Rotunno, R., 1981: On the evolution of thunderstorm rotation. *Mon. Wea. Rev.*, **109**, 577-586.

____, and ____, 1985: On the rotation and propagation of simulated supercell thunderstorms. *J. Atmos. Sci*., **42**, 271-292.

Shabbott, C. J., and P. M. Markowski, 2006: Surface in situ observations within the outflow of forward-flank downdrafts in supercell thunderstorms. *Mon. Wea. Rev.*, **134**, 1422-1441.

Smagorinsky, J., 1963: General circulation experiments with the primitive equations. *Mon. Wea. Rev.*, **91**, 99-164.

Smith, P. L., C. G. Myers, and H. D. Orville, 1975: Radar reflectivity factor calculations in numerical cloud models using bulk parameterizations of precipitation, *J. Appl. Meteor.*, **14**, 1156-1165.

Snook, N. A., and M. Xue, 2006: Sensitivity of tornadogenesis in very-high resolution numerical simulations to variations in model microphysical parameters. *23rd Conference on Severe Local Storms*, St. Louis, MO. Amer. Meteor. Soc.

Sobash, R. A., J. S. Kain, D. R. Bright, A. R. Dean, M. C. Coniglio, and S. J. Weiss, 2011: Probabilistic forecast guidance for severe thunderstorms based on the identification of extreme phenomena in convective-allowing model forecasts. *Wea. Forecasting,* **26**, 714-728.

Stensrud, D. J., 2007: *Parameterization Schemes: Keys to Understanding Numerical Weather Prediction Models*. Cambridge, 459 pp.

____, G. S. Manikin, E. Rogers, and K. E. Mitchell, 1999: Importance of cold pools to NCEP mesoscale Eta Model forecasts. *Wea. Forecasting*, **14**, 650-670.

____, M. Xue, L. J. Wicker, K. E. Kelleher, M. P. Foster, T. Schaefer, R. S. Schneider, S. G. Benjamin, S. S. Weygandt, J. T. Ferree, and J. P. Tuell, 2009: Convective-scale warn-on-forecast system: A vision for 2020, *Bull. Amer. Met. Soc.*, **90**, 1487-1499.

Stout, G.E., and F.A. Huff, 1953: Radar records Illinois tornadogenesis. *Bull. Amer. Meteor. Soc.*, **34**, 281–284.

Straka, J. M., and E. N. Rasmussen, 1998: Thirty years of cloud modeling: Does the emperor wear clothes? *Preprints*, *19th Conf. on Severe Local Storms*, Minneapolis, MN, Amer. Meteor. Soc., 342-347.

Thompson, R. L., R. Edwards, J. A. Hart, K. L. Elmore, and P. M. Markowski, 2003: Close proximity soundings within supercell environments obtained from the rapid update cycle. *Wea. Forecasting*, **18**, 1243-1261.

____, C. M. Mead, and R. Edwards, 2007: Effective storm-relative helicity and bulk shear in supercell thunderstorm environments. *Wea. Forecasting*, **22**, 102-115.

____, B. T. Smith, J. S. Grams, A. R. Dean, and C. Broyles (2012), Convective modes for significant severe thunderstorms in the contiguous United States. Part II: Supercell and QLCS tornado environments, *Wea. Forecasting*, In press.

Togstad, William E., J. M. Davies, S. J. Corfidi, D. R. Bright, and A. R. Dean, 2011: Conditional probability estimation for significant tornadoes based on Rapid Update Cycle (RUC) profiles, *Wea. Forecasting, 26*, 729-743.

Trapp, R. J., 1999: Observations of nontornadic low-level mesocyclones and attendant tornadogenesis failure during VORTEX. *Mon. Wea. Rev.*, **127**, 1693-1705.

____., and B. H. Fiedler, 1995: Tornado-like vortexgenesis in a simplified numerical model. *J. Atmos. Sci.*, **52**, 3757-3778.

____, and R. Davies-Jones, 1997: Tornadogenesis with and without a dynamic pipe effect. *J. Atmos. Sci.*, **54**, 113-133.

____, E. D. Mitchell, G. A. Tipton, D. W. Effertz, A. I. Watson, D. L. Anrda Jr., and M. A. Magsig, 1999: Descending and nondescending tornadic vortex signatures detected by WSR-88Ds. *Wea. Forecasting*, **14**, 625-639.

Tripoli, G. J., and W. R. Cotton, 1980: A numerical investigation of several factors contributing to the observed variable intensity of deep convection over south Florida. *J. Appl. Meteor.*, **19**, 1037-1063.

Wakimoto, R. M., and H. Cai, 2000: Analysis of a nontornadic storm during VORTEX 95. *Mon. Wea. Rev.*, **128**, 565-592.

Wakimoto, R. M., H. V. Murphy, and H. Cai, 2004: The San Angelo, Texas, Supercell of 31 May 1995: Visual observations and tornadogenesis. *Mon. Wea. Rev., 132*, 1269-1293.

Walko, R. L., 1993: Tornado spin-up beneath a convective cell: Required basic structure of the near-field boundary layer winds. *The Tornado: Its Structure, Dynamics, Prediction, and Hazards, Geophys. Monogr.*, No 79, Amer. Geophys. Union, 89-95.

Weisman, M. L., and J. B. Klemp, 1982: The dependence of numerically simulated convective storms on vertical wind shear and buoyancy. *Mon. Wea. Rev.*, **110**, 504-520.

____, and ____, 1984: The structure and classification of numerically simulated convective storms in directionally varying wind shears. *Mon. Wea. Rev.*, **112**, 2479-2498.

___, C. Davis, W. Wang, K. W. Manning, and J. B. Klemp, 2008: Experiences with 0 – 36-h explicit convective forecasts with the WRF-ARW model, *Wea. Forecasting*, **23**, 407-437.

____, W. C. Skamarock, and J. B. Klemp, 1997: The resolution dependence of explicitly modeled convective systems. *Mon. Wea. Rev.*, **125**, 527-548.

Wicker, L. J., 1990: A numerical simulation of a tornado-scale vortex in a three-dimensional cloud model. Ph.D. thesis, University of Illinois, 264 pp.

____, and R. B. Wilhelmson, 1993: Simulation of tornadogenesis within a supercell thunderstorm. *The Tornado: Its Structure, Dynamics, Prediction, and Hazards, Geophys. Monogr.*, No 79, Amer. Geophys. Union, 161-172.

____, and R. B. Wilhelmson, 1995: Simulation and analysis of tornado development and decay within a three-dimensional supercell thunderstorm. *J. Atmos. Sci.*, **52**, 2675-2703.

Wicker, L. J., M. P. Kay, and M. P. Foster, 1997: STORMTIPE-95: Results from a convective storm forecast experiment. *Wea. Forecasting*, **12**, 388–398.

Wilks, D. S., 2006: *Statistical Methods in the Atmospheric Sciences*. Academic Press, 627.

Wurman, J., Y. Richardson, C. Alexander, S. Weygandt, and P. F. Zhang, 2007: Dual-Doppler and single-Doppler analysis of a tornadic storm undergoing mergers and repeated tornadogenesis, *Mon. Wea. Rev., 135*, 736-758.

____, K. Kosiba, P. Markowski, Y. Richardson, D. Dowell, and P. Robinson, 2010: Finscale single- and dual-Doppler analysis of tornado intensification, maintenance, and dissipation in the Orleans, Nebraska, supercell, *Mon. Wea. Rev., 138*, 4439-4455.

Wyngaard, J. C., 2004: Toward numerical modeling in the "terra incognita". *J. Atmos. Sci.*, **61**, 1816-1826.

Ziegler, C. L., T. J. Lee, and R. A. Pielke Sr., 1997: Convective initation at the dryline: A modeling study. *Mon. Wea. Rev.*, **125**, 1001-1026.

____, E. N. Rasmussen, T. R. Shepherd, A. I. Watson, and J. M. Straka, 2001: The evolution of low-level rotation in the 29 May 1994 Newcastle-Graham storm complex during VORTEX. Mon. Wea. Rev., 129, 1339-1368.

____, E. R. Mansell, J. M. Straka, D. R. MacGorman, and D. W. Burgess, 2010: The impact of spatial variations of low-level stability on the life cycle of a simulated supercell storm. *Mon. Wea. Rev.*, **138**, 1738-1766.